Integrated circuits employing non-linear dynamics of coupled single-electron devices

結合単電子デバイスの非線形ダイナミクスを利用した集積回路に関する研究

Andrew Kilinga Kikombo

Submitted in partial fulfillment of the requirements
of the Ph.D. Degree in Engineering

February 2010

Graduate School of Information Science and Technology
Hokkaido University

Acknowledgements

This thesis marks the end of my 5 year studentship at Hokkaido university, from the Masters course through the PhD course. The 5 years have been successful because of the efforts and support of many people.

First and foremost are my wonderful advisors, Professor Yoshihito Amemiya (Director of the Laboratory of Advanced LSI Engineering (LALSIE)) and Associate Prof. Tetsuya Asai; notably, for creating an open research environment in which I have performed my graduate studies. I came to Hokkaido university intending to join this group, for two primary reasons: the area of research in which they were working, and what I had perceived of the laboratory during a summer visit. I have not been disappointed in either regard. My advisors have provided academic as well as personal guidance during my graduate studies and at key moments in my studies in Japan, while also providing me with a lot of room to work independently the majority of the time.

My sincere thanks are due to the official referees, Prof. Yasuo Takahashi and Prof. Takashi Fukui, for their detailed review, constructive criticism and excellent advice during the preparation of this thesis.

My interest in the present area of research dates back to my undergraduate studies carried out at the University of Telecommunications (Tokyo). My advisors, Prof. H. Morisaki (presently professor emeritus at the same university), Prof. S. Nozaki and Associate Prof. K. Uchida, introduced me to the field of nano-devices, which turned out to be my primary field of research through out my graduate studies. I would take this chance to thank all of them.

I am greatly indebted to my former advisors at Niihama National College of Technology, Prof. Y. Minamoto and Prof. K. Inami for their invaluable guidance during my first four years in Japan. Both motivated me to proceed with higher studies in Japan.

My thanks also go to Prof. Y. Leblebici and Dr. A. Schmid of the Microelectronic Systems Laboratory (LSM) at the Swiss Federal Institute (EPFL) for fruitful discussions and advice concerning my research in bio-inspired LSIs, during my stay at EPFL as a visiting PhD student in Sept. 2007, and Aug. - Sept. 2008.

During my graduate studies, I worked with many students and former faculty staff who have influenced me in various ways. My thanks go to Dr. T. Oya who helped me jump start my research in nano electronic circuits. Secondly, I would like to recognize Dr. T. Hirose for his motivation. I would also like to thank Dr. Ken'ichi Ueno who was both my peer and room mate all through the graduate studies. My thanks goes to all the students at the LALSIE laboratory for providing a stimulating and fun environment in which to learn and grow..

This research was partially supported by the "JSPS Research Fellowships for Young Scientists". I would also like to extend my word of gratitude to the GCOE program at the Graduate School of Information sciences and Technology for financial support. I would also like to thank the "Ito Foundation for International Education Exchange" for much needed financial support in the first 2 years of my graduate studies.

Special thanks to my parents, Boniface and Felistus, who cultivated my interest in natural sciences early in my life, and for unconditional support and encouragement to pursue my interests. I would like to thank them for all the invaluable support all through my studies. The same goes to the rest of my family. I would also like to extend my sincere thanks to Shinohara family, for the extended support all through my graduate studies.

Abstract

本論文の目的は、次世代集積機能デバイス（量子デバイス）の物理的振る舞いおよび構造的特徴を積極的に利用して信号処理を行う新しい集積回路アーキテクチャの検討と実応用につなげることである。

これまで、集積回路の高機能化・高性能化は基本素子であるトランジスタの微細化により進められてきた。しかし、素子の寸法が小さくなるにつれて量子効果や素子ばらつき（通常の回路動作にとっては望ましくない影響）が顕著になり、近い将来に微細化の限界が避けられないとも言われている。これらの問題点を解決するにはプロセス技術の向上により素子ばらつきの抑制、新しい材料の開発をもって量子効果を抑制する方法または設計の段階でエラー補正回路を組み込む方法が研究されている。その一方、近年の微細加工技術の進歩により、これまで困難であった量子集積ナノ構造の作成が可能となり、量子効果を積極的に利用するデバイスの研究も盛んに行われる様になった。CMOS デバイスによる集積回路と並ぶ次世代量子デバイスの候補として単電子デバイスが注目を浴びている。しかし単電子デバイスの動作は現用の CMOS デバイスと異なるため、従来の手法と異なる新しい回路構築方法（回路アーキテクチャ）と信号処理の方法を考える必要がある。また、国際半導体ロードマップ（ITRS）の最近の調査によれば、これからの LSI の高機能化・高性能化においてデバイス技術だけでなくアーキテクチャの技術革新の必要性が高まってきている。つまり、これまでのノイマン型アーキテクチャの延長上ではなくて、デバイスそのものの特性を理解し、またデバイス構造も生かした信号処理方法を考える必要がある。本論文では微細化によって生ずる量子効果を排除するのではなく、積極的に利用した回路アーキテクチャを検討する。ここでは単電子デバイスに着目し、新しい回路構成及びアプリケーションを提案し、コンピュータシミュレーションにて動作確認を行う。

単電子回路はクーロンブロッケードを利用して電子の輸送を一つ一つ制御し、極低消費電力で動作する LSI の基本素子として期待されている。さらに単電子デバイスの素子寸法は数ナノメートルオーダーとなっており、必然的に極低小面積な回路を構成することができる。多数の単電子素子を集積すれば空間的に高分解能な量子ドット集積体デバイスを実現することができ、センサへの新しいアプリケーションに応用できる。単電子デバイスは電子トンネリングにより、離散的な挙動を示す。また量子ドット上に抵抗体を堆積した単電子振動子素子は緩和振動を示し豊富な非線形ダイナミクスを有する離散力学システムといえる。基板上に集積された単電子デバイスの一つ一つを信号処理機能を持たせば新しい集積回路を組むことが可能である。本論文は上記の単電子回路の特徴 — 構造的特徴および豊富な非線形ダイナミクス — を組み合わせた従来の LSI 回路の枠を超える新しい集積回路開拓を行う。本研究で得られた成果の概要は以下に示す。

- 結合型単電子デバイスの非線形特性の解析

  本論文では、単電子回路の非線形ダイナミクスを把握するために、容量結合の振動子対および２次元ネットワークを取り上げて、その非線形特性を解析した。解析結果より、単電子でバイスは多周期振動、初期状態に依存する複数アトラクタの発生、振動子のノード電位パターンから成る散逸構造の発生、振動子ノード間の相互作用とトンネル事象の伝搬（トンネル波の発生）等の非線形的な性質が存在することが明らかになった。これらの非線形性を利用することで新機能を持つ集積システムの実現する可能を示唆した。上記の解析結果に基づき、以下具体的な２つの単電子システムを提案した。

- 量子ドット集合体のを利用したフォトン位置検出システム

  量子ドット集積体の構造的特徴および結合型単電子デバイスのドット間におけるトンネル波の伝搬を利用した高空間分解能な二次元フォトン位置検出センサを提案した。従来の入射フォトンの二次元位置を検出するデバイスとしてマイクロチャンネルプレート（光電子増倍管の二次元集積体：以下 MCP）が使われている。MCP の検出精度はその空間分解能で決まるが製作プロセスの制限により１０μ m 以下にする事は困難である。そこで本研究では、単電子ネットワークを利用する事により高空間分解能なセンサを実現する事を提案した。このセンサは正負交互にバイアスされた単電子振動子ネットワークからなる。空間分解能を 0.1 μ m 以下にする事が可能である。フォトンが入射してネットワーク内の振動子の一つに当たると、そのクーロンブロッケードが破れて電子トンネルが発生する（フォトン誘発トンネリング)。そのため振動子のノード電位が変化し、それが隣接する振動子のトンネル事象を誘発する。このトンネル波はネットワーク全体に拡がってセンサの周縁に到達する。トンネル波が周縁に到着する時刻を観測することで波の発生場所（フォトンの入射位置）を知る事ができる。以上の着想をもとに具体的なデバイス設計方針を開発し、プロトタイプデバイスを例として計算機シミュレーションによりフォトン位置検出の動作を確認した。

- 生物の信号処理機能に学んだ単電子振動子ネットワークシステム

  単電子素子の非線形性を利用して生物の持つ高い機能を模倣するための信号処理アーキテクチャを提案した。ここでは、比較的にしくみが明らかとなっている網膜の輪郭検出と動き検出の動作を単電子振動子ネットワークでコンパクトにハードウェア化する方法を提案した。これを具体的な回路にするときには「デバイス特性ばらつき」と「環境（熱）雑音」が問題となるが、これを排除するのではなくて、逆に利用して処理能力の向上につなげる方法を考えた。パルス密度変調にもとづいてノイズを活用しながら輪郭検出と動き検出を行う単電子ネットワークの網

膜回路を設計し、ノイズ利用により SN 比や動作精度が向上することを計算機による動作シミュレーションで確認した。

Abstract

This thesis aims at establishing novel signal processing architectures for single-electron devices.

The present trend in improving the performance of silicon LSIs has been primarily as a result of the continuous scaling of CMOS devices. The need to scale transistors has led to improvement of fabrication technologies. With the advamced LSI fabrication technologies, research on fabrication of minute nano scale structures (devices) has attracted a lot of attention. Such devices include nano wires, quantum nano dots and single-electron devices.

Single-electron devices utilize quantum-mechanical effects to control transport of electrons at the single level. Thus single-electron devices inherently operate with minimum low power dissipation. Additionally, owing to the minute physical sizes of single-electron devices, they are considered as potential devices in implementing parallel-based information paradigms that would require high device densities.

Single-electron devices operate on different principles as compared to the conventional MOSFET devices. Therefore to employ them in signal processing systems, there in need to establish new circuit architecture frame works that fully utilize their properties. This research aims at exploiting both dynamical and structural properties of single-electron devices toward establishing LSI platforms for nano devices.

This research starts with investigating non-linear characteristics of coupled single-electron devices. Single-electron devices portray interesting non-linear dynamics: a single-electron device shows relaxation oscillations, while a double-oscillator system (two single-electron oscillators coupled through a capacitor) have attractors of oscillation that are independent of initial node voltage conditions. A quadruple oscillator system (two capacitively coupled double-oscillator systems) show multi periodic oscillations. Furthermore, by coupling single-electron devices, one can control the flow of tunneling events within the device network.

By combining the above non-linear dynamics with the structural properties, we proposed a two-dimensional photon position detecting circuit, and evaluated its performance. Secondly, by obtaining hints from neuronal systems, we proposed two bio-inspired LSI circuits: an edge detection circuit and a motion detector circuit. The thesis also discusses the implications of device fabrication mismatches and environmental noises in fabricating the two bio-inspired circuits. Instead of getting rid of such noises, we propose a novel method where such noises are actively utilized to improve the performance of LSI circuits.

Contents

1 Introduction

1.1 Background

This research aims at establishing a novel architectural platform for designing electronic circuits based on the operation principles, and employing both structural properties and non-linear dynamics of quantum nano electronic devices.

For the past 4 decades, the continuous scaling of semiconductor devices has been the primary driving force behind improving the performance of digital information processing systems. The decreasing feature sizes of transistors have been accompanied by dramatic increase in speed and integration densities, which have in turn led to increased and diversified functionality in LSI circuits. This trend has been viable mainly due to guaranteed reliability in the downscaled devices. Reliability corresponds to high yields per die, hence low production costs (high cost efficiency), giving the circuit designer the opportunity to create reliable integrated systems with improved processing speeds, and increased functionality. However, as the physical feature sizes approach the deep sub-micron regime, process variations and undesirable internal (and or external) noises associated with nano-scale properties pose critical concerns on the future of scaling [1]; they dramatically reduce the reliability of electronic devices on the edge of nano-scales. Additionally, as CMOS transistors are scaled down, the average power dissipation per transistor increases exponentially due to leakage currents. As we scale down further, the density of transistors per unit area is expected to increase even further, thus driving the increase in power dissipation per unit area at a faster rate. Consequently, the number of transistors that can be integrated would be limited by the maximum allowable power density of approximately 100 $\mathrm{W/cm^2}$, and not by the size of transistors. This means that future integration capacities of scaled CMOS devices is fundamentally determined by two critical factors: size of transistors and power density, both of which are rapidly approaching their practical limits in the near future [2], [3].

Getting rid of such nano-scale properties would involve improving device fabrication technologies, or introducing error-detecting circuits within the system. The

latter would lead to advanced complexity, and design tradeoffs in using high integration capacities available to the circuit designer. Consequently, a new approache into utilizing and not eradicating nano-scale properties in future electronic devices is seen as a promising breakthrough in future LSI circuits. This has led to extensive research into the so called *emerging research devices* (ERDs) [5]. Such devices include nano-electronic devices such as single-electron devices, quantum dot devices, nano-wires, carbon nanotubes etc. Nano scale devices operate under entirely different operation principles from the present conventional CMOS devices.

In employing such devices in future information and signal processing systems, we need to come up with new ways of designing electronic circuits: novel methodologies to fully utilize the computation potentials and the terascale level of integration that such devices offer. This calls for the need of innovative circuit architecture platforms for nano-devices. In a recent report by the International Technology Roadmap for Semiconductors (ITRS) [6], it is predicted that improving the performance of future LSI circuits will not only depend on the improvement of fabrication technologies, but also on innovative circuit architectures that can accommodate future electronic devices. In other words, circuit architectures, that can accommodate new device concepts, are expected to play an important role in improving the performance of future LSI circuits. Examples of such architectures include heterogeneous architectures, molecular architectures, morphic (bio-inspired) architectures, hybrid computing architectures [7].

In this research, we investigate non-linear characteristics of coupled single-electron devices and use such characteristics to propose innovative circuit architectures and applications suitable for implementation with single-electron devices. The proposed architectures subtly utilize the nano-scale properties of single-electron devices; they employ both dynamical characteristics and structural properties of single-electron devices to establish new circuit architectures and signal processing technologies.

1.2 Objective

Single-electron devices are viewed as potential devices for use in LSI circuits because (i) they operate by controlling the flow of electrons at the single level, thus they can operate with extreme low power dissipation and (ii) due to their small feature sizes, they have potential for high levels of integration. In other words, owing to the minute sizes of single-electron devices, they could be integrated to create a functional device with a high spatial resolution for sensor applications. Such a sensor would require the constitutive elements to have ultimate low power dissipation,

to circumvent the thermal constraint explained in the preceding section 1.1. Further more, single-electron devices exhibit a high degree of non linearity because of the coexistence of continuous time and discrete time dynamics. By combining these two properties of single-electron devices, we could create a highly functional LSI devices that can compliment the function of the present conventional CMOS LSIs. By employing the two properties mentioned above, we propose a 2 dimensional photon position sensor network with a high spatial resolution, and confirm its operation through computer simulations. To realize such a sensor, one would be required to detect signals from one device and feed them to the next (or neighboring) devices. From a practical point of view, with such a high density of devices it would be impossible to fabricate wires between the device elements. Even if this could be achievable, the high parasitic capacitance would make it impossible to retrieve signals. To solve this problem, the proposed photon sensor employs capacitive coupling introduced between individual devices, that enables signal transmission through the device network. This is realized by laying positively and negatively biased devices in a checkered pattern to facilitate propagation of signals within the sensor device. We further expand our focus into realizing reliable systems with failure prone devices. As we mentioned in the preceding section, as the size of devices decreases, the device parametric variations also increase. This is true to both CMOS devices as well as nano devices. Therefore, to fabricate our photon position sensor, we have to come up with ways to to come up with ways of mitigating the effects of process variations. Additionally, since logic states in nano-devices, in particular, single-electron devices is represented by an extremely low number of electrons, this renders them vulnerable to environmental (thermal) noises. Therefore as we look into new circuit architectures, we have to be aware of the process variations and noise induced errors in future LSIs. A promising solution to noise-related problems could be solved by considering how living organisms carry out signal processing. Such LSIs are referred to as *neuromorphic* LSIs. This is discussed in detail in the third part of this research, where we propose circuit architectures that are inspired by image processing mechanisms in the retina. In addition, we evaluate the implications of noises in implementing the proposed circuits, where instead of eliminating such noises, a novel method on how to exploit them to improve the performance of LSIs is proposed. The proposed methodologies show that we can actually utilize these noises to improve the performance of LSI circuits.

The thesis is outlined as follows.

- Chapter 1 explains the background and purpose of this research.
- Chapters 2 and 3 give introduces the operation of single electron devices, where the Coulomb-blockade phenomenon and methodology of simulating

single-electron oscillator circuits is discussed.

Part (I) of the thesis consists of chapters 4 and 5.

- In chapter 4, the thesis focuses on the basics of dynamical systems, where a brief description of the terminology used in describing dynamical systems is introduced.

- Chapter 5 introduces non linear dynamics of single-electron devices as dynamical systems; the operation principle of single-electron oscillators is explained and non linear dynamics of capacitively coupled systems are investigated. The chapter starts by giving details of the circuit configuration and equations governing their operation. Their dynamics are confirmed through computer simulations, and the results are illustrated with the use of attractors of oscillation, phase diagrams, bifurcation maps, and diagrams showing basins of attraction.

  The chapters that follow focus on practical applications of single-electron devices in information and signal processing LSIs. They are divided into two parts: the first part (Part (II): chapter 6) explains about a two-dimensional photon position sensor that utilizes both the non-linear characteristics and structural properties of single-electron devices. The second part (Part (iii)) consists of chapters 7, 8 and 9, where circuit architectures that employ non-linear properties of single-electron devices to mimic signal processing in biological signal processing systems, and the implications of noises in LSIs are discussed. The details are as follows.

- Chapter 6 discusses a two-dimensional sensor that utilizes both structural properties of single-electron devices to achieve a high spatial resolution, and also makes use of non linear dynamics in signal propagation between neighboring devices.

- Chapters 7 and 8 focus on circuit architectures inspired by information processing in biological systems. Chapter 7 describes a motion detection sensor inspired by motion detection schemes in insects, while chapter 8 describes an edge detection sensor that is inspired by edge detection in the vertebrate retina.

- Chapter 9 focuses on creating reliable electronic systems with unreliable computing devices: that is we introduce a new concept of information processing where noises are exploited in improving the performance of electronic systems.

- Finally, chapter 10 concludes with a summary of this research.

References

[1] Skotnicki, T., Hutchby, J.A., King, T.-J., Wong, H.-S.P., and Boeuf, F., "The end of CMOS scaling," IEEE Circuits Devices Mag.,, vol. 21, pp. 16-26, 2005.

[2] Zhirnov, V.V. Cavin, R.K., III Hutchby, J.A. Bourianoff, G.I., "Limits to binary logic switch scaling - a gedanken model," Proc. IEEE, vol. 91, pp. 1934- 1939, 2003.

[3] Keyes R.W., "Fundamental limits in physical information processing," Proc. IEEE, vol. 69, no. 2, pp. 267-268, 1981.

[4] Zhirnov, V.V., Hutchby, J.A., Bourianoff, G.I., Brewer, J.E., "Emerging research memory and logic technologies," Circuits and Devices Magazine, IEEE, vol. 21, pp. 47- 51, 2005.

[5] Zhirnov, V.V., Hutchby, J.A., Bourianoff, G.I., and Brewer, J.E., "Emerging research logic devices," IEEE Circuits Devices Mag., vol. 21, pp. 37-46, 2005.

[6] International technology roadmap for semiconductors - 2003 edition, 2003. see http://public.itrs.net.

[7] Cavin, R., Hutchby, J.A., Zhirnov, V., Brewer, J.E., Bourianoff, G., "Emerging Research Architectures," COMPUTER, vol. 41, pp. 33-37, 2008.

2

Single Electron Devices

2.1 Introduction

The single electron device, which unlike ordinary electronic devices, operates by controlling the transport of single or small number of electrons through the Coulomb blockade phenomenon is seen as a promising device for future LSI circuits. A single electron device transports electrons across the tunneling junction depending on bias voltage: if the voltage of any of the circuit nodes exceeds (or falls below) the threshold voltage, an electron tunnels from the ground to the node (or from the node to the ground), leading to a discrete change in the entire circuit node voltages [17]. Tunneling junctions, are fabricated by sandwiching an extremely thin layer of an electrically insulating substance between two conducting plates (electrodes) to make a metal-insulator-metal tunneling junction(Fig. 2.1) [2], or confining a 2-dimensional electron gas of a GaAs/AlGaAs heterostructure to minute islands by Schottky gates [3] and [4].

For an electron to travel from one conducting plate to the other, it has to "ride over" the potential barrier created by the intermediate insulator material, between the two conducting electrodes. From the stand point of classical mechanics, electrical transport through a barrier is not possible. However, in quantum physics, particles assume wave-particle duality behavior, thus as a waves, electrons can

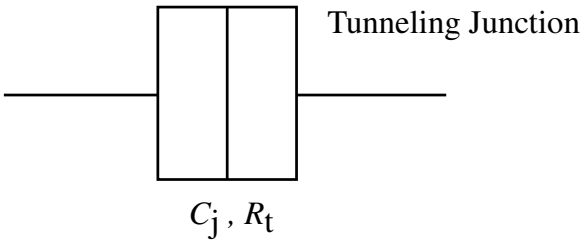

Figure 2.1: Single-electron tunneling junction consisting of a tunneling capacitance C_j, and a tunneling resistance R_t.

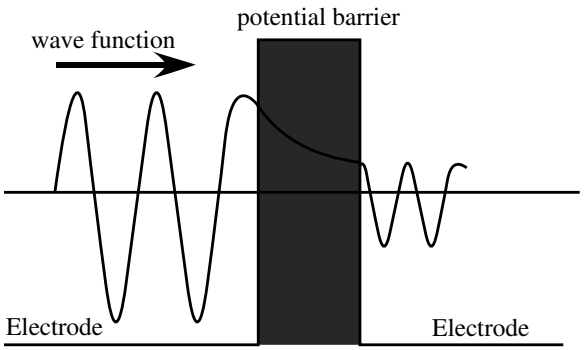

Figure 2.2: Electron tunneling across a junction.

leak through the potential wall to the other side across the insulator (Fig. 2.2). A detailed explanation on the fundamentals of single-electron devices is illustrated in reference [17].

This chapter begins with an elaboration of the Coulomb blockade phenomenon in sec. 2.2, followed by a description of single electron simulation methodology (sec. 2.3).

2.2 Coulomb Blockade Phenomenon

Electron tunneling across a tunneling junction, in a given circuit, takes place only if the net electrostatic energy of the entire circuit would decrease as a result of the tunneling event. To understand this phenomenon, consider Fig. 2.3, where a tunneling junction is connected to an external current source. Considering the electrostatic energy of the circuit, before and after a single electron tunnells as shown in Fig. 2.3, we obtain the resulting change in energy as

$$\Delta E = \frac{|Q|^2}{2C_{\mathrm{j}}} - \frac{|Q-e|^2}{2C_{\mathrm{j}}}\,, \tag{2.1}$$

where C_{j} is the capacitance of the tunneling junction, and e is elementary charge of an electron. Since tunneling can take place only if the change in electrostatic energy ΔE of the system is positive, it follows that tunneling is favorable if the charge Q on the junction falls in the range of

$$-\frac{e}{2} < Q \mathrm{and} Q > \frac{e}{2} \tag{2.2}$$

as shown in Fig. 2.4.

As shown in the diagram, a tunneling event can occur only if the charge accumulated on the junction exceeds $e/2$ for a downward tunneling, and decreases

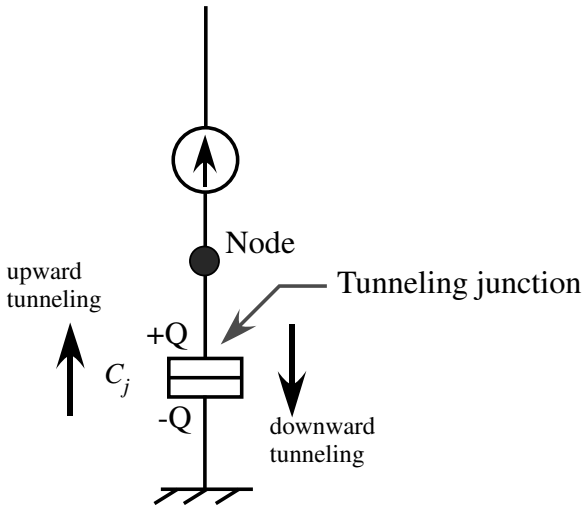

Figure 2.3: Single-electron tunneling junction connected to a constant current source.

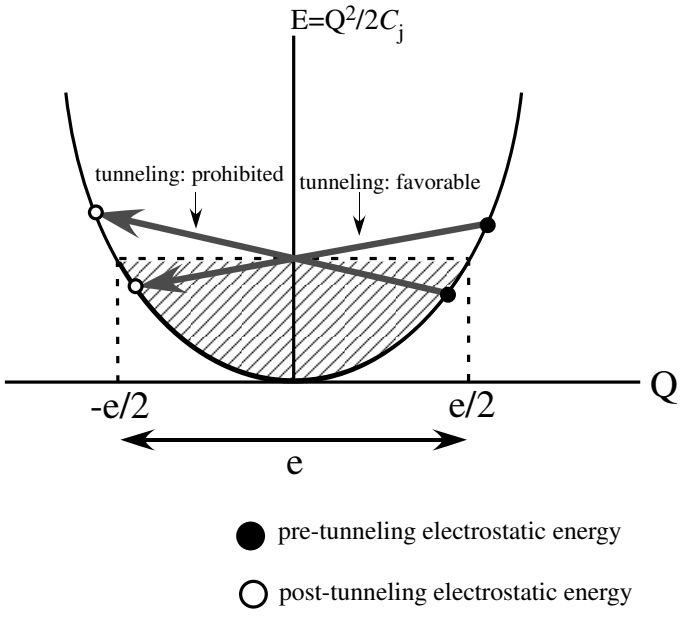

Figure 2.4: Energy diagram illustrating the Coulomb blockade phenomenon. Transitions are favorable when the charge on the junction is in the range $|Q| > e/2$.

beyond $-e/2$ for an upward tunnneling (if the bias current is connected in the opposite direction).

For single electron phenomenon to be observed in nano-scale tunneling junctions, a number of criteria are mandatory. These include the tunneling resistance, and the electrostatic energy, determined by the size of the tunneling capacitance.

(i)Tunneling resistance [5]

In classical theory, an electron is assumed to be well localized. However, in quantum mechanics theory electrons are described by wave functions, indicating the probability of the presence of an electron. If a tunnel barrier is insufficiently opaque, the electron wave function extends through the barrier and the electron is not clearly localized on the island. The opaqueness of a tunneling barrier is described by the tunnelling resistance R_{t}. A sufficient condition for observing coulomb blockade phenomenon is:

$$R_{\mathrm{t}} \gg R_k = h/e^2 \approx 25.8\ \mathrm{k\Omega} \tag{2.3}$$

where h is Plank's constant.

(ii)Electrostatic energy

Secondly, the size of the tunneling junctions (in other words, the capacitance of the tunneling junction $C\mathrm{j}$) has to be small enough so that the electrostatic energy E_c required to transport a single electron across the junction exceeds the thermal energy.

$$E_c = \frac{e^2}{2C_{\mathrm{j}}} \gg k_{\mathrm{B}}T, \tag{2.4}$$

where k_{B} is Boltzmann's constant and T is the absolute temperature. If this condition is not satisfied, the thermal energy would provide enough energy required for an electron to tunnel, thus rendering electron control across the tunneling junction impossible.

2.3 Simulating Single-electron Devices

Simulating single electron devices involves calculating the free energy of the system, bearing in mind that tunneling takes place only if the energy after the tunneling event takes a smaller value. Further more, electron tunneling is a probabilistic process, which has to be incorporated in the simulation process. To simulate single electron circuits, two prominent methods have been widely studied: simulation by Monte Carlo and the Master Equation methods.

Simulation by the Master Equation method [7] assumes that tunneling depends on the momentarily state of the circuit and that the transition takes place at random times. This can be expressed by the equation

$$\frac{\partial P_i(t)}{\partial t} = \sum \left[\Gamma_{ij} P_j(t) - \Gamma_{ji} P_i(t)\right] , \tag{2.5}$$

where Γ_{ij} shows the rate of transition form state j to state i and $P_i(t)$ is the time dependent occupation probability of state i.

The Monte Carlo method [6] calculates the probability of an electron tunneling across a particular junction, by considering the charge in the intermediate node. To calculate the tunneling rate, firstly, one has to calculate the free energy (ΔE_i) for each and every node in the circuit, which is expressed as

$$\Delta E_i = \sum_i \frac{(Q_i)^2}{2C_i} - \sum_i \frac{(Q_i - \Delta Q_i)^2}{2C_i} + \sum_i \Delta Q_i V_i \tag{2.6}$$

where Q_i is the charge on the *i*th node, ΔQ_i is the change in the circuit charge after tunneling takes place, and $\Delta Q_i V_i$ is the energy dissipated by the bias voltage V_i. Secondly, the average tunneling rate Γ_i, expressed in terms of the free energy and the tunneling resistance R_t, is computed as

$$\Gamma_i = \frac{1}{e^2 R_\mathrm{t}} \frac{\Delta E_i}{1 - \exp[-\Delta E_i / k_\mathrm{B} T]} , \tag{2.7}$$

which at temperature T = 0 K reduces to

$$\Gamma_i = \begin{cases} \frac{1}{e^2 R_\mathrm{t}}, & \Delta E_i > 0 \\ 0, & \Delta E_i \leq 0 \end{cases} \tag{2.8}$$

The Monte Carlo method itself generates random numbers to simulate stochastic models. Since single electron tunneling is a probabilistic event, the Monte Carlo method is used to calculate the waiting time (t_i) between when the tunneling conditions are met and the actual tunneling event. To do so, we take the reciprocal of the tunneling rate and multiply this with a random number r $(0 < r < 1)$ to obtain t_i as

$$t_i = \frac{1}{\Gamma_i} \ln[r] , \tag{2.9}$$

provided ΔE_i (Eq. 2.6) takes a positive value at that instant.

After calculating the waiting times for all the nodes, consider the node with the shortest waiting time and alter the node voltages accordingly. A simplified flow chart of the Monte Carlo method is shown in Fig. 2.5.

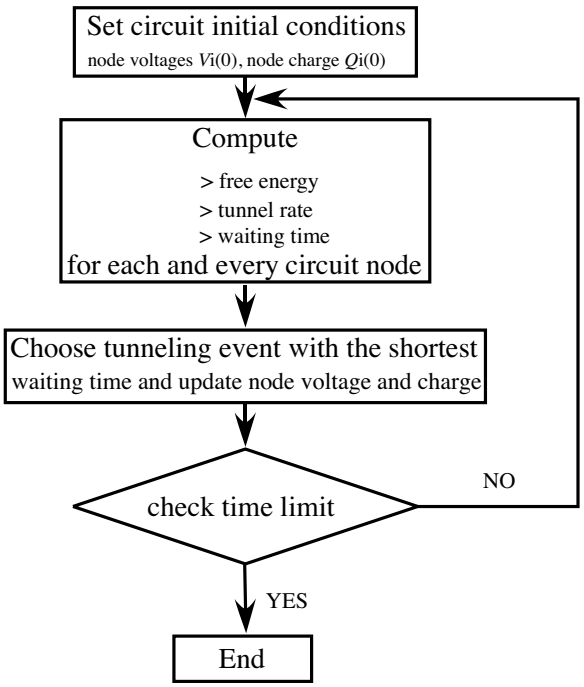

Figure 2.5: Flow chart of Monte Carlo method of simulating single-electron circuits.

References

[1] Gravert H. and Devoret M.H., "Single Charge Tunneling–Coulomb Blockade Phenomena in Nanostructures," *New York: Plenum*, 1992.

[2] Diesing, D. , Hassel, A. W., and Lohrengel, M. M., "Aluminium oxide tunnel junctions: influence of preparation technique, sample geometry and oxide thickness," Thin Solid Films 342, pp. 282-290, 1999.

[3] Tiwari, S., and Frank, D. J. , "Empirical fit to band discontinuities and barrier heights in III-V alloy systems," Applied Physics Letters 60, pp. 630-632, 1992.

[4] Ogura, M. , Wang, X. , Matsuhata, H., Tada, T., Hamoudi, A., Ikawa, S., Miyagawa, T. , and Takeyama, K. , "Fabrication of Quantum Wire and Minute Buried Heterostructure by In Situ Etching and Selective MOCVD Growth," Jpn. Journal of Applied Physics 35, pp. 1353?1357, 1996.

[5] Joyez, P., and Esteve, D., "Single-electron tunneling at high temperature," Physical Review B, 56, pp. 1848-1853, 1997.

[6] Kuwamura, N. , and Taniguchi, K. and Hamakawa, C., "Simulation of single-electron logic circuits," IEICE Trans. Electron., J77-C-II, pp. 221-228, 1994.

[7] Christoph Wasshuber, Computational Single-Electronics, *Wien: Springer-Verlag*, 2001.

3

Single Electron Oscillator

The elementary circuit used in this research—the single-electron oscillator, consists of a tunneling junction, connected in series with a high resistance. The single-electron oscillator produces relaxation oscillation dynamics, consisting of a continuous-time region and a discrete-time region. In the sections below, the configuration and operation principle of the single electron oscillator is explained in detail.

3.1 Operation of a Single-Electron Oscillator

The SET oscillation cell (Fig. 3.1) is a constituent element of our single-electron oscillator circuits. It consists of a tunneling junction (capacitance $= C_j$) and a high resistance R connected in series at node 1 and biased with a positive or a negative voltage V_d. At the low temperatures at which the Coulomb blockade effect is observed (i.e. temperature $\ll e^2/(k_B T C_j)$), the cell produces self-induced relaxation oscillation if $V_d > e/(2C_j)$, where e is the elementary charge and k_B is the Boltzmann constant. See K.K. Likharev *et al*., [18], and D.V. Averin *et al*., [19], [4] for detailed explanation. Figure 1(b) shows the waveform of the oscillation of voltage V_1 at node 1 for a positively biased cell. The node voltage gradually increases as junction capacitance C_j is charged through resistance R (curve AB). When the voltage reaches the threshold $e/(2C_j)$, it drops discontinuously to $-e/(2C_j)$ because of an electron tunneling from the ground to node 1 through the junction, again gradually increasing to repeat the same cycles. The dynamics is expressed by a combination of continuous differential equation $dV_1/dt = (V_d - V_1)/(RC_j)$ for charging curve AB and discrete difference equation $\Delta V = -e/C_j$ for discontinuous drop BC, where ΔV is the difference in the node voltage before and after tunneling. The period t_o of oscillation is $t_o = RC_j \ln(\frac{V_d + e/2C_j}{V_d - e/2C_j})$.

Strictly speaking, tunneling is a stochastic process with a probabilistic delay between when the node voltage exceeds threshold voltage $e/(2C_j)$ and when actual tunneling event takes place. Therefore, the period of oscillation shows probabilistic fluctuation expressed by $t_o + \Delta t$, where probabilistic delay or waiting time Δt

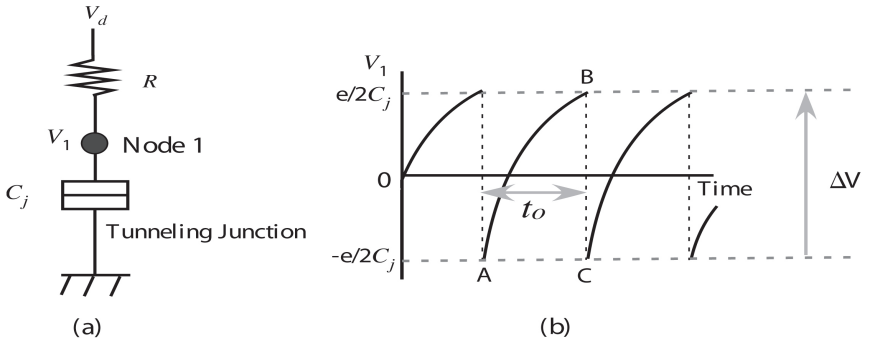

Figure 3.1: Single-electron tunneling (SET) cell: (a) circuit configuration and (b) waveform showing oscillation of node voltage V_1.

varies at every tunneling event. However, we have theoretically confirmed that waiting time decreases to a value far smaller than t_o (or $\Delta t/t_o \rightarrow 0$) as resistance *R* increases. We can consider normalised waiting time to be 0 if we use a sufficiently large resistance.

3.2 Simulating a single-electron oscillator

The following is an outline of the procedure of the Monte-Carlo simulation for single electron circuits used in this research. The single-electron oscillators are coupled to the neighboring each other though capacitors. This is in part an excerpt from [1]. Consider a circuit consisting of tunneling junctions (or tunneling capacitors), coupling capacitors, resistors, and biasing voltage sources. The internal state of the circuit is expressed by a set of charges on the nodes in the circuit. In the following, 'state' means this node-charge set. The voltage of each node can be calculated from the state.

To simulate the time-dependent behavior of the circuit, preset a time interval Δt for iteration; Δt is used to calculate the change in node charge caused by current flowing between bias voltages and nodes through resistors. The value of Δt determines time resolution of simulation. A small Δt increases the accuracy of simulation but requires a long computing time, resulting in a trade-off between the simulation time and precision. First, set time to 0 and give an initial charge to each node. Then simulate the circuit operation as follows.

Step 1: Update charge on each node. The updated charge q_i for node i is given by $q_i = q_{i0} + (V_{bi} - V_i)\Delta t/R_i$, where q_{i0} is the node charge before updating, V_{bi} is the bias voltage applied to node i through resistance R_i, and V_i is the voltage of node i. The state of the circuit changes from $(q_{10}, q_{20}, q_{30}, ...)$ to $(q_1, q_2, q_3, ...)$.

Step 2: Compute electrostatic energy E_0 (the sum of electrostatic energy of the tunneling junctions and coupling capacitors) for current state $(q_1, q_2, q_3, ...)$. Then enumerate all possible subsequent states and compute the electrostatic energy E_i for each subsequent state i. (Subsequent state i means a state into which the current state can be transformed by an electron tunneling between node i and the ground. If the number of the tunnel junctions is N, there are 2N possible tunnelings and therefore 2N subsequent states.)

Step 3: Compute the energy difference $\Delta E_i (= E_0 - E_i)$ for each subsequent state. Using the value of ΔE_i, calculate the waiting time for each tunneling event corresponding to each subsequent state. The waiting time τ_i is given by $\frac{1}{\Gamma_i} ln \frac{1}{\gamma}$ where γ is a uniform random number $(0 < \gamma < 1)$ generated for each tunneling event, and Γ_i is the mean tunneling rate (the mean number of electrons that tunnel in one second) given by $\frac{\Delta E_i}{e^2 R_T 1 - exp(-\Delta E_i / k_B T)}$, where R_T is the tunneling resistance of the tunneling junction, k_B is the Boltzmann constant, e is the elementary charge, and T is temperature.

Step 4: After calculating the waiting time τ_i for all possible tunnelings, take the shortest waiting time τ, and compare it to Δt.

(i) If $\tau > \Delta t$, no tunneling occurs. Put time forward by Δt and return to **Step 1** to repeat the iteration. (ii) If $\tau \leq \Delta t$, the tunneling event corresponding to τ occurs. Cancel the operations in **Step 1** and recalculate the updated charge on each node, using τ instead of Δt. The updated charge is given as $q_i = q_{i0} + (V_{bi} - V_i)\tau / R_i - e$ for the node that receives an electron (tunneling) from the ground, or as $q_i = q_{i0} + (V_{bi} - V_i)\tau / R_i + e$ for the node that sends an electron (tunneling) to the ground, and as $q_i = q_{i0} + (V_{bi} - V_i)\tau / R_i$ for all the other nodes. Then, put time forward by τ and return to **Step 1** to repeat the iterations.

References

[1] Kuwamura, N, Taniguchi, K., and Hamaguchi, C., ”Simulation of single-electron logic circuits,” IEICE Trans. Electron. J77-C-II pp. 221-8, 1994.

[2] Likharev, K., and Zorin, A. , “Theory of the Bloch-wave oscillations in small Josephson junctions,” J. of Low Temp. Phys. 59, 347?382, 1985.

[3] Averin, D., and Likharev, K. K. , “Coulomb blockade of single-electron tunneling, and coherent oscillations in small tunnel junctions,” J. of Low Temp. Phys. 62, 345-373, 1986.

[4] Likharev, K. K. , “Correlated discrete transfer of single electrons in ultrasmall tunnel junctions, and references therin,” IBM J. Res. Dev 32, 144-158, 1988.

【Part I 】

Introduction to nonlinear dynamics of single-electron networks

This chapter investigates non-linear behavior of coupled single-electron systems. In the first part, we focus on the terminology required in investigating the operation of non-linear systems. This is followed by detailed results on dynamical systems consisting of single-electron devices.

4

Dynamical Systems

A dynamical system is a system that evolves with time from a given initial state as defined by a certain rule. This rule is defined either by a set of difference equations or differential equations or a combination of both. Dynamical systems can be classified into two: discrete-time and continuous-time dynamical systems, according to how their dynamics are defined. In this chapter, we will start by giving details on discrete-time and continuous-time dynamical systems, then shift our focus to some useful terminology in describing dynamical systems.

4.1 Discrete-time Dynamical Systems

This is a system in which the evolution of system variables takes place in discrete time. The present state (x_{n+1}) of the system is determined by the preceding values of the system variables. That is

$$x_{n+1} = f(x_n, x_{n-1}, ..., x_1, x_0) \tag{4.1}$$

A widely studied discrete-time dynamical system is the discrete logistic system, whose dynamics is defined by the difference equation

$$x_{n+1} = \alpha x_n(1 - x_n) \tag{4.2}$$

for $0 \leq x \leq 1$, where α is a parameter.
To calculate the system's dynamics, choose a random initial state x_0, and calculate the values of x_{n+1}, according to Eq. 4.2. Depending on the parameter, the system's stable state changes from a steady state as in Fig. 4.1 (a) for $\alpha = 2.9$, to oscillating between 4 stable states (i.e. x_{n+1} repeats every 4 iterations) in Fig. 4.1 (b), for $\alpha = 3.5$, and for $\alpha > 3.56$ it oscillates in an irregular, aperiodic manner, never settling down to a periodic state (chaotic dynamics). A diagram showing the number of stable points for a wider range of bifurcation parameter α ($2.6 < \alpha < 4$) is shown in section 4.5.

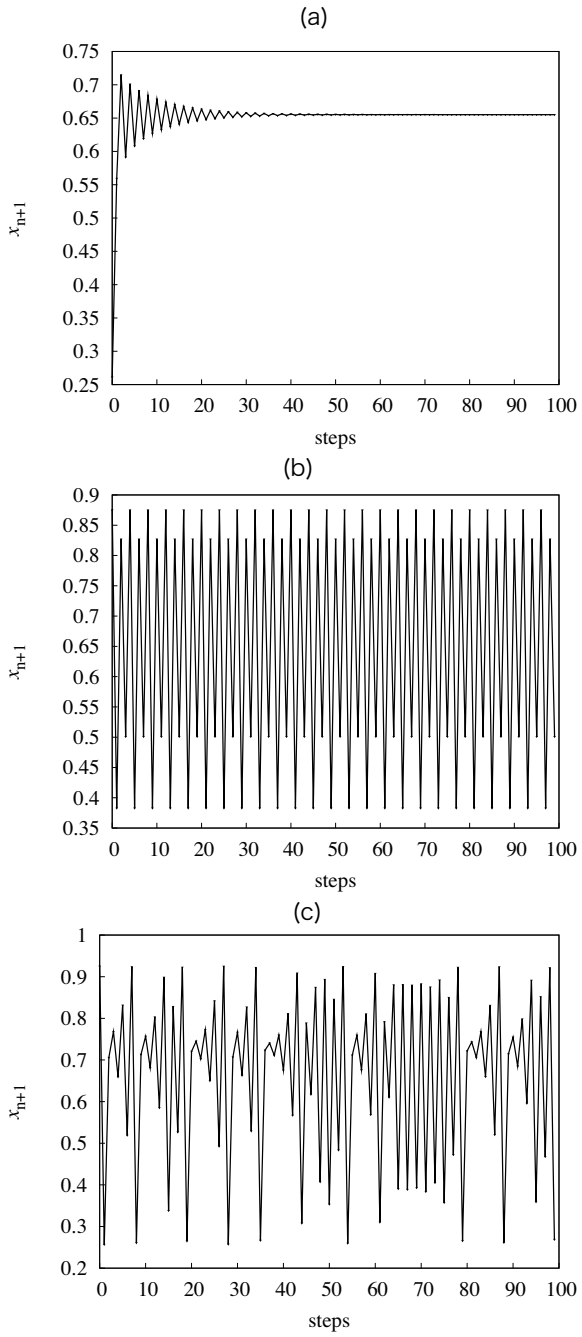

Figure 4.1: Logistic map: gradual evolution of x_n, plotted for bifurcation parameter $\alpha = 2.9$ for (a), $\alpha = 3.5$ for (b) and $\alpha = 3.7$ for (c).

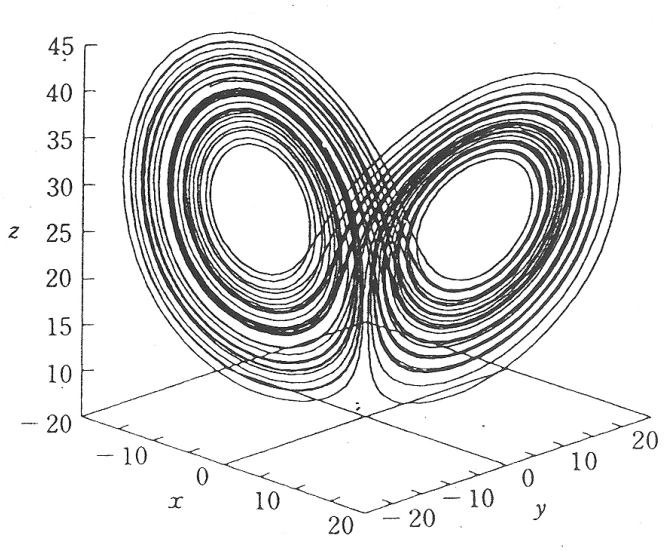

Figure 4.2: Strange attractor defined by Lorenz equations, with parameters set to $\sigma = 10$, $b = 8/3$ and $r = 28$.

4.2 Continuous-time Dynamical Systems

This class of dynamical systems is governed by ordinary differential equations, evolving in continuous time. The variables of the system evolve as

$$\frac{d\mathbf{X}(t)}{dt} = F(\mathbf{X}(t)). \tag{4.3}$$

An example of continuous-time dynamical system is the Lorenz map, a 3-dimensional system. It is described by Lorenz equations:

$$\begin{aligned} \tfrac{dx}{dt} &= \sigma(y - x) \\ \tfrac{dy}{dt} &= rx - y - xz \\ \tfrac{dz}{dt} &= xy - bz, \end{aligned} \tag{4.4}$$

where σ, r and $b \geq 0$ are parameters. This system portrays highly erratic dynamics, over a wide range of parameters. The stable points of the system oscillate irregularly, never repeating, but remain in a bounded region in a x-y-z space. The Lorenz system is renowned for its dependence on the initial conditions. Fig. 4.2 shows a trajectory obtained by setting the system parameters to $\sigma = 10$, $b = 8/3$ and $r = 28$, for a sample set of inital conditions $x(0), y(0), z(0)$.

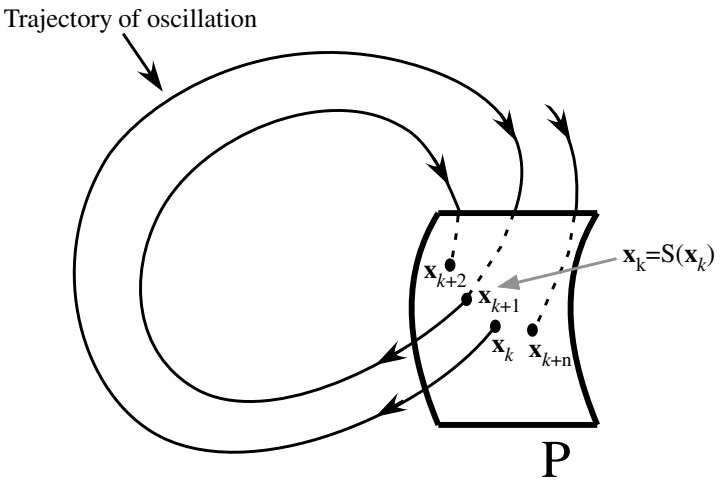

Figure 4.3: Poincare section.

4.3 Attractor

A system could settles down to some stable state which could be defined by a fixed point, or a trajectory. Such a set of points describing the final state, to which all the neighboring trajectories of an oscillation converge is referred to as the attractor of oscillation.

4.4 Poincaré Section

The Poincaré section is utilized in analyzing dynamics of an N-dimensional system, by using a transversal hyper-surface of a lower (N-1)-dimension, where $N \geq 3$, projected in such a way that all the trajectories of (or sections of trajectories describing) the oscillation flow through the surface (see Fig. 4.3). In particular, Poincaré sections are useful in studying the qualitative aspect of the flow of periodic trajectories of an oscillation. Consider a trajectory emerging from an initial state $\mathbf{x}_0$ on the Poincaré section. By following the trajectory, and plotting all the points at which it intersects the surface, you obtain the Poincaré map. If $\mathbf{x} \in \mathbf{S}$ denotes the *k*th intersection, the Poincaré map can be defined by

$$\mathbf{x}_{k+1} = \mathbf{S}(\mathbf{x}_k). \tag{4.5}$$

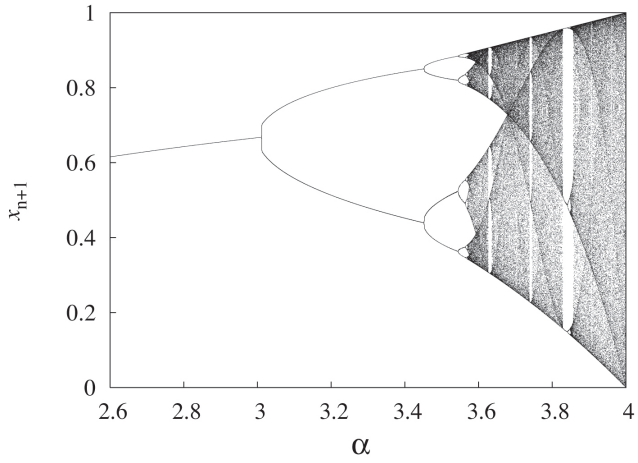

Figure 4.4: Bifurcation diagram of the logistic map, for $2.6 < \alpha < 4$

4.5 Bifurcation

The dynamics of a dynamical system depend on the system's parameters. By changing the parameters, the stability of the system also evolves to portray a number of dynamics. This includes qualitative change in the stability of a system: topological structure of the trajectory (attractor) of oscillation, or the number of stable states. Such a change is referred to as bifurcation.

As an example, we take the discrete logistic system (sec. 4.1), and study its stability, keeping our attention to how the number of stable states increase or decrease with increase in the system parameter α.

By plotting these stable points, against the respective values of parameter α, a bifurcation diagram showing the qualitative behavior of the dynamical system is obtained.

As the parameter increases from 2.6, we observe an increase in the number of stable points from 1 for parameter setting of $\alpha < 3 \rightarrow 2$ $(3 \leq \alpha < 3.449) \rightarrow$ 4 $(3.449 \leq \alpha < 3.544) \rightarrow 8$ $(3.544 \leq \alpha < 3.564)$ and so forth. At $\alpha > 3.56$, the system becomes chaotic, and possesses a considerably large number of stable points.

4.6 Summary

In this chapter, we restricted ourselves to a brief explanation of terminology in describing and analyzing non-linear behavior of dynamical systems. For a comprehensive explanation, we would refer the reader to *Nonlinear Dynamics and Chaos* [1] and *Chaos in dynamical systems* [2].

References

[1] Strogatz, S.H., Nonlinear Dynamics and Chaos, Westview Press, Cambridge, Massachusetts, 1994.

[2] Ott, E., Chaos in dynamical systems, Cambridge University, Cambridge, Massachusetts, 1993.

5

Coupled Oscillator Systems

5.1 Introduction

Single-electron oscillators exhibit complex dynamics when coupled with one another. As an example of such coupled oscillators, this chapter describes the structure and behavior of two dynamical systems consisting of two single-electron oscillators capacitively coupled with each other to form a double oscillator and two double-oscillators coupled together to form a quardruple oscillator system. This chapter gives details on the configuration and wide variety of nonlinear dynamics of such a system. To illustrate the dynamics, attractors of oscillation plotted on phase diagrams, bifurcation diagrams obtained by varying the system's parameter are utilized.

5.2 Double Oscillator System

5.2.1 Circuit configuration and operation

The double-oscillator circuit consists of two single-electron oscillators coupled with each other through a capacitance. Fig. 5.1 shows the circuit configuration. One oscillator consists of a resistor R_1 and a left tunneling junction C_j biased with a positive voltage $V_{\rm dd}$. The other oscillator consists of a resistor R_2 and a right tunneling junction C_j biased with a *negative* voltage $-V_{\rm dd}$. The two oscillators are coupled with each other at nodes 1 and 2 through a coupling capacitor *C*. The variables of the circuit are node voltages V_1 and V_2. The threshold of the junction voltages for tunneling is $\pm(C + C_j)/(2C_j(2C + C_j))$ for this circuit, and electron tunneling occurs through the corresponding junction if either of the node voltages reaches the threshold.

Coupled through capacitor *C*, the two oscillators interact with each other to produce synchronization and entrainment. Figure 4 depicts an example of the operation on a V_1-V_2 phase plane. Node voltages V_1 and V_2 change continuously as the junction capacitances are charged through the resistances. When either of

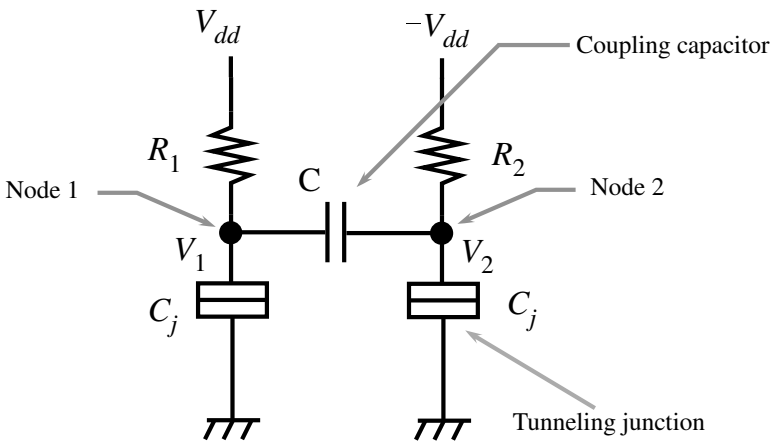

(a)

Figure 5.1: Double oscillator system consisting of two tunneling cells coupled through capacitance *C* and biased with positive and negative power voltages $V_{\rm dd}$ and $-V_{\rm dd}$.

the node voltages reaches the threshold, tunneling occurs through the corresponding junction, and this causes a discrete change in both node voltages. For instance, the trajectory of oscillation starts at point 1, proceeds rightward to 2, then it jumps discontinuously to 3 because of electron tunneling in the left junction, proceeds to 4, jumps to 5 (tunneling in the left junction, followed by immediate tunneling in the right junction), proceeds to 6, jumps to 7 (tunneling in the right junction), proceeds to 8, and finally returns to 1 (tunneling in the left junction, followed by immediate tunneling in the right junction). Thus, the circuit produces a periodic oscillation in which discrete-time and continuous-time dynamics coexist.

5.2.2 Simulating the dynamics of the Double-Oscillator circuit

To express the dynamics of the coupled oscillators, the variables and parameters were rewritten by using equations,

$$\begin{aligned} u &= \frac{2C_0}{e}V_1,\ \ v=\frac{2C_0}{e}V_2,\ \ C_0=\frac{(2k+1)}{(k+1)}C_j,\ \ k=\frac{C}{C_j}, \\ \alpha &= \frac{R_2}{R_1},\ \ \beta=\frac{2C_0}{e}V_{dd},\ \ \text{and}\ \ t=\frac{\text{time}}{R_1C_0}. \end{aligned} \tag{5.1}$$

where, u and v are normalized node voltages, k is the coupling coefficient $(k \geq 0)$, α is the resistance ratio $(\alpha > 1)$, β is normalized bias power voltage

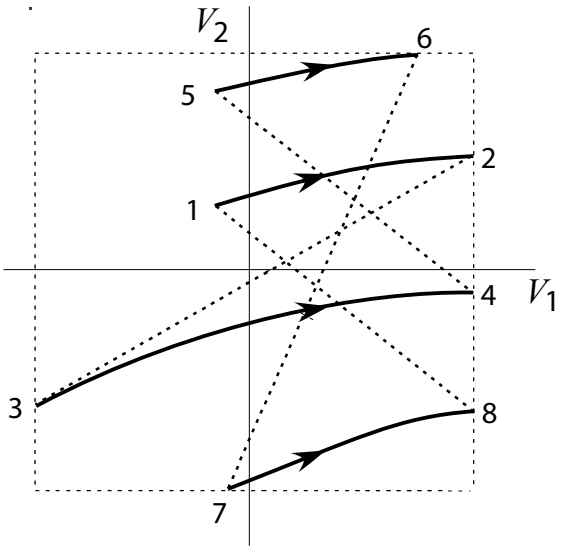

(b)

Figure 5.2: Schematic trajectory of the oscillation in the coupled oscillators, plotted on a V_1-V_2 phase plane. Dashed lines show a discrete change caused by tunneling.

($\beta > 0$), and *t* is normalised time. The dynamics of the circuit, which depend entirely on the dimensionless parameters α, β, and k, can be expressed with a trajectory on a u-v phase plane. Taking into account the Coulomb blockade, the following equations for the dynamics were obtained. The normalised threshold voltage for tunneling is ± 1. The operation is continuous-time in a range of $-1 < u \ < 1$ and $-1 < v \ < 1$ and is given by differential equations,

$$\frac{du}{dt} = (\beta - u) - \frac{k}{k+1}\frac{1}{\alpha}(\beta + v), \quad (5.2)$$

$$\frac{dv}{dt} = \frac{k}{k+1}(\beta - u) - \frac{1}{\alpha}(\beta + v). \quad (5.3)$$

When either u or v reaches the threshold ± 1, tunneling occurs in the corresponding junction and node voltages u and v change discretely by Δu and Δv,

where

$$\begin{aligned}
\Delta u &= -2 \text{ and } \Delta v = -\frac{2k}{k+1} \text{ if } u \text{ reaches } 1, \\
\Delta u &= 2 \text{ and } \Delta v = \frac{2k}{k+1} \text{ if } u \text{ reaches } -1, \\
\Delta u &= -\frac{2k}{k+1} \text{ and } \Delta v = -2 \text{ if } v \text{ reaches } 1, \\
\Delta u &= \frac{2k}{k+1} \text{ and } \Delta v = 2 \text{ if } v \text{ reaches } -1.
\end{aligned} \tag{5.4}$$

Attractors on the u-v phase plane

The operation of the coupled oscillators for sample sets of parameters was simulated and the trajectory of the oscillation was plotted on u-v phase planes. The trajectory depended on initial values of u and v but was attracted, as time passed, to a set of curves (i.e., the attractor of the oscillation) independent of the initial values. Figures 5.3 (a) through 5.3 (d) show the attractor for $\alpha = \sqrt{10}$ and $\beta = 3$, with coupling coefficient k as a parameter. As the figures show, a slight change in the coupling coefficient produces a drastic change in oscillation cycle. The flow of the attractor can be simply expressed with the values of v at which segments of the attractor meet line $u = 1$. For instance, the flow in Fig. 5.3 (b) can be expressed with a sequence of 17 values of v. This is one kind of Poincaré map, and no information is lost in terms of the qualitative behavior of the dynamics. The set of these v values were used to draw bifurcation diagrams in the next section. The number of these v values are referred to the degree of periodicity in oscillation.

Effect of the coupling coefficient and the resistance ratio on the dynamics

To come up with a general view of the effect of coupling coefficient k and resistance ratio α on the dynamics, bifurcation diagrams were drawn by plotting the set of the v values as a function of k and α. Figure 5.4 shows a bifurcation diagram with k as a bifurcation parameter. The resistance ratio was set to $\alpha = 3$ for (a) and $\alpha = \sqrt{10}$ for (b), and the bias power voltage was $\beta = 3$ for both diagrams. At k = 0 (without coupling), the two oscillators in the circuit produced a self-induced oscillation independent of each other. As coupling coefficient k increased, the oscillators began to interact with each other to produce entrainment and synchronized periodic oscillation. Generally speaking, the degree of periodicity increased with the increase of k. However there were many windows where the degree of periodicity decreased drastically. The windows appeared irregularly and repeatedly.

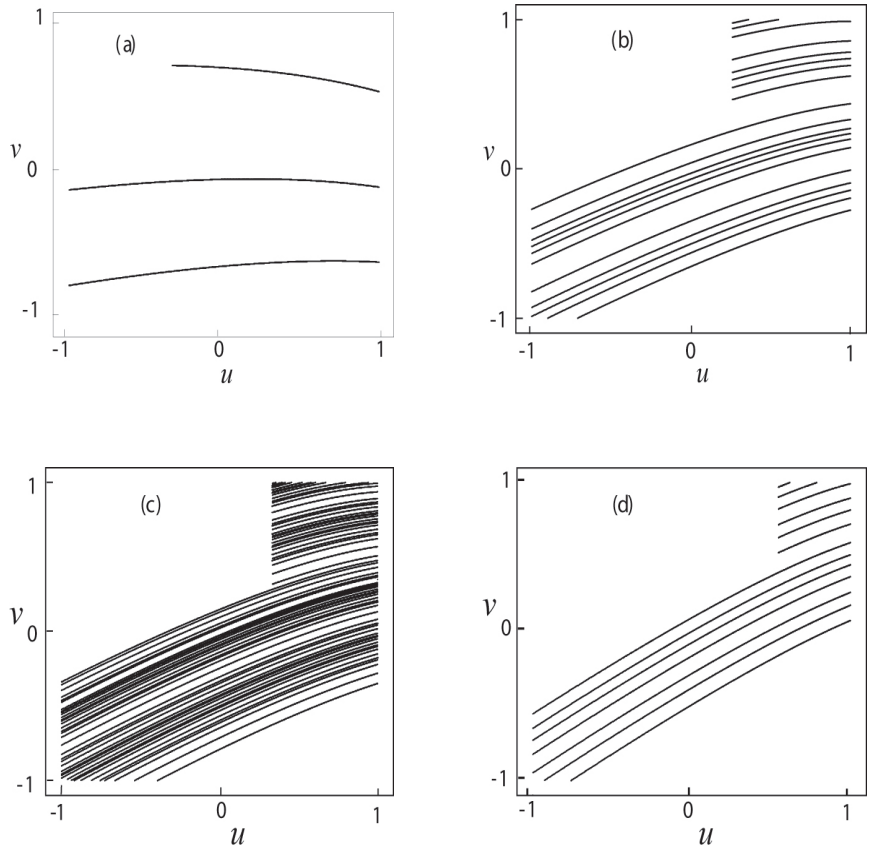

Figure 5.3: Attractors of the oscillation plotted on a u-v plane, simulated with coupling coefficients (a) k = 0.5 (3-cycle oscillation), (b) k = 1.7 (19-cycle), (c) k = 2 (58-cycle), and (d) k = 3.5 (13-cycle). The resistance ratio $\alpha = \sqrt{10}$ and bias power voltage $\beta = 3$ for all figures.

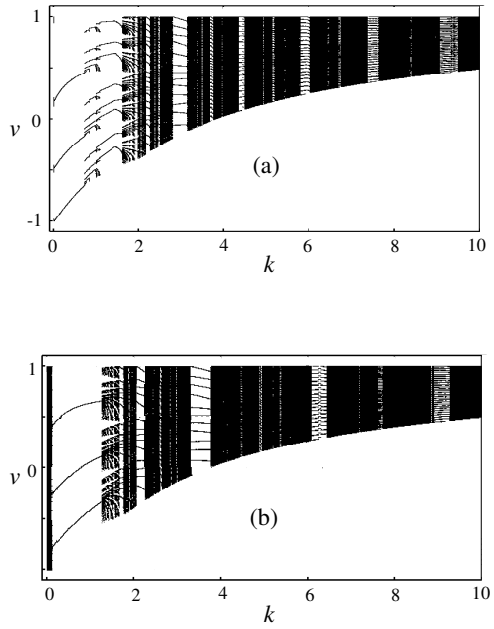

Figure 5.4: Bifurcation diagram with coupling coefficient k as a parameter. Resistance ratio is (a) $\alpha = 3$ and (b) $\alpha = \sqrt{10}$. Power voltage $\beta = 3$ for both diagrams.

As a second parameter of this circuit, the resistance ratio α was considered and the change of the system dynamics with increase in α were studied. The results are shown in Fig. 5.5.The coupling coefficient and the power voltage were set to $k = 0.2$ for (a) and $k = 1$ for (b), with $\beta = 3$ for both diagrams. The degree of periodicity increased as α increased, but windows also appeared repeatedly. In each window, the degree of periodicity is equal to the nearest integer value of α.

5.3 Quadruple Oscillator System

This section describes, in detail, the structure and behavior of a quadruple-oscillator system. Similarly to the double oscillator described in the previous section, the quadruple system produces a multi-periodic oscillation. However, unlike the double system, whose oscillation settled to the same trajectory –a single attractor–independent of the initial state it starts from, the quadruple system has a number of possible attractors and takes one of them determined by initial conditions of its 4 nodes.
The sections to follow, elaborate this more thoroughly with the use of phase diagrams and diagrams showing basins of attraction for different initial conditions and parameter settings.

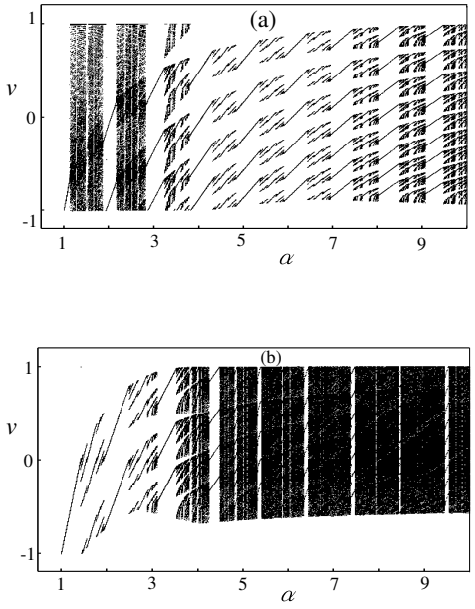

Figure 5.5: Bifurcation diagram with resistance ratio α as a parameter. The coupling coefficient is (a) k = 0.2 and (b) k = 1. Power voltage $\beta = 3$ for both diagrams.

5.3.1 Structure of the Quadruple-Oscillator system

Coupling two double-oscillator circuits will produce a new system with more complex dynamics. Figure 5.6 shows such a quadruple-oscillator system consisting of four oscillators—two are *positively* biased with V_{dd} and the other two are *negatively* biased with $-V_{dd}$. The oscillators are connected in a ring through coupling capacitors C so that electron tunneling in one oscillator will induce tunneling in the two adjacent oscillators. The variables of this system are four node voltages V_1, V_2, V_3, and V_4.

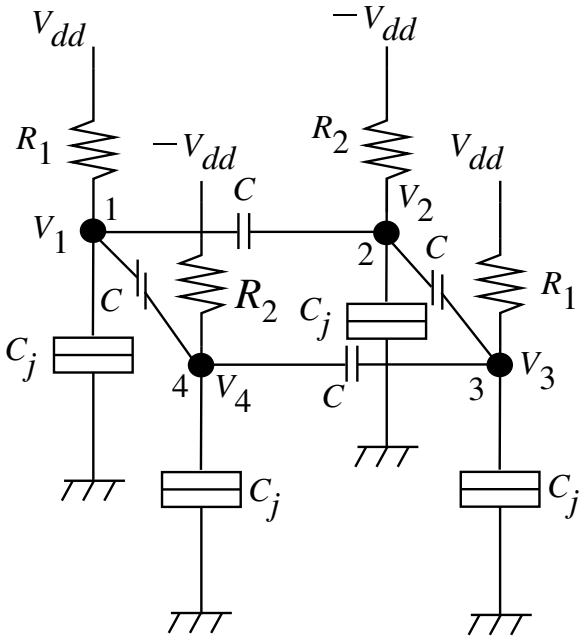

Figure 5.6: Quadruple oscillator circuit consisting of two double-oscillator circuits coupled through capacitors *C*.

5.3.2 Expressing the system dynamics

To express the dynamics of this circuit, the variables and parameters were rewritten as

$$\begin{aligned} u_i &= \frac{2C_s V_i}{e} \quad (i = 1{-}4), \\ C_s &= \frac{(8k^2 + 6k + 1)C_j}{(2k^2 + 4k + 1)}, \\ k &= \frac{C}{C_j}, \quad \alpha = \frac{R_2}{R_1}, \\ \beta &= \frac{2C_s}{e} V_{dd}, \quad \text{and} \quad t = \frac{\text{time}}{R_1 C_s}, \end{aligned} \tag{5.5}$$

where, u_i is the normalized voltage of the ith node, k is the coupling coefficient ($k \geq 0$), α is the resistance ratio ($\alpha > 1$), β is the normalized bias voltage ($\beta > 0$), and *t* is normalised time.
With this rewriting, the dynamics of the system were calculated . In a range of $-1 < u_i < 1$ (*i* = 1-4), the system dynamics are given by differential equations

$$\begin{aligned}
\frac{du_1}{dt} &= -\frac{2(\gamma+\zeta-\kappa-\eta)k^2+(-4\kappa+\gamma+\zeta)k-\kappa}{(4k+1)(2k+1)} \\
\frac{du_2}{dt} &= -\frac{2(\gamma+\zeta-\kappa-\eta)k^2+(4\gamma-\kappa-\eta)k+\gamma}{(4k+1)(2k+1)} \\
\frac{du_3}{dt} &= -\frac{2(\gamma+\zeta-\kappa-\eta)k^2+(-4\eta+\zeta+\gamma)k-\eta}{(4k+1)(2k+1)} \\
\frac{du_4}{dt} &= -\frac{2(\gamma+\zeta-\kappa-\eta)k^2+(4\zeta-\kappa-\eta)k+\zeta}{(4k+1)(2k+1)} \ ,
\end{aligned} \tag{5.6}$$

where

$$\begin{aligned}
\gamma &= \frac{\beta+u_2}{\alpha}, \quad \zeta = \frac{\beta+u_4}{\alpha} \\
\kappa &= \beta-u_1, \quad \eta = \beta-u_3.
\end{aligned} \tag{5.7}$$

When any of node voltages u_i reaches the threshold value of ± 1, an electron tunnels at the corresponding node, and this leads to a discrete change in node voltages of the four nodes of the system. For instance, if u_1 reaches +1, tunneling occurs in oscillator 1 from the ground to node 1. This produces a discontinuous change in node voltage given by difference equations

$$\Delta u_1 = -2 \tag{5.8}$$

for node 1,

$$\Delta u_2 \ \text{ and } \ \Delta u_4 = -\frac{2k(2k+1)}{2k^2+4k+1} \tag{5.9}$$

for the two adjacent nodes 2 and 4, and

$$\Delta u_3 = -\frac{4k^2}{2k^2+4k+1} \tag{5.10}$$

for the diagonally positioned node 3. In case u_1 decreases to -1, electron tunnels from node 1 to the ground, and the change is positive for every node voltage. Tunneling at any other node leads to a similar change in the four node voltages.

5.3.3 Simulation results - basin diagrams -

The operation of the quadruple-oscillator circuit was simulated for various parameter settings and found that this system showed multi-periodic oscillation with a number of possible attractors instead of a single attractor. The attractor the system actually took was determined by the initial values of the four node

voltages u_i ($i = 1$-4); in other words, some initial conditions evolve to a certain attractor, and other initial conditions evolve to a different attractor.
To understand the relationship between the initial node conditions of this system and the attractor of oscillation, we need to draw four-dimensional basin diagrams for various parameter settings.
Figure 5.7 shows an example of a simplified two-dimensional basin diagram for a sample parameter setting of $k = 1$, $\alpha = \sqrt{10}$, and $\beta = 3$. It was drawn as follows:
•***step 1*:** The attractor of oscillation was calculated and plotted on a four-dimensional u_1-u_2-u_3-u_4 phase space for a given initial condition $(u_{01}, u_{02}, u_{03}, u_{04})$, where u_{0i} are the initial values of node voltages u_i. For simplicity, the initial voltages of nodes 1 and 3 (and initial voltages of nodes 2 and 4) were assumed to be the same in amplitude but inverse in polarity: i.e., $u_{03} = -u_{01}$ and $u_{04} = -u_{02}$. Therefore initial conditions can be plotted on an u_1-u_2 plane.
•***step 2*:** The calculated attractor was orthogonally projected onto the u_1-u_2 plane to reduce its dimensions. The projected attractor consisted of a number of curve segments on the u_1-u_2 plane. Figures 5.7(a) and 5.7(b) show the projected attractor for two sample initial conditions.
•***step 3*:** Steps 1, 2 and 3 were repeated many times to obtain projected attractors for various initial conditions.
•***step 4*:** The basins of attraction for the projected attractors were depicted on a u_1-u_2 plane.
The resultant basin diagram is Fig. 5.7 (c). The sample system has three possible attractors; the first is shown by Fig. 5.7 (a), the second is shown by Fig. 5.7 (b), and the third is similar to Fig. 5.7 (b) but the number of curve segments is somewhat smaller. The attractor actually taken was determined by the initial conditions: that is, initial conditions in region A in Fig. 5.7 (c) lead to the first attractor (Fig. 5.7 (a)), initial conditions in region B lead to the second attractor (Fig. 5.7 (b)), and initial-conditions in region C lead to the third attractor.
Figure 5.8 shows the whole of the basin diagram on a u_1-u_2 plane ($-1 < u_1 < 1$ and $-1 < u_2 < 1$). The shaded regions are the basins of the first attractor (Fig. 5.7 (a)), and non-shaded regions are the basins of the second and the third attractors (these two are labyrinthine and undistinguishable on the figure).
Figure 5.9 shows another example, calculated with a parameter setting of $k = 3.6$, $\alpha = \sqrt{10}$, and $\beta = 3$. Also three possible attractors exist. The shaded regions in Fig. 5.9(a) are the basins of one attractor (Fig. 5.9(b)) and non-shaded regions are the basins of the other two attractors (one is shown in Fig. 5.9(c)).

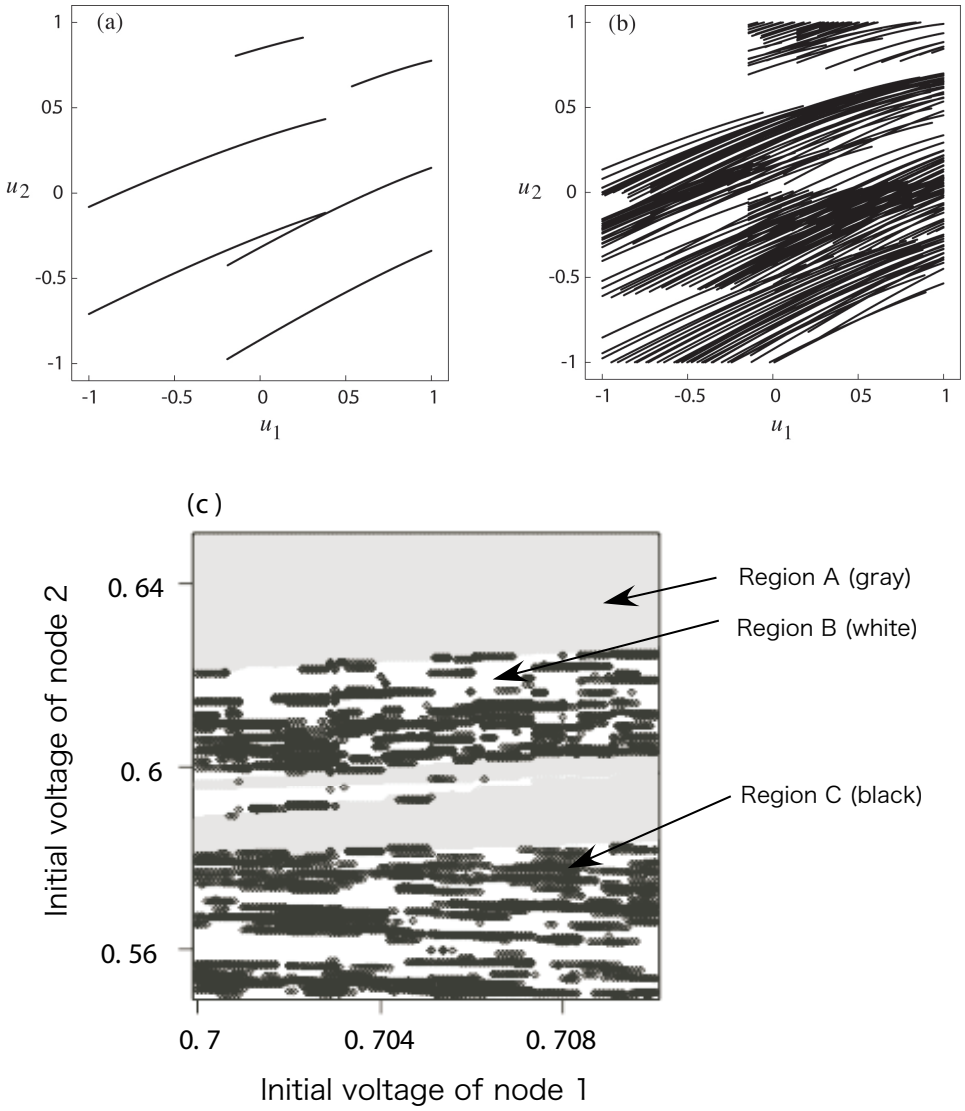

Figure 5.7: Attractors and basins of the quadruple-oscillator circuit, simulated with a parameter setting of $k = 1$, $\alpha = \sqrt{10}$ and $\beta = 3$. (a),(b): two of the three attractors projected onto a u_1-u_2 plane, and (c) basin for the attractors. Regions A, B, and C are the attracting basins for the first (Fig. 5.7(a)), the second (Fig. 5.7(b)) and the third attractors respectively.

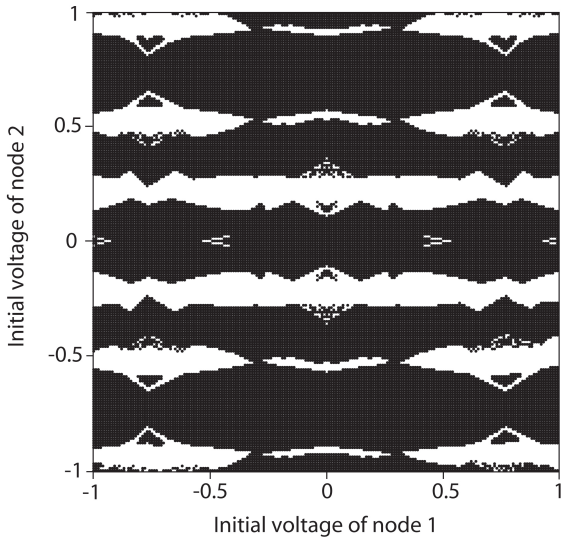

Figure 5.8: The whole of the basin diagram for a parameter setting of $k = 1$, $\alpha = \sqrt{10}$ and $\beta = 3$. Shaded regions are the basins of the first attractor (a), and non-shaded regions are the basins of the second (b) and the third attractors.

5.4 Summary

The first part of this thesis focused on analyzing the non-linear dynamics of coupled single-electron devices. Understanding the principles and the non-linear dynamics of such devices is inevitable in creating novel architectures for the next generation of LSI systems consisting of single-electron devices. To accomplish this, we proposed a basic circuit– the single-electron oscillator, with which we designed two sample dynamical systems: a double- and a quadruple-oscillator system and illustrated their rich dynamics with phase diagrams, bifurcation diagrams and basins of attraction diagrams. Though the structure of these systems is very simple, they showed a wide variety of non-linear dynamics. Through computer simulations, we confirmed that the complexity of system's operation increases with the number of coupled oscillators. We observed that
① a single oscillator shows only simple relaxation oscillation, when biased to a voltage higher than the threshold,
② the double-oscillator system produces multi-periodic oscillation with a single attractor, and
③ the quadruple oscillator system also produces multi-periodic oscillation but has a number of possible attractors and takes one of them, as determined by the initial conditions.

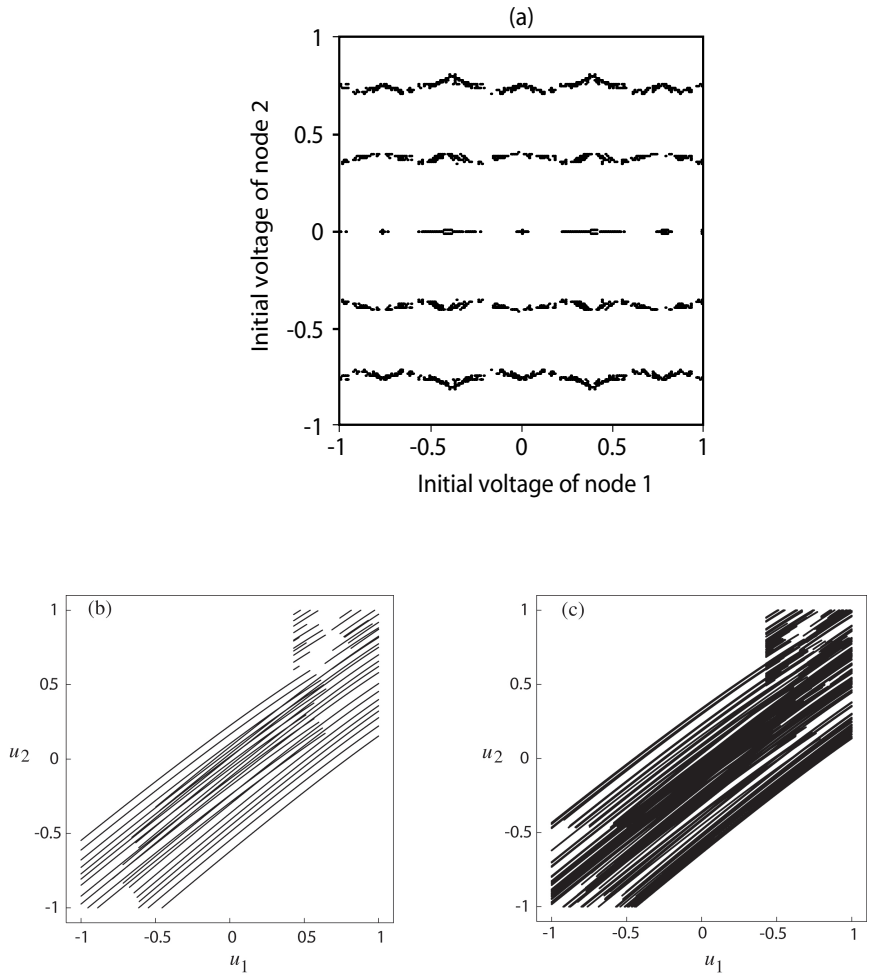

Figure 5.9: Basin diagram (a) for a parameter setting of $k = 3.6$, $\alpha = \sqrt{10}$, and $\beta = 3$. Three possible attractors exist. Shaded regions in (a) are the basin of one attractor (b) and non-shaded regions are the basins of the other two attractors (one is shown in (c).

References

[1] Gravert, H., and Devoret, M. H., *Single Charge Tunneling—Coulomb Blockade Phenomena in Nanostructures* New York: Plenum, 1992.

[2] Oya, T., Asai, T., Fukui, T., and Amemiya, Y., "Reaction-diffusion systems consisting of single-electron circuits," Int. J. of Unconventional Computing 1 pp. 177-94, 2005.

【Part II 】

LSI architectures employing structural properties of single-electron devices

This part focuses on how to utilize the minute sizes of single-electron devices to applications that require high spatial resolutions. As an example we propose a two-dimensional photon sensor that can detect the position of incoming photons with a spatial resolution of a few nano meters. The sensor also actively uses capacitive coupling between single-electron devices to propagate signals (in form of an electron tunneling wave) amongst individual units within itself. By detecting the arrival time at the periphery of the device network, we can precisely determine the position at which the photon entered the device.

6

Two-dimensional photon position sensor

6.1 Introduction

A promising area of research in microphotonics is the development of solid-state sensors that can detect the position of incident single photons with high spatial resolution. This chapter discusses a two-dimensional photon sensor consisting of single-electron integrated circuits.

Detecting the position of incident photons is a fundamental, important process in spectroscopic and imaging measurement in physical, chemical, and biological sciences. The existing device used for this purpose is the microchannel plate photomultiplier (MCP) [1], [2], [3] —a two-dimensional array of millions of small photomultiplier tubes, each tube with a diameter of several micrometers. The MCP is a superior device with a high sensitivity and a large signal-to-noise ratio. Its spatial resolving power, however, is determined by the channel diameter (or pitch: center-to-center spacing) which is typically in the range of 10 μm. A MCP consists of a bundle of fine glass capillaries that conduct incoming electrons from the input plate toward the output. A cross section of a MCP is show in figure 6.1 (a), while its operation principle is shown in figure 6.1 (b). As shown in figure 6.1 (b), an incoming electron enters a channel, and is accelerated along the channel by the accelerating voltage V. The incoming electron induces secondary electrons on hitting the channel inner wall. The secondary electrons are also accelerated and induce more secondary electrons producing a cascade of secondary electrons that propagates toward the opposite face of the MCP plate. This amplifies the original input (few electrons) by several orders. The output signal is detected either by using a metal anode measuring total current or in some applications each channel is monitored independently with a phosphor screen to produce an image.

Far higher resolution can be achieved using an array of single-electron tunneling junctions. A single-electron tunneling junction can operate as a minute photon

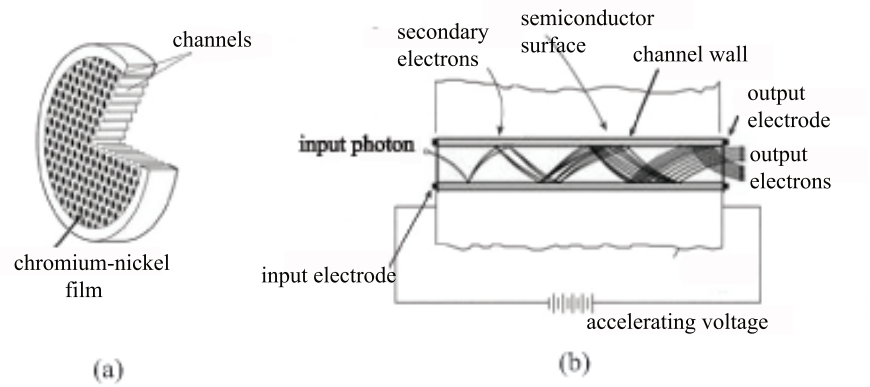

Figure 6.1: Microchannel Plate photomultiplier: (a) Cross section showing a bundle of microchannels (b) Operation principle: incoming photon strikes the microchannel channel inner wall, producing a secondary electrons which in turn hit the channels walls producing more secondary electrons as the are accelerated along the channel.

detector based on the photo-induced charging effect (see [20] , [21] and [6] for details). Therefore, arranging many tunneling junctions into an array will create a novel two-dimensional position sensor for photons. Junction arrays with a tens-nanometer arrangement pitch can be fabricated using existing nano process technologies, so one can develop a position sensor with a high resolving power of 0.01-0.1 μm—a far higher resolution than that of MCPs.

The challenge in the development of this sensor is related to the accurate determination of the two-dimensional position of incident photons. Unlike conventional devices, it is difficult to lay row-column access lines through closely arranged, minute tunneling junctions. Even if one could do that, the large parasitic capacitance of the access lines would impede the single-electron operation of the tunneling junctions.

To solve this problem, we developed a method of detecting positions that makes use of the propagation of tunneling waves in a tunneling junction array. The proposed photon sensor consists of many single-electron tunneling oscillators regularly arrayed on a plane, where each oscillator is coupled with neighboring oscillators. If a photon hits and excites an oscillator, photo-induced tunneling occurs in the oscillator. This induces tunneling in neighboring junctions, and the tunneling events successively propagate, like a wave, in all directions to reach the periphery of the sensor. By measuring the arrival time of the wave at several points on the periphery, one can determine the starting point of the wave and therefore know the position at which the photon entered the sensor.

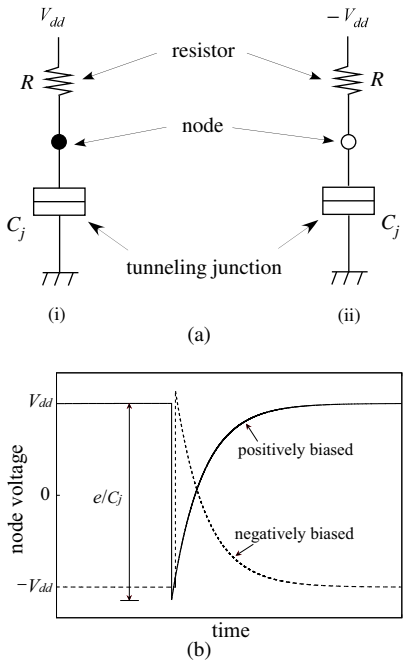

Figure 6.2: Single electron oscillators biased with (a-(i)) positive voltage V_{dd} and (a-(ii)) negative voltage $-V_{dd}$, and (b) monostable, or one-shot, operation of positively biased (solid line) and negatively biased (dashed line) oscillators.

In the following sections, first the structure of the proposed sensor is described. Then its operation is illustrated using the results of Monte-Carlo based computer simulation. Tunneling wave's generation, propagation, and arrival at the device periphery are simulated. We show that the starting position of the wave can be determined using the arrival time of the wave.

6.2 Structure of sensor device

To make the photon position sensor, we use a network of single-electron oscillators. A single-electron oscillator, shown in Fig. 9.8, is a simple circuit consisting of a tunneling junction C_j and a high-resistance resistor R connected in series at a node and biased with a positive voltage V_{dd} (Fig. 9.8(a-(i))) or a negative voltage $-V_{dd}$ (Fig. 9.8(a-(ii))). It operates as a relaxation oscillator at low temperatures at which the Coulomb-blockade effect occurs. The oscillator is astable if $V_{dd} > e/(2C_j)$ (e is the elementary charge) and monostable if $V_{dd} < e/(2C_j)$ (see [18] and [17] for detailed explanation). The node voltage of the monostable oscillator is equal to the bias voltage in an equilibrium state, and

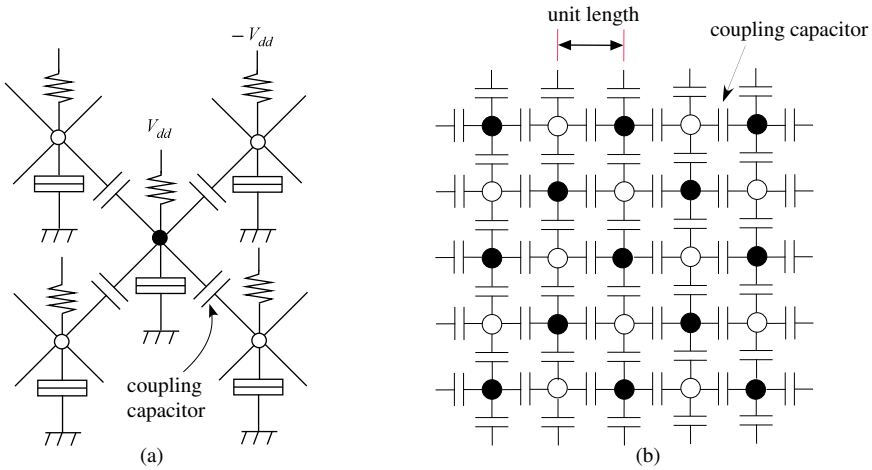

Figure 6.3: Photon-position sensor consisting of two-dimensional network of single-electron oscillators: (a) capacitive coupling of positively biased and negatively biased oscillators and (b) sensor device consisting of coupled-oscillator network. Closed circles and open circles represent the node of positively biased and negatively biased oscillators.

no change occurs under that condition. Upon application of a triggering signal, such as an incidence of photons, the Coulomb blockade is broken off, and electron tunneling occurs through the tunneling junctio n. The node voltage of a positively biased oscillator drops by e/C_j, as shown in Fig. 9.8(b), because of tunneling from the ground to the node. The node voltage then gradually increases to return to V_{dd} as junction capacitance C_j is charged through resistance R. In a negatively biased oscillator, the node voltage jumps by e/C_j because of tunneling from the node to the ground, and then gradually decreases to return to $-V_{dd}$. The structure of the proposed sensor consisting of monostable oscillators is shown in Fig. 9.10. It consists of a network of monostable single-electron oscillators—positively biased and negatively biased oscillators—regularly arrayed on a plane in a checkered pattern. Each positively biased oscillator is connected to four negatively biased oscillators by means of coupling capacitors. Similarly, each negatively biased oscillator is connected to four positively biased oscillators. The unit length of the network, or the arrangement pitch of oscillators, could be tens of nanometers for tunneling junction arrays that are made using existing nanoprocess technologies. The network, or the sensor device, is in a stable uniform state as it stands. Once tunneling is induced in an oscillator by an incident photon, the occurrence of tunneling events is transmitted from the oscillator to other oscillators in the following manner (see [9] for details). For

example, if electron tunneling occurs in a positively biased oscillator, the oscillator changes its node voltage from positive to negative, and this induces, through the coupling capacitors, electron tunneling in neighboring negatively biased oscillators. The negatively biased oscillators consequently change their node voltages from negative to positive, and this induces electron tunneling in neighboring positively biased oscillators. In this manner, the occurrence of tunneling events is transmitted in the network like a wave—hereafter, this consecutive transfer of tunneling events (wave) is referred to as a *tunneling wave*. To show this operation simply, the transmission of a tunneling wave is illustrated with simulated results for a one-dimensional connection of oscillators given in Fig. 9.12(a). Electron tunneling was induced in the leftmost oscillator A0 by a triggering signal, and the chain reaction of tunneling started and proceeded to the right along the row of oscillators. The successive drops in the node voltages, shown in Figs. 9.12(b) and (c), indicate this chain reaction, which occurred in the following manner. When tunneling occurred in the positively biased oscillator A2, its node voltage changed from positive to negative (see Fig. 9.12(b)). This induced tunneling in the neighboring negatively biased oscillator A3. The node voltage of A3 therefore changed from negative to positive, and this induced tunneling in positively biased oscillator A4. This way, a tunneling wave could propagate rightward through the oscillators.

A time lag or a waiting time exists between when the voltage across each junction exceeds the tunneling threshold and when tunneling actually occurs in the junction. This is caused by the stochastic nature of tunneling and determines the velocity of wave propagation. The waiting time has probabilistic fluctuations in every tunneling event (e.g., see the difference between t_1, t_2, and t_3 in Fig. 9.12(b)), and consequently, the wave velocity fluctuates at every moment around its mean value. The effect of this fluctuation, however, diminishes as the number of oscillators increases (see section 6.6).

6.3 Propagation of tunneling waves

In the two-dimensional network (Fig. 9.10(b)), the tunneling wave propagates in all direction and spreads across the network to form a circular wave. We simulated the wave propagation in a network consisting of 501 $\times$ 501 positively biased oscillators interleaved with a 500 $\times$ 500 array of negatively biased oscillators in a checkerboard pattern. In the calculations, we assumed that each oscillator is connected to four neighboring oscillators inside the network, three oscillators on the four sides, and two oscillators at the four corners.

The result is shown in Fig. 9.13. To visualize the time development of a tunneling

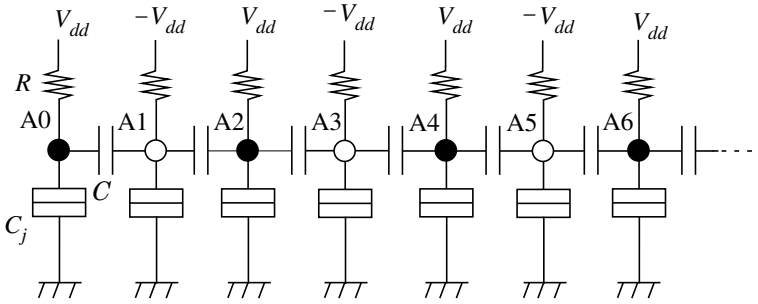

(a)

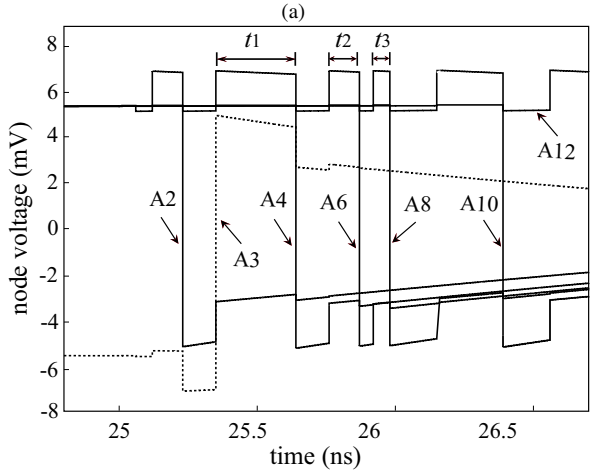

(b)

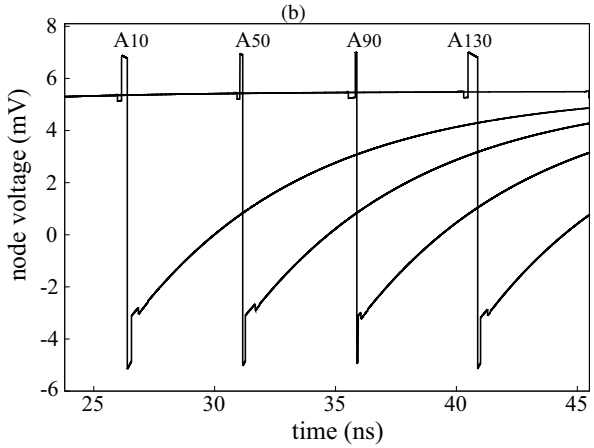

(c)

Figure 6.4: (a) One-dimensional connection of oscillators A0, A1, A2, ...; (b) Waveform of node voltage plotted for positively biased oscillators A2-A12 (solid lines) and negatively biased oscillator A3 (dashed line); (c) waveform for every fortieth oscillator. Tunneling is induced in leftmost oscillator A0 and transmitted rightward along the row of oscillators with delay. Drop in each waveform corresponds to tunneling in the oscillator. This was simulated with a set of parameters C_j = 10 aF, C = 2 aF, R = 400 MΩ, tunneling junction conductance = 1 μS, V_{dd} = 5.5 mV, $-V_{dd}$ = $-$5.5 mV, and zero temperature.

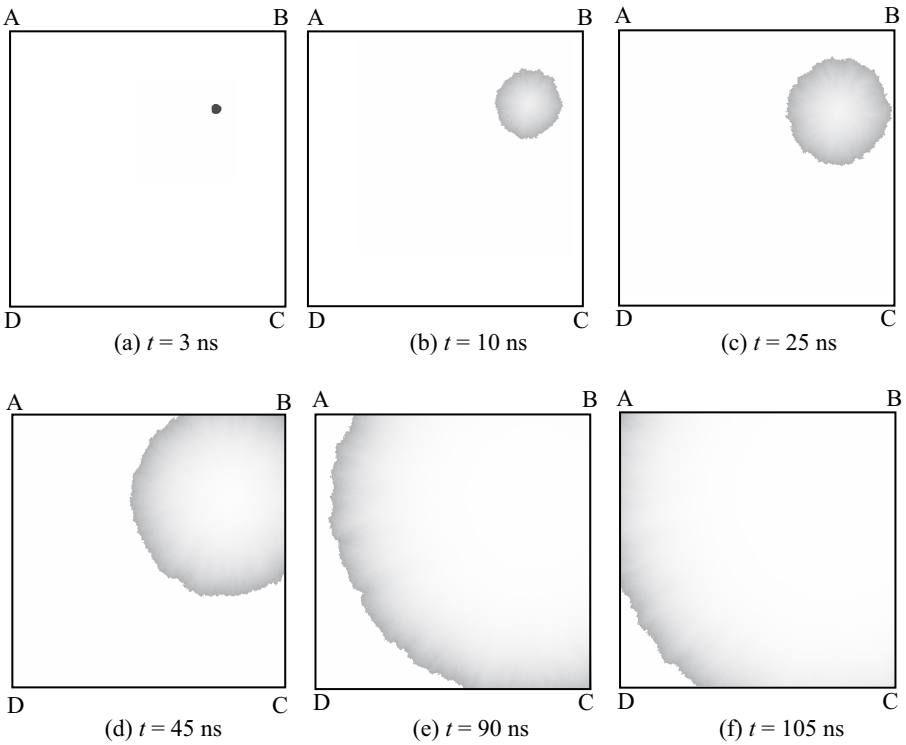

Figure 6.5: Expanding circular wave in the network. Snapshots for six time steps, with time t after the start of the wave, simulated with a set of parameters C_j = 10 aF, C = 2 aF, R = 400 MΩ, tunneling junction conductance = 1 μS, V_{dd} = 4.8 mV, $-V_{dd}$ = $-$4.8 mV, and zero temperature.

wave, the node voltage of each positively biased oscillator is shown on a gray scale: the light shading represents high voltage, and the dark represents low voltage. In this example, a tunneling wave started at the upper right of the network (Fig. 9.13(a)), expanded in all directions in the form of a circular wave (Figs. 4(b) and (c)), and reached corners A, B, C, and D (Figs. 9.13(d)-(f)). The front of the wave is the region where tunneling just occurred, and therefore, the node voltages of oscillators are at the lowest negative value (represented by the darkest shading). The front line of the wave is uneven or irregular because the velocity of the traveling wave fluctuated in each direction throughout the process because of the stochastic waiting time of tunneling. The mean velocity depends on the circuit parameters and was 100 unit lengths per 12.52 ns (for 'unit length', see Fig. 9.10(b)) for the parameter set given in the figure caption.
On the arrival of the wave, the positively biased oscillator at each corner produced tunneling and changed its node voltage from positive to negative. Waveforms of the node voltages are plotted in Fig. 9.7—the results of the wave propagation shown in Fig. 9.13. The time when the voltage dropped indicates the time when the wave reached the corner of the network.
After the wave passed, the node voltage of each oscillator gradually increased to return to its initial value. This is represented by light shading behind the wave front. If a photon hits again, the same operation will be repeated.

6.4 Detecting the starting position of tunneling waves

From the wave's arrival time at the corners, we can know the starting position of the wave as follows (see Fig. 6.7). Let us assume that a photon hits the sensor network ABCD at a position P. Then a tunneling wave appears at P and spreads out through the sensor at a velocity of v_0. As time passes, the wave front expands in all directions, as indicated by F1-F4, and reaches the periphery of the sensor. We observe the arrival of the wave at corners A, B, C, and D and measure the wave's arrival time at each point. If the arrival time was t_0 at point A and t_0 + t_1 at point B, we can consider that position P is on the locus S1 of points where the difference in the distance to points A and B is $v_0 t_1$. That is, P is on hyperbola S1 with foci A and B. Similarly, position P is also on hyperbola S2 with foci B and C. Therefore, we can determine position P as the point of intersection of the two hyperbolas.
There are six possible sets of foci (AB, AC, AD, BC, BD, and CD), so we can draw six hyperbolas from the data of arrival time at the four corner points. All the hyperbolas intersect at one point if the wave velocity is constant, and therefore,

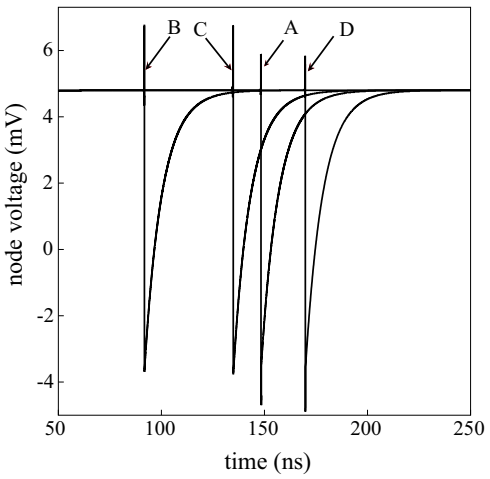

Figure 6.6: Node voltage waveforms of the oscillators at corners A, B, C, and D of network: the result of the wave propagation shown in Fig. 9.13. The trigger was applied at time = 50 ns

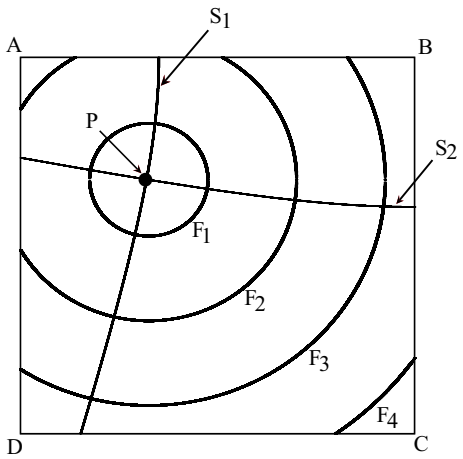

Figure 6.7: Determination of the position of incident photons. ABCD: sensor network. P: incident position of a photon, F1-F4: spreading wave front for four steps. S1 and S2: hyperbolas drawn from the arrival-time data at points A, B, and C.

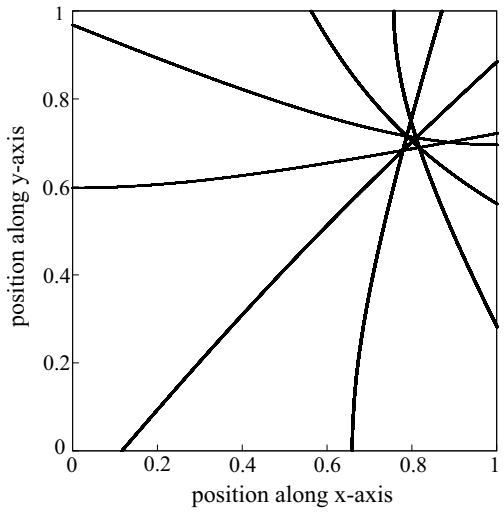

Figure 6.8: Calculation of the starting position of tunneling waves. The six hyperbolas with their 15 intersection points are shown. The mean coordinate of the intersection points was (0.799,0.701), which was approximately consistent with the actual starting position (0.8,0.7).

the two hyperbolas suffice to determine the position of P. In our device, however, wave velocity is not constant but fluctuates a little at every moment.
Consequently, not all the hyperbolas intersect at one point, and there can be 15 intersection points at maximum (i.e., combination ${}_6\mathrm{C}_2$ = 15). Therefore we determined the position of P by calculating the mean coordinate of the 15 intersection points.
Taking the example of Fig. 9.13, we calculated the starting position of the wave from the data of the wave's arrival time given by Fig. 9.7, and compared the calculations with the actual starting position. In the calculations, we set the coordinates of corners A, B, C, and D to (0,1), (1,1), (1,0), and (0,0). In this coordinate system, the starting position of the wave in Fig. 9.13 is (0.8,0.7). In the calculation results, six hyperbolas with their 15 intersection points are shown in Fig. 6.8. The mean coordinate of the intersection points was (0.799,0.701), which was approximately consistent with the actual starting position. This way, we can know the starting position of tunneling waves in the sensor, and therefore, can detect the position of incident photons.

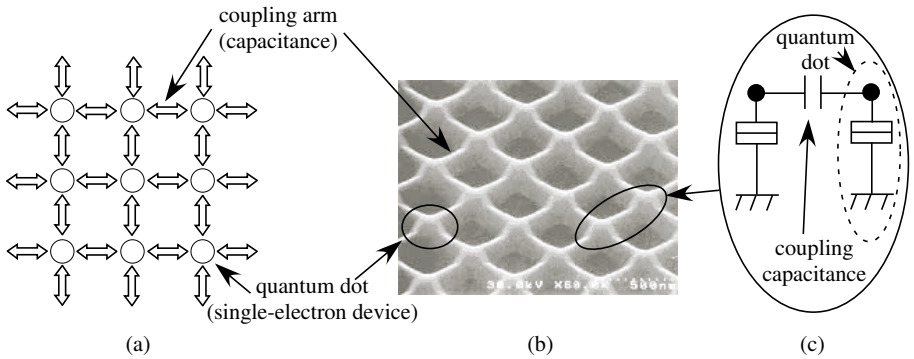

Figure 6.9: Structure of fabricated device. (a) Conceptual network of single-electron devices (b) Micrograph of a quantum-dot-network device fabricated at the Research Centre for Integrated Quantum Elecronics (RCQIE) at Hokkaido university. (c) Detailed structure of the fabricated device consisting of the quantum dot layer, and coupling capacitances.

6.5 Toward actual devices

To develop our idea into actual devices, we have to deal with two matters of importance; that is, constructing a large-scaled array of coupled single-electron oscillators, and amplifying a small output signal from a single-electron oscillator. The key to constructing the device is forming the arrangement of single-electron oscillators with their coupling arms and tunneling junctions at an arrangement pitch of tens of nanometers. One of us previously presented and demonstrated a process technology that can be used to fabricate such an array structure [10]. This technology uses self-organized crystal growth based on selective-area metalorganic vapor-phase epitaxy (see [32] for this epitaxy method). Using this technology, we can form an array of semiconductor dots with coupling arms and tunneling junctions in a self-organizing manner (Fig. 6.9(b)). The next step is to create high-resistance resistors on the nanodots. This could be achieved through two methods. One way is to use a multiple-tunneling junction, or a series of many tunneling junctions, (as described in [10]), using the same fabrication technology as the quantum dot array. Another possible method for realizing the resistance layer is by depositing a layer of high-resistive materials such as semi-insulating polycrystalline silicon (called SIPOS) [12] on the quantum dot layer.
Amplifying the output signal is the other matter of importance. The arrival of a tunneling wave produces a change in the node voltage of the single-electron oscillator on each corner. However, we would not be able to retrieve the output signal directly from the corner oscillator. This is so because a single junction has

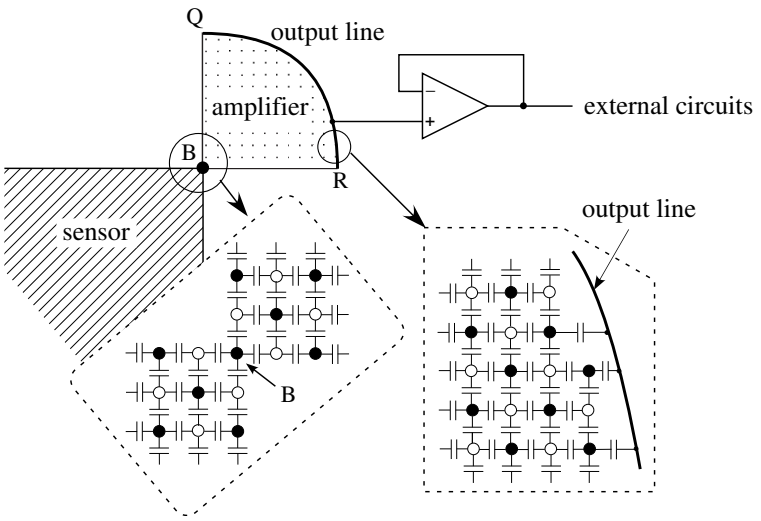

Figure 6.10: Output amplifier consisting of quadrant network of single-electron oscillators. Closed circles and open circles in the network represent the node of positively biased oscillators and negatively biased oscillators. The nodes of positively biased oscillators on arc QR are connected to an output load through coupling capacitors.

a very small capacitance and therefore cannot send a large enough voltage signal to an output load that has a far larger capacitance. Therefore, an output amplifier is indispensable for efficiently driving the output load. A promising method of amplifying the single-electron signal is by making use of an expansion of tunneling waves in the single-electron network. A schematic diagram of such an amplifier is shown in Fig. 6.10. The amplifier consists of a single-electron network with a quadrant periphery BQR that is connected to corner oscillator B of the sensor. The amplifier network has the same structure as that shown in Fig. 9.10(b), and the nodes of the positively biased oscillators on arc QR are connected to an output line through capacitors. A tunneling wave generated in the sensing network reaches corner oscillator B and induces tunneling in the oscillator. This excites a secondary wave in the amplifier. The secondary wave expands in the amplifier network and reaches arc QR to induce tunneling in all oscillators connected to the output line. The oscillators have a large capacitance in total and therefore can send a large signal to an output load.

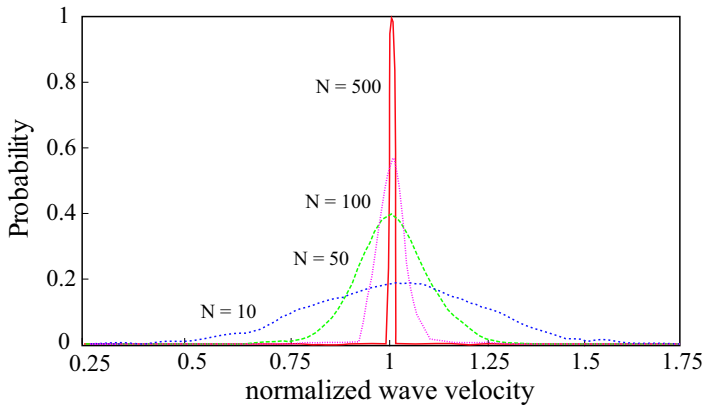

Figure 6.11: Fluctuation of wave velocity for N (the number of oscillators) = 10, 50, 100, and 500. Horizontal axis shows the wave velocity (reciprocal of normalised mean waiting time). As N increases, the fluctuation decreases and wave velocity approaches the average waiting time.

6.6 Effect of fluctuations in waiting time to the precision of position detection

The velocity of tunneling waves fluctuates around its mean value because of the stochastic nature of tunneling. However, when a wave travels across many oscillators, the fluctuation would be averaged and therefore the velocity could be considered to be almost constant. To confirm this, we simulated wave propagation along one-dimensional oscillator chains with various number of oscillators. That is, we simulated transmission time T for a chain with N oscillators and calculated the wave velocity given by N/T. We repeated this simulation many times and calculated the probability of occurrence of wave velocity i.e. probability of the wave velocity taking a certain value.

The results are shown in Fig. 6.11 for $N = 10, 50, 100, \text{and} 500$. The fluctuation in wave velocity decreased as the number of oscillators increased. For example, the distribution had a 3σ error of 5% for $N = 100$ and of 1% for $N = 500$. Therefore, putting a dummy zone consisting of many oscillators around the sensor will reduce the fluctuation in wave velocity. The output amplifier, shown in Fig. 6.10, can be used as the dummy zone, so no additional dummy zone will be needed in practice.

6.7 Summary

This chapter proposed a photon position sensor with a high spatial resolving power. The sensor consists of monostable single-electron devices coupled with each other through capacitors. Through Monte-Carlo based computer simulations we confirmed that a tunneling wave can propagate through the network of oscillators toward the sensors positioned at the peripheries. From the arrival times at the peripheral sensors, we could accurately determine the starting position of the tunneling wave—hence the two-dimensional position where the incident photon hit the sensor. We are now developing the proposed sensor device with together with the amplifier, using the self-organized crystal growth process technology.

References

[1] Wiza, J.L., ”Microchannel Plate Detectors,” Nucl. In- str. and Meth. vol. 162, pp. 587-601, 1979.

[2] Oba, K., and Matsuura, S., ”Characteristics of the newly developed MCP and its assembly”. IEEE Ttrans. vol. 32, pp. 350-354, 1985.

[3] Roy S. Bondurant, Prem Kumar, Jeffrey H. Shapiro, and Michael M. Salour ”Photon-counting statistics of pulsed light sources” Optics Letters, Vol. 7, Iss. 11, pp. 529?531, 1982.

[4] Fujiwara, A., Takahashi, Y. and Murase, K., ”Observation of single electron-hole recombination and photon-pumped current in an asymmetric Si single-electron transistor,” P. R. L. 78, pp. 1532-35, 1997.

[5] Nuryadi, R., Ishikawa, Y., and Tabe, M., ”Single-photon-induced random telegraph signal in a two-dimensional multiple-tunnel-junction array,” Phys. Rev. B 73 pp. 45310-16, 2006.

[6] Andrew J. Shields, Martin P. O’Sullivan, Ian Farrer, David A. Ritchie, Mark L. Leadbeater, Nalin K. Patel, Richard A. Hogg, Carl E. Norman, Neil J. Curson and Michael Pepper ”Single Photon Detection with a Quantum Dot Transistor,” Jpn. J. Appl. Phys. 40, pp. 2058-2064, 2001.

[7] Likharev, K. K. , ”Single-electron devices and their applications,” Proc. of IEEE 87, 4, pp. 606-32, 1999.

[8] Gravert, H., and Devoret, M. H., *Single Charge Tunneling—Coulomb Blockade Phenomena in Nanostructures* New York: Plenum, 1992.

[9] Oya, T., Asai, T., Fukui, T., and Amemiya, Y., ”Reaction-diffusion systems consisting of single-electron circuits,” Int. J. of Unconventional Computing 1 pp. 177-94, 2005.

[10] Oya, T., Asai, T., Fukui, T., and Amemiya, Y., ”A majority-logic nanodevice using a balanced pair of single-electron boxes,” J. of Nanoscience and Nanotechnology 2, pp. 333-42, 2002.

[11] Kumakura, K., Motohisa, J., and Fukui, T., ”Formation and characterization of coupled quantum dots (CQDs) by selective area metalorganic vapor phase epitaxy,” J. Crystal Growth 170, pp. 700-4, 1997.

[12] Ong, P. H., Ang, S. S., Brown, W. D., Naseem, H. A., Ulrich, R, K., and Dressendorfer, P, V., ”Arsenic-implanted thin film PECVD semi-insulating polysilicon (SIPOS) resistors,” J. Ele. Mat. 20, pp. 211-5, 1990.

【Part III 】

Neuromorphic LSI architectures employing non-linear properties of single-electron networks

In the third part of this thesis, a number of bio-inspired LSI architectures are discussed. The circuit architectures are inspired by information processing mechanisms in living organisms. As mentioned in the introduction part of this thesis, *emerging research* devices suffer from:

- Diverse variations in fabricated device feature sizes, resulting in heterogeneity in parameters and device characteristics ([1] - [4])
- High sensitivity to internal and external (or environmental) noises associated with nano scale properties.

Therefore, despite all the appealing features in utilizing nano-electronic devices in future electronic systems, we have to address and solve a fundamental question; how can we build reliable systems using error-prone and unreliable building devices? To address this problem, we consider obtaining hints from information processing in biological systems. The elementary building blocks of these systems — the neurons, are sensitive to noises, operate asynchronously because of differences in their structural properties, and have large time jitters—that is, they are imperfect and unreliable ([6] - [9])—-but nevertheless they carry out information processing effectively. Therefore, LSIs created by obtaining hints from biological systems (*Neuromorphic* LSIs [10], [11]) are seen as innovative ways of finding solution to the above mentioned problems facing nano-electronic devices.
To investigate how we mimic signal processing mechanisms in living systems in actual LSIs, we first studied how to implement some biological models with single-electron devices. Based on a well studied retinal edge detection model and a neuronal motion detection model we proposed simple circuit architectures that utilize non-linear properties of single-electron devices. To implement the two circuits with actual devices, we have to solve the problems mentioned above (low tolerance to noises, and high parameter fluctuations as a result of device fabrication mismatches). To do so, we employed a bio-inspired approach, where instead of getting rid of such noises, we subtly employed them in signal-processing. From the results, we could conclude that indeed utilizing noises in signal processing could improve signal-to-noise ratios, or fidelity of signal transmission in both circuits.
Part 3 of this thesis is divided into three chapters. Chapters 7 and 8, discuss single-electron circuits that are based on well studied biological models. We investigate ways of implementing such highly parallel information processing functions with single-electron devices. These include visual motion detection circuit based on correlation neural model, and edge detection and extraction circuit based on vertebrate retinal model.

In chapter 9, we explore the possibility of creating novel circuit architectures with single-electron devices, by employing environmental (dynamic) noises, and static noises originating from fabrication mismatches. The circuit architectures proposed in this chapter are inspired by information coding mechanisms in biological neural networks that convert analog input signals into spike densities (digital-pulse streams) in the time domain—pulse density modulation (PDM). This operation is also referred to 1-bit analog-to-digital conversion, and is often implemented with $\Delta - \Sigma$ modulators ([18], [19]). Such converters exhibit noise-shaping properties (see [6] - [22]) for details on neuronal noise-shaping), separating signal and noises into low and high frequency bands respectively. Secondly, we investigate the implication of noises in improving the fidelity with which a PDM circuit can encode high frequency signals (Chap. 9).

References

[1] Bowman, K., Duvall, S., & Meindl, J. (2002). Impact of die-to-die and within die parameter fluctuations on the maximum clock frequency distribution for gigascale integration. *J. of Solid-State Circuits*, 37, 183–190.

[2] Constantinescu, C. Trends and challenges in VLSI circuit reliability. *Micro, IEEE*, 23, 14 – 19, 2003.

[3] Jose A. B. F. Future Challenges in VLSI Design. *IEEE Computer Society Annual Symposium on VLSI (ISVLSI'03)*, 5–7, 2003.

[4] Way, K., & Taeho, K. An overview of manufacturing yield and reliability modeling forsemiconductor products. *Proc. of the IEEE*, 87, 1329–1344, 1999.

[5] Calhoun, B.H., Cao, Y., Xi L., Mai, K., Pileggi, L.T., Rutenbar, R.A., & Shepard, K.L. Digital Circuit Design Challenges and Opportunities in the Era of Nanoscale CMOS. *Proceedings of the IEEE.* 96, 343–365, 2008.

[6] Chatterjee, A. Concurrent Error Detection and Fault-Tolerance in Linear Analog Circuits Using Continuous Checksums. *IEEE Transactions on very large scale Integration (VLSI) Systems*, 1, 138–150, 1993.

[7] Shadlen, M.N., & Newsome, W.T. The Variable Discharge of Cortical Neurons: Implications for Connectivity, Computation, and Information Coding. *J. of Neuroscience*, 18, 3870–3896, 1998.

[8] Shint, J.N., Lee, K.R., & Park, S.B. Novel neural circuits based on stochastic pulse coding and noise feedback pulse coding. *Int. J. of Electronics*, 74, 359–368, 1993.

[9] Softky, W.R., & Koch, C. The highly irregular firing of cortical cells is inconsistent with temporal integration of random EPSPs. *J. of Neuroscience*, 14, 334–350, 1993.

[10] Douglas, R., Mahowald, M., & Mead, C. Neuromorphic Analogue VLSI. *Annual Review of Neuroscience*, 18, 255–281, 1995.

[11] Mead, C., *Analog VLSI and neural systems*. New York: Addison Wesley, 1989.

[12] Utagawa, A., Asai, T., Hirose, T., & Amemiya, Y. An inhibitory neural-network circuit exhibiting noise shaping with subthreshold MOS neuron circuits. *IEICE Transactions on Fundamentals of Electronics, Communications and Computer*, E90-A, 2108–2115, 2007.

[13] Collins, J.J., Chow, C.C., & Imhoff, T.T. Stochastic resonance without tuning. *Nature*, 376, 236–238, 2002.

[14] Simonotto, E., Riani, M., Seife, C., Roberts, M., Twitty J., & Moss, F. (1997). Visual Perception of Stochastic Resonance. *Phy. rev. lett.*, 78, 6, 1186–1189.

[15] Oya, T., Asai, T., & Amemiya, Y. Stochastic resonance in an ensemble of single-electron neuromorphic devices and its application to competitive neural networks. *Chaos, Solitons & Fractals*, 32, 855–861, 2007.

[16] Oya, T., Asai, T., Kagaya, R., Hirose, T., & Amemiya, Y. Neuronal synchrony detection on single-electron neural network. *Chaos, Solitons & Fractals*, 27, 887–894, 2007.

[17] Aziz, P.M., Sorensen, H.V., Van der Spiegel, J. An overview of sigma-delta converters. *IEEE Signal Processing Magazine*, 13, 61–84, 1996.

[18] Aziz, P.M., Sorensen, H.V., Van der Spiegel, J. An overview of sigma-delta converters. *IEEE Signal Processing Magazine*, 13, 61–84, 1996.

[19] Schreier, R., & Temes, G.C. *Understanding Delta-Sigma Data Converters*. New Jersey: Wiley-IEEE Press, 2004.

[20] Mayr, C., & Schueffny, R. Applying Spiking Neural Nets to Noise Shaping. *IEICE - Transactions on Information and Systems*, E88-D, 1885–1892, 2005.

[21] Shin, J. Adaptation in spiking neurons based on the noise shaping neural coding hypothesis. *Neural networks*, 14, 907–919, 2001.

[22] Shin, J. Adaptive noise shaping neural spike encoding and decoding. *Neurocomputing*, 38-40, 369–381, 2001.

7

Visual motion detection circuits based on correlation neural networks

7.1 Introduction

This chapter discusses a *neuromorphic* circuit inspired by motion detection in insects. Motion detection is an essential task in first levels of visual information processing carried out in the retina. Living organisms, in particular insects, utilize motion detection to avoid collision and to navigate movements. Through hints from biological systems, we could create highly functional nano-electronic processors for special applications in parallel information processing. For the last two decades, electronic circuits based on how living organisms perform information processing—*neuromorphic engineering* ([1] - [16]) have been viewed as a breakthrough to creating highly parallel, real time information processors for the next generation of LSIs.
In the sections to follow, firstly, the model of motion detection in insects is illustrated, followed by a detailed explanation on LSI implementation of the model with single-electron devices. Finally, performance of the proposed circuit is evaluated through Monte-Carlo based computer simulations.

7.2 The Correlation Model

The proposed circuit is based on the correlation motion scheme[3], one of the earliest biological motion detection systems based on the optomotor response of insects. In this model, motion detection is computed by comparing signals from a photoreceptor to delayed signals from adjacent photoreceptors. This is illustrated in Fig. 7.1. The photoreceptors (P_i) transduce light inputs (a light spot moving in the direction $\mathrm{P}_1 \rightarrow \mathrm{P}_2$ above the photoreceptors) in to electrical signals. The transduced signals are sent to both the corresponding correlators, and the neighboring pixels through delayers as shown in Fig. 7.1. For example, let's consider pixel 2. Photoreceptor P_2 receives light inputs to produce electrical

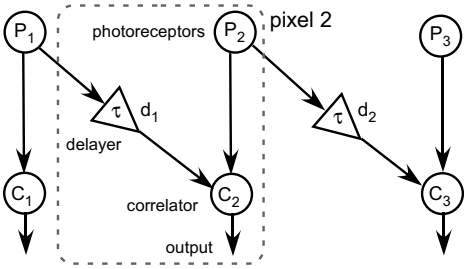

Figure 7.1: Correlator model for motion detection, consisting of photoreceptor cells (P), delayers (d) and correlators (C). Signals from photoreceptors are fed to the underlying correlators, and to the neighboring cell's corelators through the delayers.

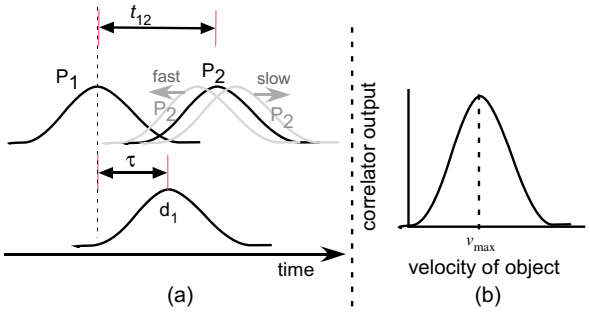

Figure 7.2: Operation of the correlator model: (a) transient response of photoreceptors P_1, P_2 and delayer d_1. (b) Output (velocity response curve) of correlator C_2.

signals corresponding to the light intensity. These signals are sent to the underlying correlator circuit C_2 and also to the adjacent correlator C_3 through delayer circuit d_2. Likewise, correlator C_2 receives a delayed signal from adjacent photoreceptor P_1 through d_1. Correlator C_2 gives an output, the product of these two signals (P_2 and d_1). In other words, C_2 calculates the correlation value between P_2 and d_1 signals. As illustrated in Fig. 7.2(a), if the two signals overlap, i.e., if the time the light spot takes to move from P1 to P2 ($\equiv t_{12}$) is equivalent to the delay time (τ), the correlator (C_2) gives the maximum output. This would be referred to as the maximum detectable velocity (v_{max}). Otherwise, if the velocity is lower (or higher) than the maximum velocity, the correlator gives a monotonously increasing (or decreasing) output (Fig. **??**(b)).

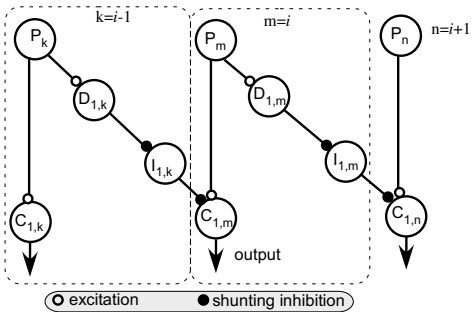

Figure 7.3: Conceptual circuit configuration with single-electron devices. The photoreceptors ($\mathrm{P}_{i's}$) receive light inputs to produce excitatory signals toward the delayer ($\mathrm{D}_{1,i's}$) circuits. The delayer circuits in turn produce inhibitory signals toward interneurons ($\mathrm{I}_{1,i's}$) which consequently send inhibitory signals toward correlator circuits ($\mathrm{C}_{1,i's}$).

7.3 Circuit implementation

To implement the motion detection model, we employ local computations among single-electron oscillators. This section starts with a description of the conceptual circuit structure for implementing the motion detection model with single electron devices. Then the basic function of single-electron devices and details on implementation of the respective parts of the motion-detection model; the photoreceptor, delayer, and the correlator circuits are illustrated. Finally a unit pixel of the proposed motion detecting circuit is shown.

The conceptual schematic model circuit is shown in Fig. 7.3. It constitutes of photoreceptors $\mathrm{P}_{i's}$, delayer circuits $\mathrm{D}_{1,i's}$, interneuron circuits $\mathrm{I}_{1,i's}$, and correlator circuits $\mathrm{C}_{1,i's}$. Photoreceptor P_m receives light inputs to produce an excitatory signal toward correlator $\mathrm{C}_{1,m}$. Similarly, photoreceptor P_k receives light inputs to produce excitatory signals toward the delayer circuit $\mathrm{D}_{1,k}$. The delayer circuit in turn produces an inhibitory signal toward interneuron $\mathrm{I}_{1,k}$, which consequently produces an inhibitory signal toward the correlator $\mathrm{C}_{1,m}$. The correlator calculates the correlation value of the two signals from neighboring photoreceptors; it gives a zero output at the maximum value of inhibitory signal $\mathrm{I}_{1,k}$, or otherwise produces an increasing output as the magnitude of the inhibitory signal decreases.

Based on this basic configuration, the following subsections give details on how to realize the motion detecting circuit.

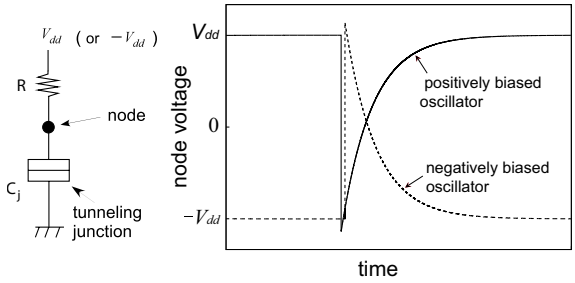

(a) (b)

Figure 7.4: Single electron oscillator; (a) circuit configuration (b) monostable, or one-shot, operation of positively biased (solid curve) and negatively biased (dashed curve) oscillators.

7.3.1 Single-electron oscillator

To realize the proposed motion detecting circuit, we employ single-electron oscillators. A single-electron oscillator, shown in Fig. 7.4(a), is a simple circuit consisting of a tunneling junction C_j and a high resistance R connected in series at a node (•) and biased with a positive voltage V_{dd} (Fig. 7.4(a)) or a negative voltage $-V_{dd}$. It operates as a relaxation oscillator at low temperatures at which the Coulomb-blockade effect takes place. The oscillator is astable if the bias voltage is lower than the tunneling threshold ($V_{dd} > e/(2C_j)$ (e is the elementary charge)) and monostable if $V_{dd} < e/(2C_j)$ (see [17] - [19]). The node voltage of the monostable oscillator is equal to the bias voltage in an equilibrium state, and no change occurs under in the absence of external innterference. Upon application of an external trigger signal, such as incidence of photons, the Coulomb blockade is broken off, and electron tunneling occurs through the tunneling junction. The node voltage of a positively biased oscillator drops by e/C_j, because of tunneling from the ground to the node, then gradually increases to return to V_{dd} as junction capacitance C_j is charged through resistance R (Fig. 7.4(b)-solid curve). In a negatively biased oscillator, the node voltage jumps by e/C_j because of tunneling from the node to the ground, and then gradually decreases to return to $-V_{dd}$ (Fig. 7.4(b)-dashed curve). To implement the motion detecting circuit, we utilize monostable single-electron oscillators.

7.3.2 Photoreceptor circuit

The retinal photoreceptor is implemented with a negatively biased single-electron oscillator. As explained in the previous subsection, in the absence of external

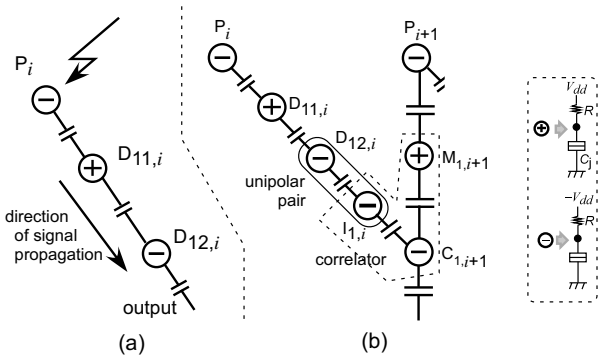

Figure 7.5: (a) Delayer circuit: Signal propagation through oscillators in the delayer circuit. Photoreceptor (P_i) receives light inputs to produce an electrical signal, which is fed to underlying oscillator $\mathrm{D}_{11,i}$ through a coupling capacitor. The signal is similarly relayed to oscillator $\mathrm{D}_{12,i}$, (b) Signal propagation through delayer and correlator circuits.

interference, the photoreceptors assume a stable state where their node (nanodot) voltages take a value equivalent to the bias voltage. In the presence of light inputs (incoming photons), *photo-induced tunneling effect* ([9] - [10]) takes place inducing electron tunneling from the nanodot to the ground. This leads to a jump in the node voltage from a low to a high value. We refer to this change as a firing event. The nanodot is recharged to its original stable state. The number of firing events would be proportional to the intensity of the illuminated light; low intensities would produce low firing rates and vice versa.

7.3.3 Delayer and Correlator circuits

The delayer circuit is realised through capacitively coupled single-electron oscillators, which form a delay transmission line [23]. This is illustrated in Fig. 7.5(a). Let's assume that photo-induced tunneling occurs at photoreceptor P_i. This triggers a signal flow toward underlying oscillators $\mathrm{D}_{11,i}$ and $\mathrm{D}_{12,i}$ as follows. Electron tunneling in P_i leads to a voltage increase in $\mathrm{D}_{11,i}$ above its threshold, thus inducing it to tunnel. Likewise tuneling in $\mathrm{D}_{11,i}$ reduces the node voltage of $\mathrm{D}_{12,i}$ below the threshold value inducing it to tunnel [22] - [23]. Therefore signals emanating from the photoreceptors propagate through the series of positively and negatively biased oscillators (transmission line), with a time delay at each stage caused by stochastic nature of electron tunneling [17].
The basic circuit configuration of the conceptual circuit (Fig. 7.3) implemented with single-electron devices is shown in Fig. 7.5(b). Suppose a light spot is

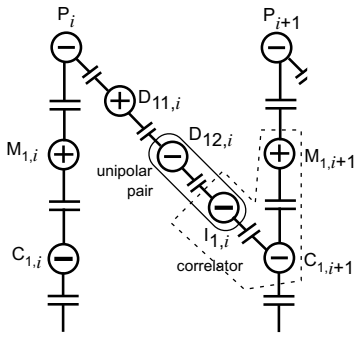

Figure 7.6: Unit pixel configuration of the motion detecting circuit for left → right images.

moving from from the left to the right. This triggers the photoreceptors to tunnel in turns, $\mathrm{P}_i \rightarrow \mathrm{P}_{i+1} \rightarrow \cdots$. The signals emanating from the photoreceptors are transmitted through the delayers as explained above. To implement the inhibition function between the delayer and correlator circuits, we introduce a unipolar pair in the trasmission line of positively- and negatively-biased oscillators. This is realised by introducing a capacitively coupled pair of negatively-biased oscillators between the delayer and the correlator circuit (see unipolar pair encircled with a solid line in Fig. 7.5(b)). Therefore signals flowing from the delayer circuit raise the node voltages of the unipolar pair, and consequently the correlator terminal circuit ($\mathrm{C}_{1,i+1}$), thus inhibiting them from tunneling, even in the presence of an external trigger input. On the other hand, tunneling in P_{i+1} induces tunneling in $\mathrm{M}_{1,i+1}$, which in turn induces $\mathrm{C}_{1,i+1}$ to tunnel. The correlator circuit, $\mathrm{C}_{1,i+1}$, receives excitatory signals from $\mathrm{M}_{1,i+1}$ and inhibitory signals from $\mathrm{I}_{1,i}$ (with which it makes a unipolar pair). Thus the tunneling rate of $\mathrm{C}_{1,i+1}$ remains at a low value (almost zero) as inhibitory signals are fed from the delayer circuit ($\mathrm{D}_{13,i}$), and increases as the inhibition signal decreases with time.

7.3.4 Unit pixel circuit

A unit pixel of the motion detecting circuit is shown in Fig. 7.6. This configuration can only detect motion in images (light spots) travelling from the left toward the right. A circuit configuration for detecting bi-directional motion is illustrated in Fig. 7.7(a). The subscript ”1” (for open circles) denotes circuits responsible for left-right motion detection, while ”2” (for shaded circles) shows circuits responsible for right-left motion detection. The correlation value in both directions is produced at the coresponding correlators $\mathrm{C}_{1,n}$ and $\mathrm{C}_{2,n}$ (for the i_{th}

pixel) for left-right and right-left motions respectively. These signals are fed to the underlying layer (see dotted box in Fig. 7.7(a)) where the final correlation value, and hence motion velocity is determined. The circuit configuration of a unit pixel of the dotted region is shown in Fig. 7.7(b). Let's assume the light spot is moving from the left to the right. The correlator circuit ($C_{1,i}$) would produce a signal corresponding to the velocity of the light spot as explained above. Note that as the light spot moves to the right, the magnitude of the inhibition signal toward the "left" direction correlator circuit remains high, as opposed to decreasing inhibition signal sent to the "right" direction correlator circuit, as explained in Section 7.3.3. Therefore, for images travelling fom the left to the right, the correlator circuit $C_{2,i's}$ would produce a zero output in comparison to correlator $C_{1,i}$. The signals from correlator $C_{1,i}$ are fed to C_i through the right branch via oscillator $O_{1,i}$. At the same time, $C_{1,i}$ sends inhibitory signals to the left branch (toward $O_{2,i}$), blocking any signals from the $C_{2,i}$ oscillator. The same is repeated in a leftward motion detection. Therefore, this mechanism makes it possible to detect motion in both directions and to produce an output value of zero at C_i for stationary images.

7.4 Simulation results

The operation of the proposed motion detection circuit was investigated with a one-dimensional array construction consisting of 100 unit pixels. A unit pixel is shown in Fig. 7.7 (unit pixel). Light inputs were simulated with an external trigger input whose frequency is equivalent to the intensity of the input light. The trigger input was set to an amplitude of 2.5 mV and the light intensity was simulated with a maximum frequency of 50 MHz. All excitatory and inhibitory capacitive couplings were implemented with a capacitance (C) of 2 aF, whereas tunneling junction capacitance C_j was set to 10 aF.

7.4.1 Velocity response curve

With the above construction, we investigated the response of the proposed motion detector to images (light spots) travelling at different velocities, to obtain the velocity response curve. The velocity response curve (VRC) was obtained by plotting the maximum firing rate of correlator circuits against the velocity of projected images. Fig. 7.8 shows the VRC of the $50th$ correlator circuit as a function of the projected image velocity moving from the left toward the right at zero temperature. The proposed circuit can detect motion in projected images with a maximum detectable velocity of 20 pixels/ns. This would correspond to a

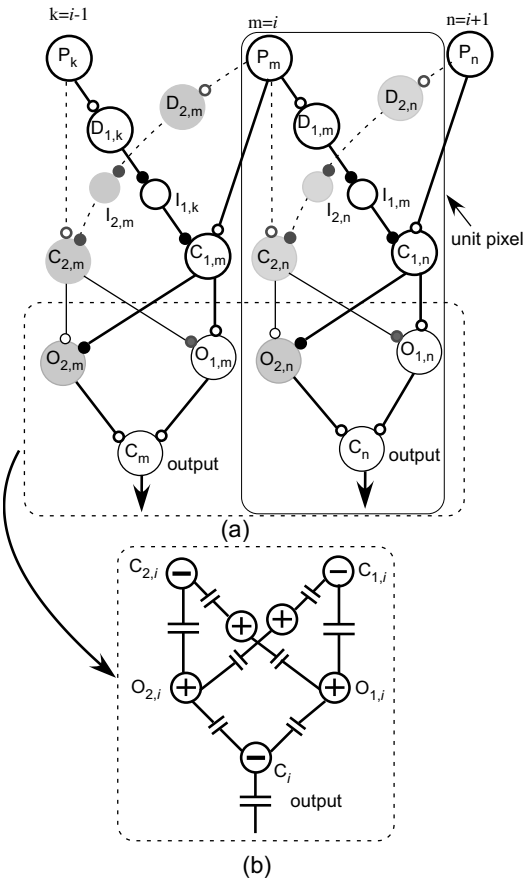

Figure 7.7: (a) Conceptual circuit configuration for bi-directional motion detection. Open circles denoted with subscript $(1,i)$ represent circuits responsible for left $\rightarrow$ right motion detection, while shaded circles denoted with subscript $(2,i)$ represent delayer, interneural and correlator circuits responsible for motion detection in images moving from the right toward the left. (b) Circuit configuration of the overall correlation circuit (dotted portion in (a)) of the bi-directional motion detector.

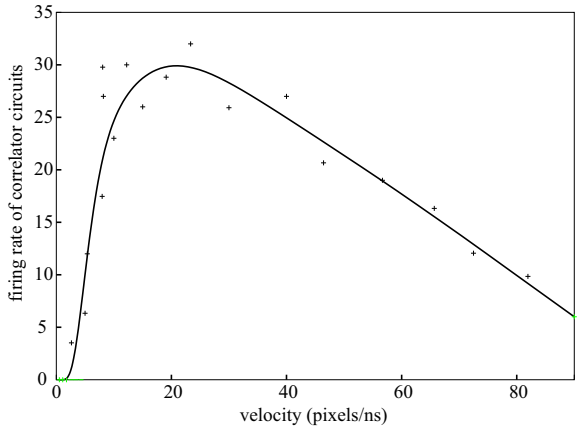

Figure 7.8: Motion detection with a 100 pixel array construction. Vertical axis shows the maximum firing rate of the $50th$ correlator circuit against the projected image velocity. Simulated with images moving from the left to the right at zero temperature. Maximum frequency of input trigger is set to 50 MHz.

maximum velocity of 2 Km/s if adjacent photoreceptors were fabricated at a pitch of 100 nm. The maximum detectable velocity can be tuned by adjusting the delay-time τ along the transmission line. This can be achieved by increasing (or decreasing) the number of oscillators along the transmission line to increase (or decrease) the maximum detectable velocity.

7.4.2 Response to light intensity

As mentioned in subsection 7.3.2, the firing rate of the photoreceptor circuits is proportional to the light intensity. To confirm the response of the proposed circuit to light intensity, images with different light intensities (and constant velocity) were projected onto the 100-pixel retinomorphic circuit. Fig. 7.9 shows the response of the 50*th* correlator circuit to various light intensities, for images travelling at a constant velocity of 20 pixels/ns. The vertical axis shows the maximum output of the 50*th* correlator circuit at zero temperature. The firing rate of the correlator circuit (output) increases with increase in light intensity to attain a maximum value at a light intensity of 75 MHz. The vertical axis is normalised with the firing rate at 75 MHz.

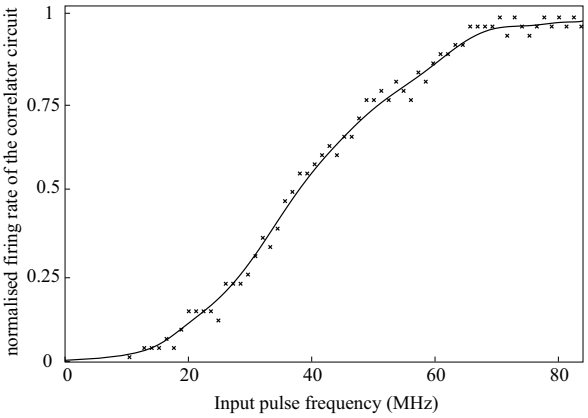

Figure 7.9: Response to light intensity simulated by varying the maximum frequency of input tigger signal. Vertical axis represents the maximum firing rate of the 50*th* correlator circuit, normalised with the maximum firing rate at 75 MHz. Simulated at zero temperature.

7.4.3 Temperature characteristics

We evaluated the temperature performance of the motion detecting circuit with increasing temperatures by plotting the *hump* (see Fig. 7.10(a)) height against the temperature. The *hump* height is the difference between the firing rate at zero velocity and at the maximum detectable velocity. We refer to this as the signal-noise (SN) ratio. We observed that as the temperature increases, random firing as a result of thermal induced electron tunneling within the circuit also increases (Fig. 7.10(a), (b), and (c) simulated at T = 5, 10, and 20 K respectively). As a result the height of the hump (SN ratio) decreases, and finally flattens at high temperatures. Fig. 7.11 shows the simulated results for a temperature range between 0 and 30 K. The vertical axis, *hump* height is normalized with the maximum height at zero temperature. With the present configuration, the proposed circuit can perform at signal-noise ratio of 0.4 at 20 K.

7.5 Summary

In the first chapter in this part, we proposed a motion detection circuit based on correlation neural models in insects. Based on this model, we proposed a circuit structure with single-electron devices and evaluated its performance through Monte-carlo based simulations. The proposed circuit could detect motion in images with a maximum detectable velocity of 20 pixels/ns. The temperature

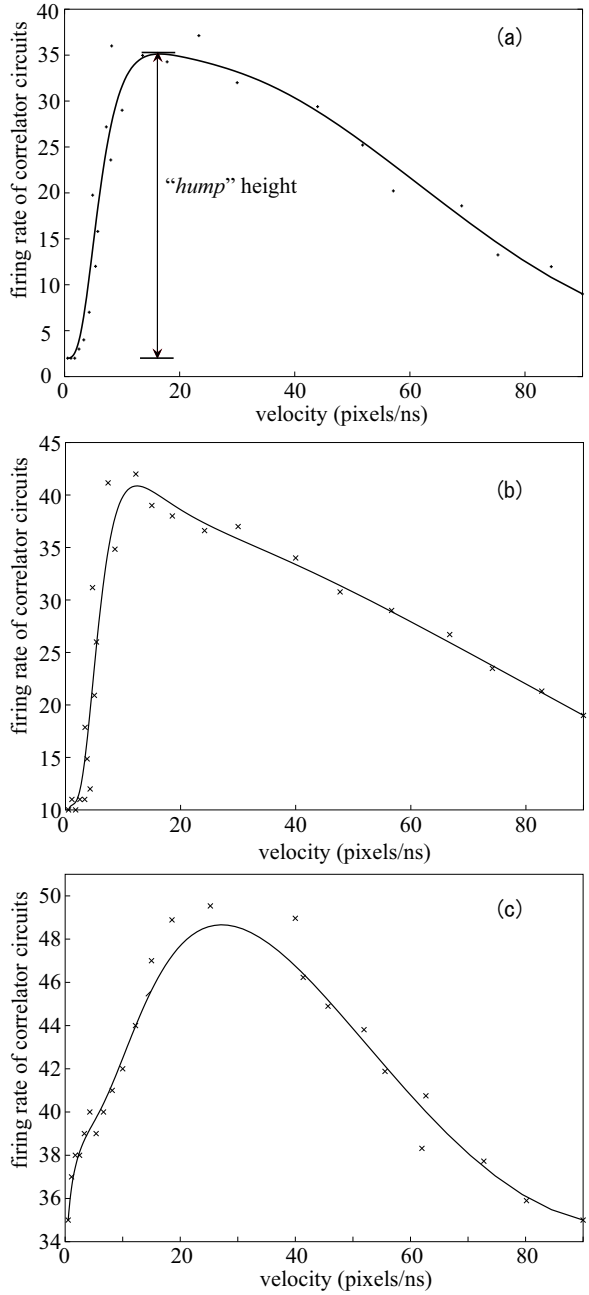

Figure 7.10: Velocity response curves simulated for temperature T = 5 K (a), 10 K (b), and 20 K (c). Vertical axis shows the maximum firing rate of the $50th$ correlator circuit against the projected image velocity.

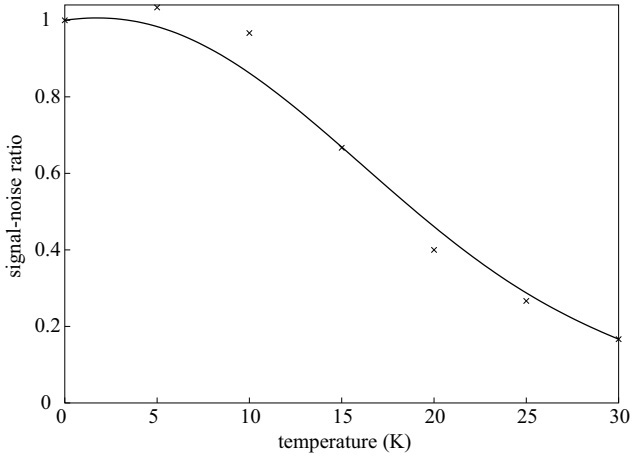

Figure 7.11: Temperature characterists: *hump* height (signal-noise ratio) plotted against temperature. Vertical axis is normalised with the SN ratio at zero temperature.

characteristics of the proposed circuit were analyzed. The circuit could detect motion in images with a signal-noise ratio of 0.4 at 20 K.

References

[1] Carver Mead, Analog VLSI and Neural Systems, Addison-Wesley,1989.

[2] Douglas, R., Mahowald, M., and Mead, C., "Neuromorphic analogue VLSI," Annual Review of Neuroscience, 18, pp. 255-281, 1995.

[3] Reichard, W., "Autocorrrelation, a principal for the evaluation of sensory information by the central nervous systems, in: Sensory communication," Contributions to the Symposium on Principles of Sensory Communication, edited by W.A. Rosenblith, MIT Press, pp. 303-317, 1961.

[4] Egelhaaf, M., Borst, A., and Reichardt, W., "Computational structure of a biological motion-detection system as revealed by local detector analysis in the fly's nervous system," J. Opt. Soc. Am. A, 6, pp. 1070-1087, 1989.

[5] Barlow, H.B. and Levick, W.R., "The mechanism of directionally selective units in rabbit's retina," J. of Physiology, 178, 477- 504, 1965.

[6] Delbrück, T., "Silicon retina with correlation-based, velocity-tuned pixels," IEEE Trans. Neural Networks, 4, pp. 529-541,1993.

[7] Moini, A., Bouzerdoum, A., Eshraghian, K., Yakovleff, A., Xuan Thong Nguyen, Blanksby, A., Beare, R., Abbott, D., Bogner, R.E., "An insect vision-based motion detection chip," IEEE J. Solid State Circuits, 32, pp. 279-284, 1997.

[8] Asai, T., Ohtani, M., Yonezu, H., "Analog MOS circuits for motion detection based on correlation neural networks," Jpn. J. Appl. Phys., 38, pp. 2256-2261, 1999.

[9] Fujiwara, A., Takahashi, Y., and Murase, K., "Observation of single electron-hole recombination and photon-pumped current in an asymmetric Si single-electron transistor," Phys. Rev. Lett., 78, pp. 1532-1535, 1997.

[10] Nuryadi, R., Ishikawa, Y., and Tabe, M., "Single-photon-induced random telegraph signal in a two-dimensional multiple-tunnel-junction array," Phys. Rev. B, 73, pp. 45310- 45316, 2006.

[11] Gravert H., and Devoret, M.H., Single Charge Tunneling—Coulomb Blockade Phenomena in Nanostructures, New York: Plenum, 1992.

[12] Likharev K.K., and Zorin, A.B., "Theory of the Bloch-wave oscillations in small Josephson junctions," J. of Low Temp. Phys., 59, pp. 347-382, 1985.

[13] Averin, D. V., Likharev, K. K., ”Coulomb blockade of single-electron tunneling, and coherent oscillations in small tunnel junctions,” J. of Low Temp. Phys., 62, pp. 345-373, 1986.

[14] Oya, T., Asai, T., Fukui, ., and Amemiya, Y., ”Reaction-Diffusion Systems Consisting of Single-Electron Oscillators,” Int. J. Unconventional Computing, 1, pp. 177-194, 2005.

[15] Oya, T., Schmid, A., Asai, T., Leblebici, Y., and Amemiya, Y., ”On the fault tolerance of a clustered single-electron neural network for differential enhancement,” IEICE Electronics Express, 2, 76-80 2005.

8

A neuromorphic circuit for edge detection and extraction

8.1 Introduction

This chapter illustrates an edge detecting (or extracting) circuit inspired by image processing mechanisms in the vertebrate retina. Edge detection is a primary function in the early stages of visual processing carried out in the vertebrate retina. Thus far, only neuromorphic circuits achieved with silicon have been designed and fabricated [1] - [3]. In this work, we propose a possible image-processing structure for single-electron circuits as an example toward linking *nano-electronic devices* with *neuromorphic architectures*. Based on a well studied model of the vertebrate inner retina, this chapter illustrates a single-electron circuit that detects edges, and investigates its basic operations. The chapter starts by explaining the model. This is followed by details on how to implement the model with single-electron devices. Finally, details on the operation of the proposed circuit are illustrated with one- and two-dimensional circuit structures.

8.2 The model

The vertebrate retina consists of massively interconnected neural cells in a hierarchical structure, where edge detection is carried out mainly through three types of cells: (i) photoreceptors that transduce light inputs into electrical signals, (ii) horizontal cells that receive inputs from the superjacent layer of photoreceptors and produce spatially averaged outputs in relation to the inputs, and (iii) bipolar cells that produce the difference in amplitudes between the outputs of photoreceptors and horizontal cells. The schematic model is shown in Fig. 8.1(a) . In this model, we assume that illuminated (or non-illuminated) photoreceptors produce low (or high) potentials (Figs. 8.1(b) and (c)-P). The outputs are spatially averaged by horizontal cells (Fig. 8.1(c)-H). The bipolar

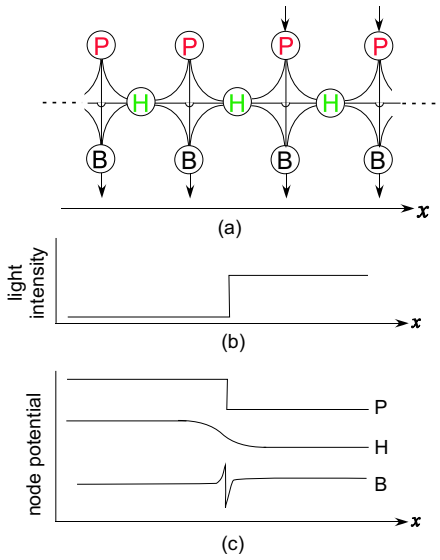

Figure 8.1: Cross section of the vertebrate retina, showing neurons involved in edge detection: (a) Model: P—Photoreceptors, H—Horizontal cells, and B—Bipolar cells. (b) Intensity profile of incident light and (c) Potentials of P, H, and B cells, showing response to the incident light (input)

cells detect the position of edges in the incident images by producing the difference in amplitudes between photoreceptors and horizontal cells. This is obtained by subtracting “H”- from their corresponding “P”-values in bipolar cells. Therefore, the non-zero outputs of bipolar cells represent the positions of edges in the input image (Fig. 8.1(c)-B).

8.3 Circuit implementation

In this section we propose a neuromorphic architecture, based on the retinal model above, with single-electron oscillators. Details on the operation of single-electron devices are presented in chap. 7. We start by giving details on how to realize the constitutive elements, i.e., photoreceptors, horizontal and bipolar cells with single electron devices, and then explain the configuration of a unit pixel circuit.

8.3.1 Photoreceptor circuit

Photoreceptors convert incident light inputs into electrical signals. We implement a retinal photoreceptor with a positively biased monostable oscillator that is

triggered by external light inputs. In the absence of external inteference (thermal or incoming photons) the node voltage of the oscillator is stable (and equivalent to the bias voltage). If a photon (light) is illuminated on the nano-dot, *photo-induced charging effect* ([20],[21]) occurs and an electron tunneling is induced from the ground to the nano-dot across the tunneling junction. Therefore the oscillator changes its node voltage from positive to negative. Since the intensity of input light is proportional to the number of incident photons, the number of tunneling and recharging events also increase. Therefore the intensity of incoming light would correspond to the average tunneling rate in the photoreceptors. To realize the photoreceptor layer, we use a single oscillator for a single photoreceptor cell.

8.3.2 Horizontal cell circuit

The horizontal cell layer receives inputs from the superjacent layer of photoreceptors to produce a spatially averaged output. The horizontal cells are implemented with negatively biased single-electron oscillators. Fig. 8.2 shows the configuration of the horizontal cell layer. The extensive gap junctions in the retinal cells are emulated by a resistive-coupling, realized through resistor $\mathrm{R_h}$, between neighboring horizontal oscillators. If tunneling takes place in one of the horizontal cell circuits, from the node to the ground, the node voltage of the corresponding oscillator changes from a low to a high value. Through this resistive coupling, the excess negative charge is redistributed to neigboring horizontal cells, reducing their node voltages. The change in the node voltage is inversely proportional to the spatial distance from the tunneling cell: oscillators nearest to the tunneling cell experience a higher drop in their node voltages, and therefore have a higher probability of tunneling than those positioned further. Thus, the average tunneling rate decreases with the spatial distance from the tunneling cell. Therefore, negatively biased oscillators coupled through resistances would produce a spatially weighted output in relation to the input from superjacent photoreceptor cells.

8.3.3 Bipolar cell circuit

Bipolar cells detect the position of edges by producing the difference in the amplitude of corresponding photoreceptors and horizontal cells. In conventional silicon retinas, this could be realized with an operational amplifier or current subtraction method. To implement a similar architecture with single-electron devices, we would require a complicated circuit. We therefore, qualitatively imitated the subtractive functions of the bipolar cells through neural shunting inhibition mechanism.

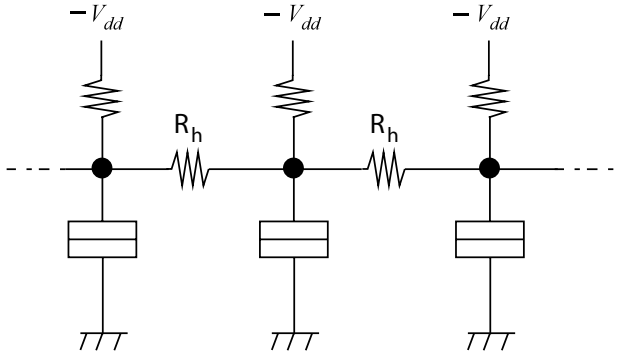

Figure 8.2: Configuration of the horizontal cell layer: A single horizontal cell is implemented with a negatively biased oscillator, while the junction gaps are emulated through resistive coupling realized with resistor $\mathrm{R_h}$

This mechanism is illustrated in Fig. 8.3. We consider a configuration in which the photoreceptors (P) produce an excitatory signal, while the horizontal cells ($\mathrm{H_l}$ and $\mathrm{H_r}$) produce an inhibitory signal toward "D" cells. If the excitatory signal surpasses the inhibitory signal in amplitude, it triggers cell "D" to tunnel (excitation). Otherwise, cell "D" would be restrained from tunneling (shunting inhibition).

These two mechanisms can be achieved with single-electron devices through capacitive couplings [22]-[24]. An excitatory coupling is achieved by connecting a positively (+) biased oscillator to one that is negatively (-) biased. In the absence of an external input, the oscillator node takes a voltage value equivalent to the bias voltage. If tunneling occurs in the positive oscillator, through the capacitive coupling, the negative charge leads to a drop in the node potential of the coupled negative oscillator below its threshold, thus inducing it to tunnel. Shunting inhibition is realized by applying the same bias voltage to two coupled oscillators. For example, if the two are positively biased, tunneling in either of them leads to a drop in the node voltage of the other far below the threshold, thus restraining it from tunneling (inhibition) even in the presence of an external trigger input.

Fig. 8.4 shows fundamental circuits for neural excitation and inhibition with single-electron oscillators. Let us assume that electron tunneling occurred in "P". This triggers a signal flow along the middle branch: electron tunneling in "P" leads to a drop in the node voltage of $\mathrm{B_1}$ below its threshold (thus inducing it to tunnel). $\mathrm{B_1}$ in turn induces tunneling in $\mathrm{B_3}$, and tunneling in "*O*" is consequently induced (excitation). On the other hand if tunneling takes place in cells $\mathrm{H_l}$ and $\mathrm{H_r}$, this triggers subsequent tunneling in the left and right branches. Tunneling in $\mathrm{B_{2l}}$ and $\mathrm{B_{2r}}$ decreases the node voltage of $\mathrm{B_3}$ restraining it from tunneling

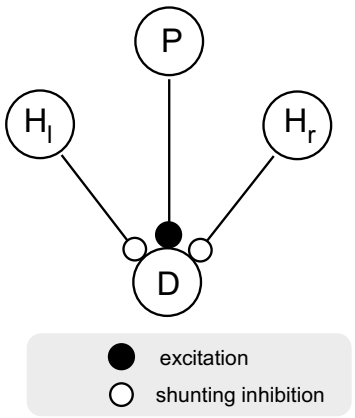

Figure 8.3: Conceptual configuration of bipolar cells: Neural excitation and inhibition

(shunting inhibition)–in other words, tunneling in ”H” cells blocks excitatory signals initiating from ”P” in the middle branch. If tunneling occurs in either of the ”H” cells, this would not have a sufficiently large inhibitory effect on B_3, and the probability of electron tunneling taking place (tunneling rate) would be higher than that in the previous case. With these excitatory and inhibitory configurations, we partly imitate the subtractive functions of bipolar cells.

8.3.4 Configuration of a unit pixel

The edge detecting circuit is constructed with ”P”, ”H”, and ”B” blocks, proposed in the preceding section. The configuration of a unit pixel is shown in Fig. 8.5. To increase the inhibitory effect of the horizontal cell layer, additional excitatory coupling was introduced between $\mathrm{B}_{1,2}$ and $\mathrm{B}_{2\mathrm{r}}$.

8.4 Simulation results

To confirm the basic operation, we constructed (i) a one-dimensional array retinal-circuit consisting of 100 pixel circuits, and (ii) a two-dimensional retinal-circuit consisting of 100×100 pixel circuits. We carried out Monte-Carlo based simulations: transient responses of the ”P”, ”H”, and ”B” cell circuits, edge responses, sensitivity to light intensity, Mach bands and evaluated signal to noise ratio (SNR) with temperature, to confirm their basic operations. In the simulations, the horizontal layer gap junction was simulated with a resistance $\mathrm{R}_\mathrm{h} = 400$ MΩ, excitatory and inhibitory capacitive coupling with a capacitance

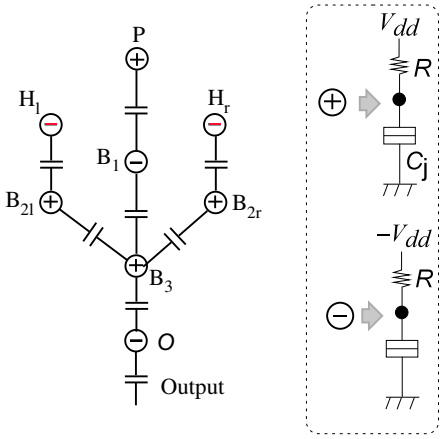

Figure 8.4: Realizing the bipolar circuit: Neural excitation and inhibition with single-electron circuits

of 2 aF, tunneling junction capacitance C_{j}, series resistance R, and tunneling junction conductance were set to 10 aF, 100 MΩ, and 1 μS respectively. The simulation time was 700 ns.

8.4.1 One-dimensional array circuit

The projected image is shown in Fig. 8.6. The dark region shows non-illuminated regions of the array, while the unshaded region (pixels 33-67) represents uniformly illuminated photoreceptors.
Light input was simulated by applying an external trigger input (whose frequency is equivalent to the intensity of the input light) to corresponding photoreceptors. In this simulation, the applied trigger frequency and amplitude were set to 110 MHz, and 2.5 mV respectively.

Transient responses

Fig. 8.7 shows the time-course responses of photoreceptors, horizontal and bipolar cell circuits. Fig. 8.7(a) shows the response of the 50*th* photoreceptor circuit. The photoreceptor receives a series of trigger signals, which induce it to tunnel from a high to a low voltage, followed by recharging to repeat the same cycle. We refer to each of these cycles as a firing event. The light intensity is computed by calculating the average firing rate of each photoreceptor circuit. Fig. 8.7(b) shows the response of the 50*th* cell of the subjacent horizontal cell layer. As mentioned in the previous section, due to the averaging effect of gap

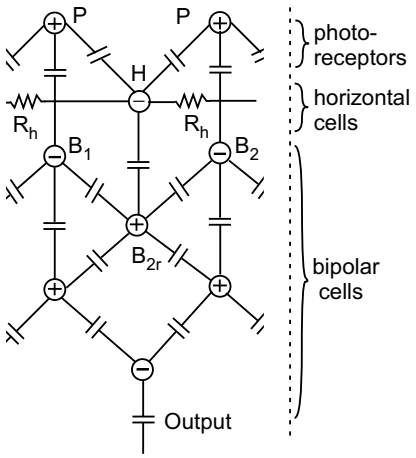

Figure 8.5: Configuration of a unit pixel of the edge detecting circuit consisting of "P", "H", and "B" circuit blocks

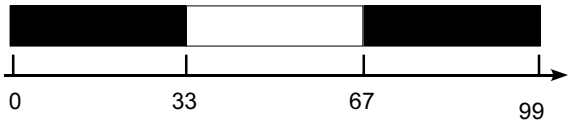

Figure 8.6: Binary image projected onto the one-dimensional retinal circuit

junctions, the firing rate of horizontal cell circuits is somewhat lower than that of corresponding photoreceptor circuits. Figs. 8.7(c) and (d) show the responses of the 50*th* (middle of the illuminated region) and 33*rd* (left edge) bipolar cell circuits respectively. Note that the firing rate of circuits within the illuminated region (Fig. 8.7:(c)) is not zero, however, it is extremely low compared to the edge cells. The simulations were carried out at T = 0 K.

Edge response

Figs. 8.8(a), (b) and (c) correspond to the average tunneling rates for photoreceptors, horizontal and bipolar cell layers. The vertical axes are normalized by the maximum average firing rate in the photoreceptor layer. As mentioned in the preceding section, the average firing rate of the horizontal cells is somewhat lower than that of the photoreceptors. The image edges correspond to the high firing positions of the bipolar cell circuit. However, the firing rates of bipolar cells within the illuminated region have a comparatively low non-zero output.

Sensitivity to light intensity

The firing rate of photoreceptors would be proportional to the intensity of input light (section 8.3.1). To simulate the response of our circuit to various light intensities, we altered the frequency of the applied input pulse trigger, and computed the average tunneling rates of bipolar cells. The results are shown in Fig. 8.9. The maximum response frequency was 110 MHz, determined by the minimum charging period within "P", "H", and "B" cell layer oscillators.

Mach bands

Mach bands are defined as illusory light or dark bands that appear when a spatial ramp in light intensity (in projected images) abruptly changes slope [1],[25] . To confirm the Mach-band response of our circuit, the ramp input shown in Fig. 8.10(a) was fed to the photoreceptor layer. The input was simulated by setting the frequency of the input trigger signal at 10MHz for photoreceptors between nodes 0 and 33, ramp increment between nodes 33 and 67 from 10 MHz to 110 MHz and a constant frequency of 110 MHz for nodes 68-99. The response of the bipolar cell circuit layer (output) is shown in Fig. 8.10(b). The vertical axis is normalized by the firing rate for maximum light intensity (frequency = 110MHz). The circuit could detect the abrupt change in slope of input light intensity. This is shown in Fig. 8.10(b)-"peak", at node positions "33" and "67".

Temperature characteristics

The temperature characteristics were evaluated by computing the circuit's ability to detect edges with increasing temperatures. Figs. 8.11 (a)-(c) show edge responses at T = 0 K, T = 10 K, and T= 20 K respectively. The vertical axes are normalized by the maximum firing rate in the bipolar cell layer at T = 0 K. As the temperature increases, the overall tunneling rates within the circuit increase, leading to a decrement in its ability to detect edges. The ability to detect edges was evaluated as the peak signal to noise ratio (PSNR). To evaluate the overall performance against temperature, the PSNR is defined as:

$$\begin{aligned} \mathrm{PSNR} &\equiv 20\log_{10}\left(\frac{f_{\max}}{\sqrt{\mathrm{MSE}}}\right), \\ \mathrm{MSE} &\equiv \frac{1}{N}\sum_{i=0}^{N-1}\left(f_0(i) - f_{\mathrm{T}}(i)\right)^2 \end{aligned} \tag{8.1}$$

where, $f_{\max}$ is the average firing rate for the entire bipolar circuit at room temperature, MSE is the mean square error, $f_0(i)$ is the firing rate of the ith node

of the bipolar circuit at zero temperature (i.e., the ideal output), and $f_{\mathrm{T}}(i)$ is the firing rate for the ith node of the bipolar circuit at temperature T K, and $N = 100$. The MSE at each temperature was calculated by averaging five runs. The firing rate $f_{\max}$ was 8.33, normalized by the maximum firing rate at 0 K.
Fig. 8.12 shows the PSNR over a temperature range between 0 and 50 K. The circuit could detect edges with a contrast ratio of 23 dB at T = 5 K. This is presumed to be low in comparison to the capacity of the vertebrate retina, (and other electronic systems) in the range of 20 - 40 dB at higher temperatures. This could be attributed to the fact that besides inhibitory mechanisms, there could be other mechanisms involved in edge detection in actual retinas, as compared to our circuit that only modeled inhibition mechanisms [26]-[28]. These could also include stochastic resonance [29], [30], aggregating and thresholding mechanisms together with higher-level visual information processes found in biological systems. Therefore, we think that the PSNR of our circuit could be improved if we were able to incorporate all these mechanisms. A possible architectural approach that could be used to improve performance against temperature, hence PSNR in the proposed circuit, is discussed in section 8.5.

8.4.2 Two-dimensional array circuit

The two-dimensional array was constructed with 100×100 pixel circuits.
Fig. 8.13 shows a schematic top view of the circuit. Each photoreceptor cell is capacitively coupled to four-horizontal cells in the subjacent horizontal layer. Each of the horizontal cells is resistively coupled to its four adjacent cells in the horizontal layer. Similarly, each of the bipolar cells is capacitively coupled to corrresponding cells in the neighboring four-pixels.

Edge response

To confirm the operation of the two-dimensional circuit, a 34×34 pixel sized window was projected into the middle of the array circuit. The response is shown in Fig. 8.14. The photoreceptors receive light inputs to produce a high firing rate (Fig. 8.14(a)). The horizontal cell layer response is shown in (b), while the bipolar cell output is shown in (c). We could successfully detect edges in the projected image.

Temperature characteristics

To analyse temperature characteristics of this circuit, we consider the cross section along A-B, in the middle of the input image (Fig. 8.15). Point ”A” was

taken as node number 0, while B as node number 99. The ability of the circuit to detect edges was analyzed by computing the average tunneling rates of bipolar cells along this cross section. The results are shown in Fig. 8.16, for T = 0 K, 5 K, and 10 K for (a), (b) and (c) respectively. The vertical axis is normalized by the maximum average firing rate of bipolar cell circuits at T = 0 K. The firing rates for all bipolar cells increase with temperature. The performance of the circuit in detecting edges in projected images over a temperature range of 0 - 20 K is shown in Fig. 8.17. The vertical axis represents the peak signal-to-noise ratio (PSNR) defined as:

$$\begin{aligned} \mathrm{PSNR} &\equiv 20\log_{10}\left(\frac{f_{\max}}{\sqrt{\mathrm{MSE}}}\right), \\ \mathrm{MSE} &\equiv \frac{1}{N^2}\sum_{i=0}^{N-1}\sum_{j=0}^{N-1}\left(f_0(i,j) - f_{\mathrm{T}}(i,j)\right)^2 \end{aligned} \tag{8.2}$$

where, $f_{\max}$ is the average firing rate for the entire bipolar circuit at room temperature, MSE is the mean square error, $f_0(i,j)$ is the firing rate for the $[i,j]$th node of the bipolar circuit at zero temperature (i.e. the ideal output), and $f_{\mathrm{T}}(i,j)$ is the firing rate for the $[i,j]$th node of the bipolar circuit at temperature T K, and $N = 100$. The MSE was obtained by averaging five runs at each temperature. The firing rate $f_{\max}$ was 11.36, normalized by the maximum firing rate for the bipolar cell layer at 0 K.

Edge enhancement in a gray image

Fig. 8.18 shows the edge computation results of a 100×100 sized gray image projected onto the two-dimensional circuit. Fig. 8.18(a) is the input image. The dark region represents non-illuminated pixels of the array. The coloring in (b), and (c) corresponds with firing rates of the oscillators, with the dark coloring representing a zero firing rate, and the white representing a high firing rate. The edge detection results at T = 0 K, and T = 5 K are shown in Figs. 8.18(b) and (c) respectively. As the temperature increases, the firing rate of the entire the circuit increases. This is indicated by the grayish background in Fig. 8.18(c). This would increase with temperature, leading to a low edge extraction capacity.

8.5 Discussion: Improving temperature performance

Stochastic resonance is a phenomenon where weak signals can be retrieved from a noisy output [14],[35] by applying an optimal ammount of random noise.

Single-electron devices are sensitive to thermal noises. As shown in our results, the probability of random electron tunneling (firing) rises as the temperature increases, degrading the capacity of edge detection. One method of improving the circuit performance in relation to temperature is to utilize these thermally induced noises (random tunneling events). Living organisms are immune against noise in information processing; they effectively process information even in noisy environments [29],[30]. It is presumed that one of the ways they are able to do so is by exploiting stochastic resonance (SR) [36]. Oya *et al*., [37] proposed a single-electron neural network and demonstrated its improved temperature performance by employing SR in detecting output signals. This was achieved by setting the input signal to a value lower than the tunneling (firing) threshold of the neurons. By applying thermal noises, neurons with non-zero inputs were thermally induced to tunnel—tunneling events were synchronized with the input signal to a certain quantity of thermal noises. They found that the neuron performance against noises was enhanced through partially using thermal noises. We could use the same method in our edge-detecting circuit, where a number of circuit blocks would be fed with the same input. After each of the blocks processes the input image, their outputs would be summed to produce the overall output. Through this process, we could be able to successfully carry out edge detection with improved performance at higher temperatures. Therefore, applying the SR phenomenon to the proposed circuit would enhance temperature performance, hence increased PSNR against thermally induced noise, without an immediate need to find a solution through fabrication techniques.

8.6 Summary

Toward creating *neuromorphic architectures* with nano-electronic devices, we proposed a single-electron circuit that can detect edges in incident images. Based on a well studied retinal model, we implemented the model with single-electron devices, and confirmed its basic performance through Monte-Carlo based simulations.

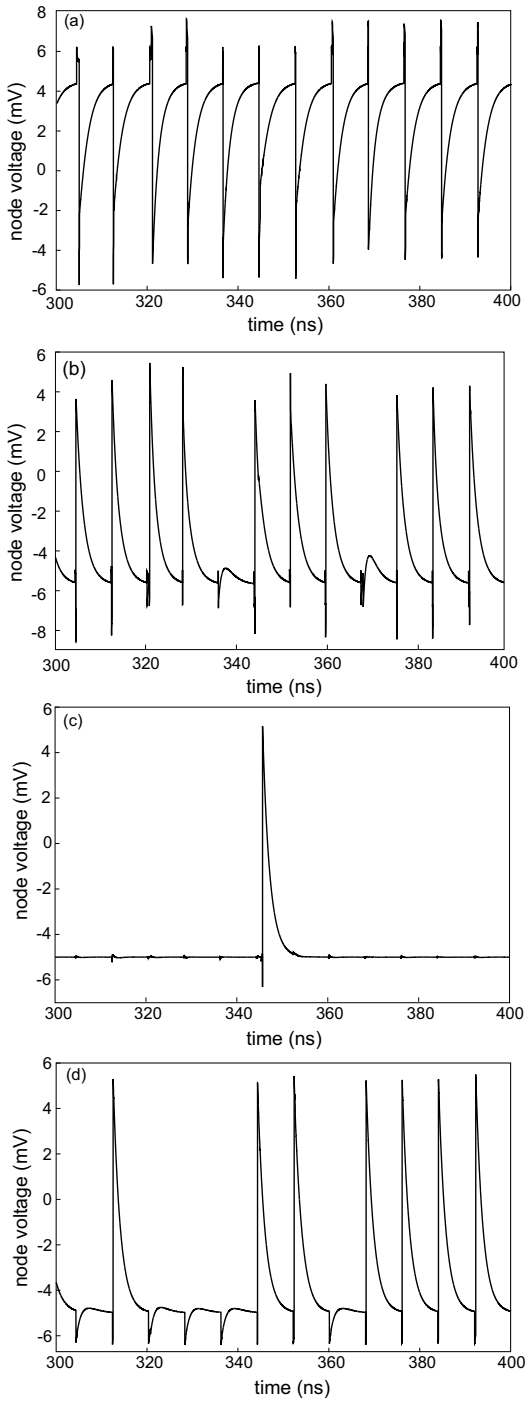

Figure 8.7: Transient responses of constitutive circuit cells: (a) Photoreceptors, (b) Horizontal cells, (c), and (d) Bipolar cell circuits. (c) shows the response of bipolar cells in the middle of illuminated region, while (d) shows response of those in the edges of the illuminated region. The simulation temperature T = 0 K

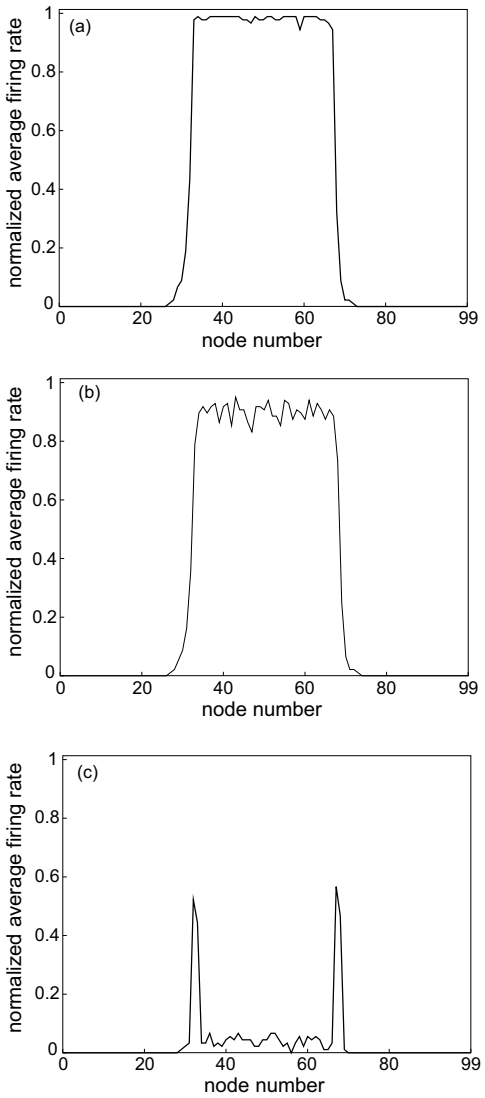

Figure 8.8: Response to input images: (a) Average firing rate for photoreceptors—input, (b) Average firing rate for horizontal cells, and (c) Average firing rate of bipolar cells—output (T = 0 K)

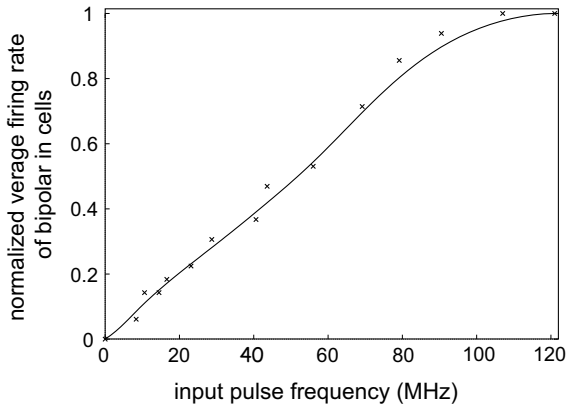

Figure 8.9: Response to light intensity, simulated by varying frequency of input trigger signal—horizontal axis: The vertical axis represents the maximum firing rate of edge cell circuits, normalized by the firing rate for maximum light intensity (frequency = 110MHz). Simulated at T = 0 K

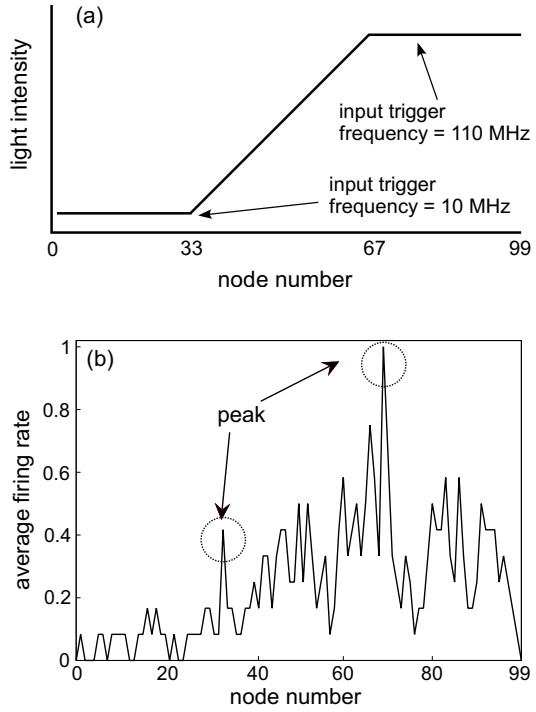

Figure 8.10: Mach band: (a) Light intensity profile of input image, and (b) Response—average firing rate for bipolar cells (T = 0 K)

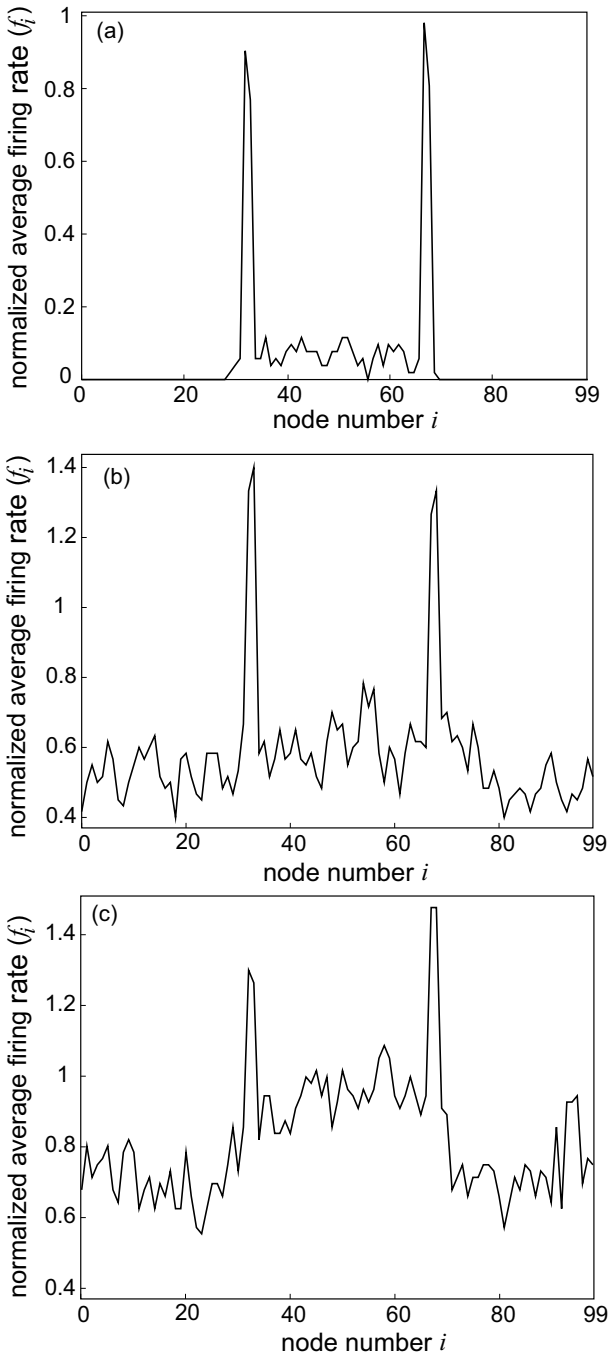

Figure 8.11: Edge detection at sample temperatures: (a) Temperature T = 0 K, (b) Temperature T = 10 K, and (c) Temperature T = 20 K

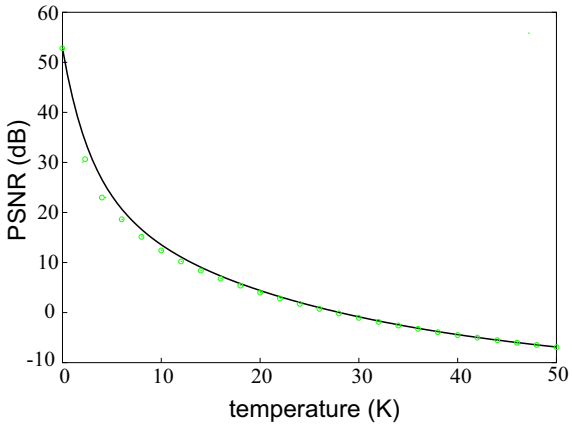

Figure 8.12: Edge detection capacity (peak signal to noise ratio) for T = 0 - 50 K

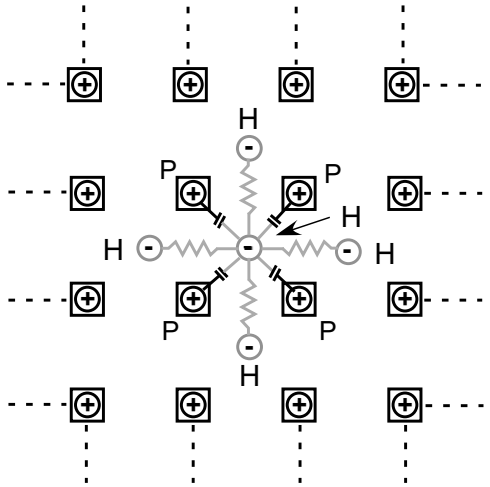

Figure 8.13: Schematic of the two-dimensional circuit configuration, showing positions of photoreceptor and horizontal cells

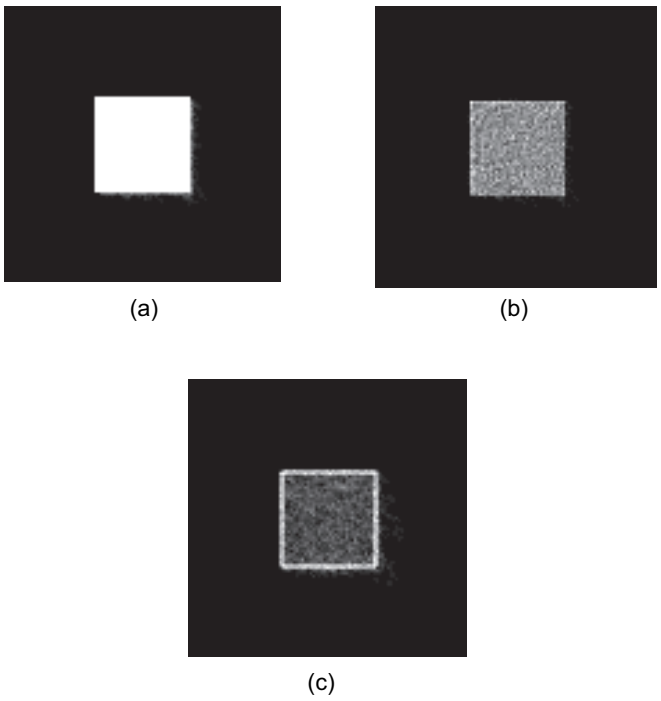

Figure 8.14: Response of (a) Photoreceptors, (b) Horizontal cells, and (c) Bipolar cells to incident image (T = 0 K)

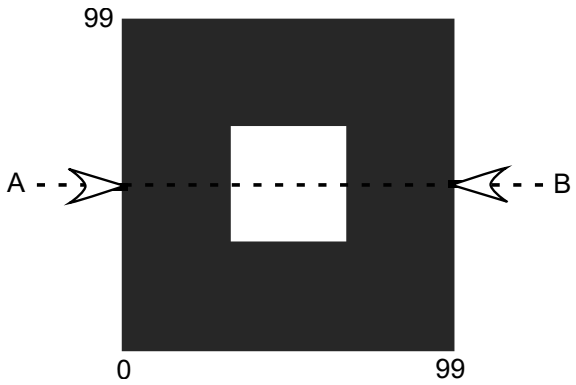

Figure 8.15: Schematic diagram showing cross section "A-B" along which temperature characteristics were analyzed.

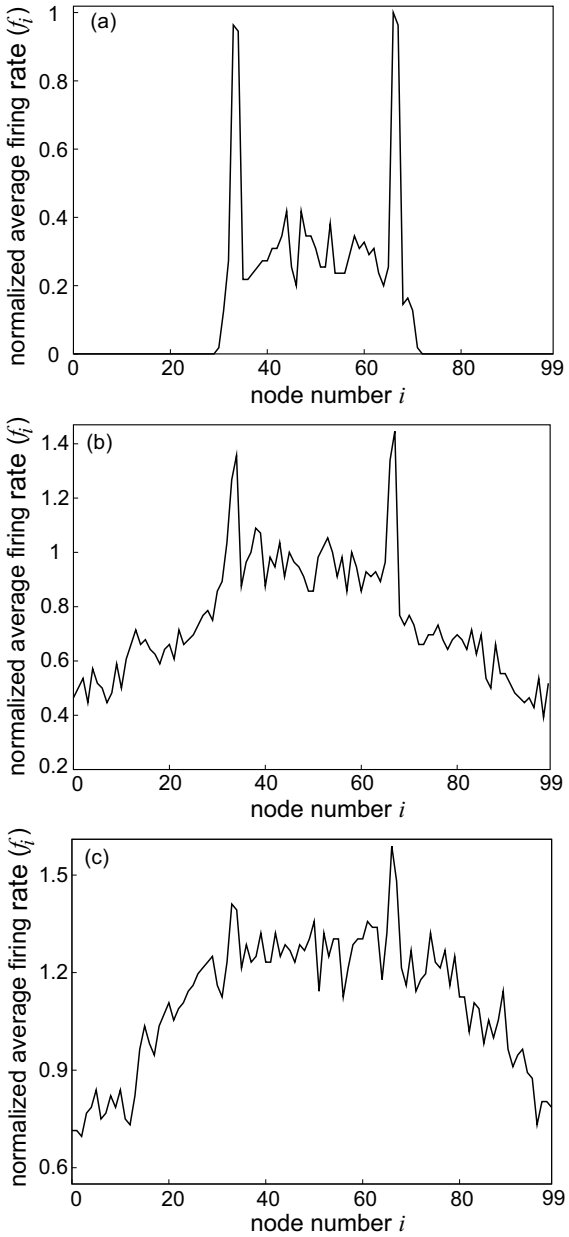

Figure 8.16: Firing rates for bipolar cell circuits along cross section A-B at smple temperatures. (a) T = 0 K, (b) T = 5 K, and (c) T = 15 K

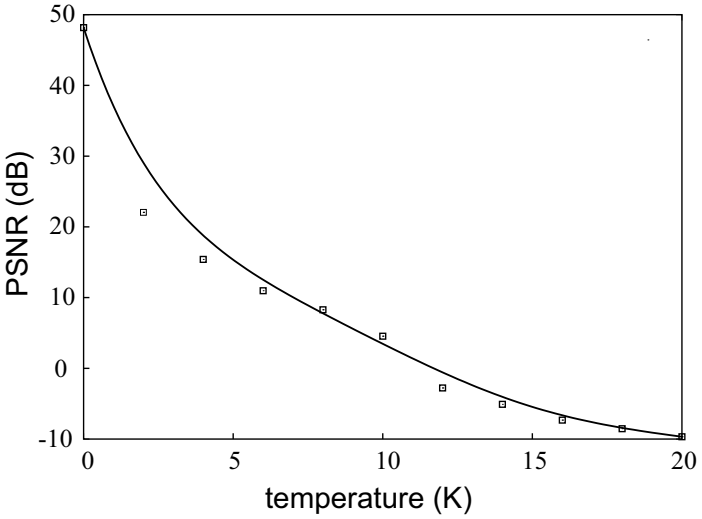

Figure 8.17: Edge detection capacity (PSNR) over a temperature range of T = 0 - 20 K

Figure 8.18: Edge detection results for gray image: (a) Input image, (b) and (c): Edge detection results at T = 0 K (b), and T = 5 K (c)

References

[1] C. Mead: Analog VLSI and neural systems, New York: Addison Wesley, 1989.

[2] A. Moini: Vision Chips, Kluwer, 1999.

[3] S.-C. Liu, J. Kramer, G. Indiveri, T. Delbruck and R. Douglas: Analog VLSI: Circuits and Principles, MIT Press, 2002.

[4] C. Washubber: Computational Single-Electronics, Springer, 2001.

[5] See, for example, K.K. Likharev: Proc. of IEEE, Single-electron devices and their applications, Vol. 87, pp. 606-632, 1999; and references therein.

[6] M.N. Shadlen and W.T. Newsome: The Variable Discharge of Cortical Neurons: Implications for Connectivity, Computation, and Information Coding, J. of Neuroscience, Vol. 18, pp. 3870–3896, 1998.

[7] J.N. Shint, K.R. Lee and S.B. Park: Novel neural circuits based on stochastic pulse coding and noise feedback pulse coding, Int. J. of Electronics, Vol. 74, pp. 359–368, 1993.

[8] W.R. Softky and C. Koch: The highly irregular firing of cortical cells is inconsistent with temporal integration of random EPSPs, J. of Neuroscience, Vol. 14, pp. 334–350, 1993.

[9] C.L. Passaglia and J.B. Troy: Impact of Noise on Retinal Coding of Visual Signals, J. Neurophysiology, Vol. 92, pp. 1023-1033, 2004.

[10] J. B. Demb, P. Sterling and M. A. Freed: How Retinal Ganglion Cells Prevent Synaptic Noise From Reaching the Spike Output, J. Neurophysiology, Vol. 92, pp. 2510 - 2519, 2004.

[11] M.C.W. van Rossum, B. J. O'Brien and R. G. Smith: Effects of Noise on the Spike Timing Precision of Retinal Ganglion Cells, J. Neurophysiology, Vol. 89, pp. 2406-2419, 2003.

[12] L. J. Croner, K. Purpura and E. Kaplan: Response variability in retinal ganglion cells of primates, Proc. Natl. Acad. Sci. USA, Vol. 90, pp. 8128-8130, 1993.

[13] N. Barkai and S. Leibler: Robustness in simple biochemical networks, Nature, Vol. 387, pp. 855–857, 1997.

[14] M. Morohashi, A.E. Winn, M.T. Borisuk, H. Bolouri, J. Doyle and H. Kitano: Robustness as a measure of plausibility in models of biochemical network, J. Theoret. Biol., Vol. 216, pp. 19-30, 2002.

[15] H. Kitano: Biological robustness, Nat. Rev. Genet., Vol. 5, pp. 826–837, 2004.

[16] R. Douglas, M. Mahowald and C. Mead: Neuromorphic analogue VLSI, Annual Review of Neuroscience, Vol. 18, pp. 255-281, 1995.

[17] H. Gravert and M.H. Devoret: Single Charge Tunneling—Coulomb Blockade Phenomena in Nanostructures, Plenum Press, 1992.

[18] K.K. Likharev and A.B. Zorin: Theory of the Bloch-wave oscillations in small Josephson junctions, J. of Low Temp. Phys., Vol. 59, pp. 347-382, 1985.

[19] D.V. Averin and K.K. Likharev: Coulomb blockade of single-electron tunneling and coherent oscillations in small tunnel junctions, J. of Low Temp. Phys., Vol. 62, pp. 345-373, 1986.

[20] A. Fujiwara, Y. Takahashi and K. Murase: Observation of single electron-hole recombination and photon-pumped current in an asymmetric Si single-electron transistor, Phys. Rev. Lett., Vol. 78, No. 8, pp. 1532-1535, 1997.

[21] R. Nuryadi, Y. Ishikawa and M. Tabe: Single-photon-induced random telegraph signal in a two-dimensional multiple-tunnel-junction array, Phys. Rev. B, Vol. 73, pp. 45310-45316, 2006.

[22] T. Oya, T. Asai, T. Fukui and Y. Amemiya: Reaction-Diffusion Systems Consisting of Single-Electron Oscillators, Int. J. Unconventional Computing, Vol. 1, No. 2, pp. 177-194, 2005.

[23] T. Oya, A. Schmid, T. Asai, Y. Leblebici and Y. Amemiya: On the fault tolerance of a clustered single-electron neural network for differential enhancement, IEICE Electronics Express, Vol. 2, No. 3, pp. 76-80, 2005.

[24] T. Oya, T. Asai, R. Kagaya, T. Hirose and Y. Amemiya: Neuronal synchrony detection on signle-electron neural network, Chaos, Solitons & Fractals, Vol. 27, No. 4, pp. 887-894, 2006.

[25] E. M. LowRY and J.J. DE PALMA: Sine-wave response of the visual system. I. The Mach phenomenon, J. Opt. Soc. Am., Vol. 51, pp. 740-746, 1961.

[26] R. H. Masland: The fundamental plan of the retina, Nature Neuroscience, Vol. 4, pp. 877–886, 2001.

[27] R. H. Masland: Neuronal diversity in the retina, Current Opinion in Neurobiology, Vol. 11, pp. 431-436, 2001.

[28] S. M. Wu, F. Gao and B. R. Maple: Functional Architecture of Synapses in the Inner Retina: Segregation of Visual Signals by Stratification of Bipolar Cell Axon Terminals, The J. of Neuroscience, Vol. 20, pp: 4462–4470, 2000.

[29] W. R. Adey: Organization of brain tissue: Is the brain a noisy process?, Int. J. Neurosci., Vol. 3, pp. 271-284, 1972.

[30] J. J. Collins, C. C. Chow and T. T. Imhoff: Stochastic resonance without tuning, Nature, Vol. 376, pp. 236-238, 2002.

[31] T. Oya, T. Asai, T. Fukui and Y. Amemiya: A majority-logic nanodevice using a balanced pair of single-electron boxes, J. of Nanoscience and Nanotechnology, Vol. 2, No. 3/4, pp. 333-342, 2002.

[32] K. Kumakura, J. Motohisa and T. Fukui: Formation and characterization of coupled quantum dots (CQDs) by selective area metalorganic vapor phase epitaxy, J. Crystal Growth, Vol. 170, No. 1, pp. 700-704, 1997.

[33] L. Yang, J. Motohisa, J. Takeda and T. Fukui: Photonic crystal slabs with hexagonal airholes fabricated by selective area metal organic vapor phase epitaxy, Sensors and Actuators; A, Vol. 133, pp. 288-293, 2007.

[34] L. Gammaitoni, P. Hanggi, P. Jung and F. Marchesoni: Stochastic resonance, Reviews of Modern Physics, Vol. 70, No. 1, 1998.

[35] E. Simonotto, M. Riani, C. Seife, M. Roberts, J. Twitty and F. Moss: Visual Perception of Stochastic Resonance, Phy. rev. lett., Vol. 78, No. 6, pp. 1186-1189, 1997.

[36] J. K. Douglass, L. Wilkens, E. Pantazelou and F. Moss: Noise enhancement of information transfer in crayfish mechanoreceptors by stochastic resonance, Nature, Vol. 365, pp. 337-340, 1993.

[37] T. Oya, T. Asai, R. Kagaya, S. Kasai and Y. Amemiya: Stochastic resonance among single-electron neurons on Schottky wrap-gate device, Int. Cong. Series, Vol. 1291, pp. 213-216, 2006.

9

Pulse density modulation circuits exploiting noises to improve signal-to-noise ratio

9.1 Introduction

This chapter investigates how we can employ noises, instead of eradicating them, to improve the performance of LSI circuits. This is done by investigating the performance of two circuit architectures, inspired by pulse-density modulation in neurons. In the first circuit, we show that indeed introducing noises improves noise shaping characteristics of the proposed analog-to-digital converter circuit, hence increasing signal-to-noise ratio. In the second circuit, we investigate the implications of noises in improving the fidelity with which the proposed neuronal circuit can transmit high frequency signals. In both cases, we found that introducing noises reduces the probability of synchrony, leading to random firing events in the circuit network. This in turn improves temporal resolution with which the neuron network can track input signals. The chapter is organized as follows. First, a preview of signal processing in neurons is provided, followed by investigation on the first proposed circuit: noise-shaping in a population of single-electron network. This is followed by the second proposed circuit: implications of noises in the fidelity of signal transmission.

9.1.1 A short review of pulse-density modulation in neurons

A neuron aggregates inputs from other neurons connected through synapses. The aggregated charge raises the membrane potential until it reaches a threshold, where the neuron fires generating a spike. This spike corresponds to a binary output “1”. After the firing event, the membrane potential is reset to a low value, and it increases again as the neuron accepts inputs from neighboring neurons (or input signals) to repeat the same cycle; producing a stream of “one”

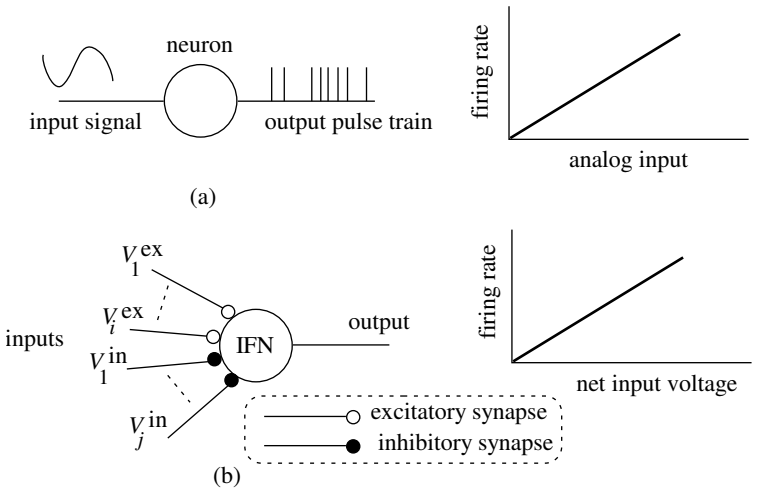

Figure 9.1: (a) Pulse density modulation in neurons: analog input is converted into a pulse train whose density is proportional to the net amplitude of the input signal. (b) Fundamental structure and operation of integrate-and-fire neurons (IFNs). The IFN receives input voltages through excitatory and inhibitory synapses, and produces pulses when the net input voltage exceeds the threshold. The output pulse density (firing rate) is proportional to the net input voltage.

and "zero" pulse trains. The operation of neurons is often modeled with spiking neurons such as the integrate-and-fire neurons. Fig. 9.1(b) illustrates the fundamental operation of an integrate-and-fire (IFN) neuron. The open circles (○) and shaded circles (●) represent excitatory and inhibitory synapses, respectively. The IFN receives input signals (voltages) through the excitatory synapses (to raise its membrane voltage) and inhibitory synapses (which decrease the membrane voltage) from adjacent neurons, to produce a spike if the summed input voltage ($\sum V_i^{\rm ex} - \sum V_j^{\rm in}$) exceeds the threshold voltage. After the IFN fires, its membrane voltage is reset to a low value, and the integration action resumes.

9.1.2 Single-electron integrate and fire neuron

A single-electron oscillator is used to model the operation of an integrate-and-fire neuron (IFN). The structure and operation of a single-electron oscillator is shown in Fig. 9.8(a) and (b), respectively. A single-electron oscillator produces self-induced relaxation oscillations if the bias voltage is higher than the tunneling threshold . The node voltage V_1 increases as the capacitance $C_{\rm j}$ is charged through the series resistance (curve AB), until it reaches the tunneling threshold $e/(2C_{\rm j})$, at which an electron tunnels from the ground to the nanodot across the

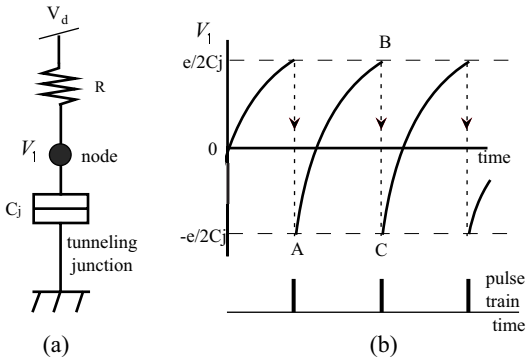

Figure 9.2: Single-electron neuron: (a) circuit configuration and (b) waveform showing oscillation of node voltage V_1, as capacitor Cj is charged through resistance R (from A to B) and reset by an electron tunneling from the ground to the node (voltage drop from B to C). This sudden drop in the node voltage (BC) corresponds to a pulse output.

tunneling junction, resetting the node voltage to $-e/(2C_{\rm j})$. This abrupt change in node potential (from B to C) can be referred to as a firing event. The nanodot is recharged to repeat the same cycles. Therefore, a single-electron oscillator could be viewed as an integrate and fire neuron, which aggregates input voltages (or inputs from from neighboring neurons) producing a pulse when its node voltage reaches the threshold voltage. A detailed explanation of the operation of a single-electron oscillator is shown in chapter 7.

9.2 A pulse-density modulation circuit exhibiting noise shaping with single-electron neurons

9.2.1 Model and circuit implementation

Fig. 9.3 shows the model of the proposed circuit, consisting of three neuronal elements, the minimum number of units required to achieve a considerable signal-to-noise ratio ([2]). The neurons receive the same analog input through excitatory synapses (○) and produce digital pulses toward the global inhibitor Σ [9]. The output is fed-back to the three elements through inhibitory synapses denoted by shaded circles (●) in the network. Firing in any of the neurons in the network decreases the membrane potential of the other neurons, reducing the probability of their firing.

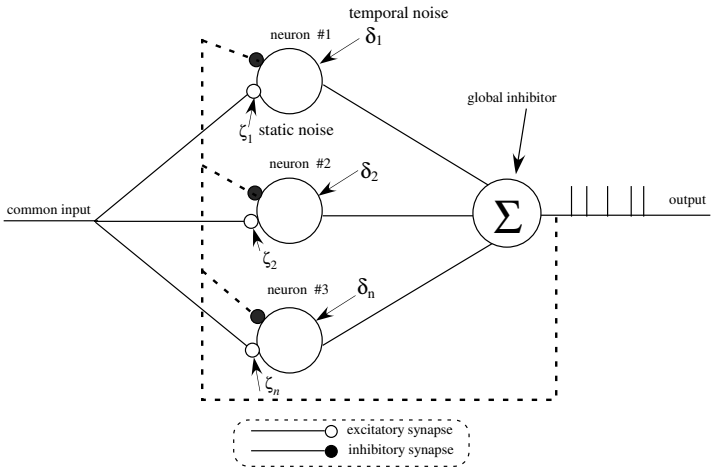

Figure 9.3: Model of pulse-density modulation circuit employing excitatory and inhibitory mechanisms. A common input is fed to the three neurons through excitatory synapses (○), while the output is fedback to the three neurons through inhibitory synapses (●).

The neuronal structure in Fig. 9.3 is implemented with single-electron oscillators that receive the same analog input. Each neuron in the network is implemented with a single electron oscillator. The input induces electron tunneling in the single-electron oscillators, generating pulses toward the global inhibitor. The global inhibitor (Σ) sums the pulses to produce a train of spikes representing tunneling (firing) events in the three neurons. Fig. 9.10 shows the circuit configuration. The global inhibitor is realized by numerically summing the firing events in the network. Inhibitory synapses are implemented by coupling capacitances (C), that decrease the node voltages of all the oscillators once a pulse is released at the output.
Each neuron in the network receives the same input ($V(\mathrm{t})$) raising its node voltage. Whenever any of the three single-electron oscillators reaches its threshold voltage, it fires, releasing a pulse toward the global inhibitor. The global inhibitor, through the coupling capacitors C, subtracts a certain amount of voltage from the other oscillators, suppressing them from tunneling for a certain period of time. This contributes to the distribution of output pulses. In the absence of the global inhibitor, all the neurons would fire randomly and with almost the same timing, producing a Poisson-like distribution of inter-spike intervals (ISIs). Contrally, by introducing the global inhibitor, consecutive firing events in the network are suppressed, resulting in a Gaussian-like distribution of ISIs in the coupled network.

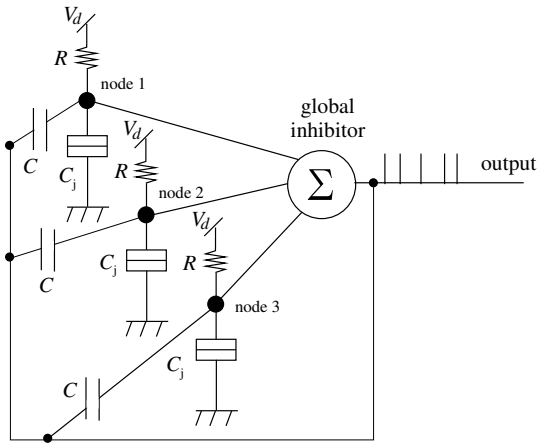

Figure 9.4: Single-electron circuit performing pulse-density modulation. The structure consists of three single-electron oscillators, and a global inhibitor Σ. The output is fed back to all the other oscillators through the capacitive coupling C.

9.2.2 Simulation results

As mentioned in the introduction, the noise-shaping properties of the network of model neurons were reportedly improved by introducing dynamic and static noises [7]. In our circuit, this was realized as follows. As noted earlier, thermal noises lead to random electron tunneling in single-electron devices. We therefore introduced dynamical noises by tuning the temperatures in both the coupled and the uncoupled networks. Static noises were introduced only in the coupled network, by varying the values of series resistances R. In the coupled network, all the series resistances were set to 44 MΩ, whereas in the coupled network, the mean value of the three resistances was 44 MΩ (to obtain a ISI distribution with a standard deviation of one sigma), and the variance was $\pm 12.5\%$. The inhibitory coupling in the coupled network was implemented with a capacitive coupling of 4 aF. The temperature was set to 0.5 K in all simulations.

The performance of both the coupled and the uncoupled circuits was investigated through Monte-Carlo based computer simulations. All the circuit units in both the coupled and the uncoupled networks were fed with an input $V_d = 7.85$ mV.

Fig. 9.12 shows the raster plots of the firings of the network elements. The top diagrams of (a) and (b) show the random pulses for each unit in the uncoupled and coupled networks, respectively. The bottom diagrams in (a) and (b) show the summed output (pulse train) for all the elements in the uncoupled and coupled networks, respectively. From the diagrams, we could observe that the firing timings in the uncoupled network were random and all the neurons fired with almost the same timing. In the coupled network, however, the firing of one of the

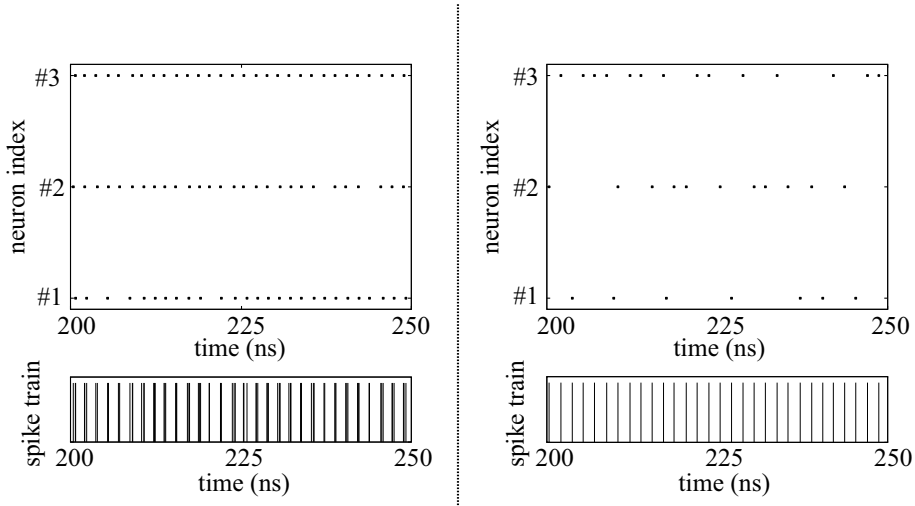

Figure 9.5: Raster plots for firing events for uncoupled (left diagrams) and coupled (right diagrams) networks. The top diagrams show firing events for each neuron, while the bottom diagrams show summed output spike train at the global inhibitor Σ. Firing events in the uncoupled network were random and almost consecutive, whereas firing timings in the coupled network were well distributed as a result of the inhibitory coupling inhibiting concurrent events.

neurons inhibited the others from firing, thus reducing the probability of consecutive firing in the network. In addition, the variance in the series resistances results in variations in the time constants of the network neurons. This reduced the probability of neurons attaining the firing threshold at the same time, and thus improved the distribution of firing intervals in the network. Consequently, these two factors resulted in well distributed firing timings in the network, leading to a Gaussian-like distribution of inter-spike intervals.
Fig. 9.13 shows the ISI distribution of firing events in the whole network. The histogram for the coupled network shows a Gaussian-like distribution with an inter-spike interval of 1.65 ns at the maximum number of firing counts. The histogram for the uncoupled network, in contrast, shows a Poisson-like distribution. We also investigated the effect of increasing the variance in the series resistances on the standard deviation of the Gaussian-like distribution. We found that the standard deviation increases as the variation decreases below or increases above 12.5 %. As the variance decreases, the probability that multiple neurons in the network reach the threshold voltage at the same time increases. This shifts the ISI at the maximum firing rate toward zero, consequently leading to a larger standard deviation of the ISI distribution. The ISI distribution can,

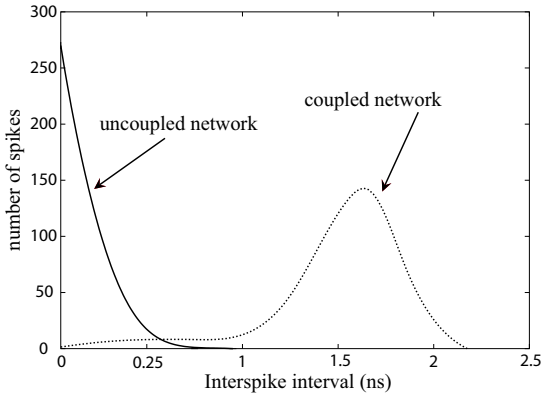

Figure 9.6: Histogram of inter-spike intervals (ISIs) for coupled and uncoupled networks. The uncoupled network shows a Poisson-like distribution of ISIs where the firing events in the network elements are almost concurrent. The coupled network shows a Gaussian-like distribution, as a result of distributed firing events.

however, be tuned by adjusting the value of the inhibitory coupling capacitance C. As the coupling strength increases, the number of neurons reaching the threshold concurrently decreases drastically. In otherwords, the firing timings tend to distribute evenly, resulting to a sharper Gaussian-like distribution. However, increasing the coupling strength to a relatively high value, beyond the optimal value (of 4 aF in our simulations), leads to a winner-takes-all [10] operation (where only one neuron in the network produces the highest spike rate and inhibits all the others from firing). This would be undesirable, especially in a network of fault- and defect-prone elements, where increasing the probability of correct operation requires that all the elements play a substantial part in the network operation (i.e. a winners-share-all [11] operation, where several neurons in the network survive). Thus obtaining an ideal operation of the network requires tuning the firing rates of individual neurons though the series resistances, and also tuning the summed firing rate of the network through the capacitive coupling to obtain a winners-share-all type function.
Fig. 9.7 shows the power spectra for the coupled and uncoupled networks. The three neurons in both networks were fed with a sinusoidal input $V_d = V_0 + \mathrm{A}\sin(2\pi ft)$, where amplitude $A = 2.5$ mV, frequency $f = 100$ MHz, and bias voltage $V_0 = 7.85$ mV. The power in both cases was calculated with 25 runs averaged with a square window. From the results we can confirm that the global inhibitory coupling and the heterogeneity in series resistances collectively helped reduce the noise level in the coupled network substantially. The signal-to-noise ratio in the uncoupled network was 22.96 dB, while that in the

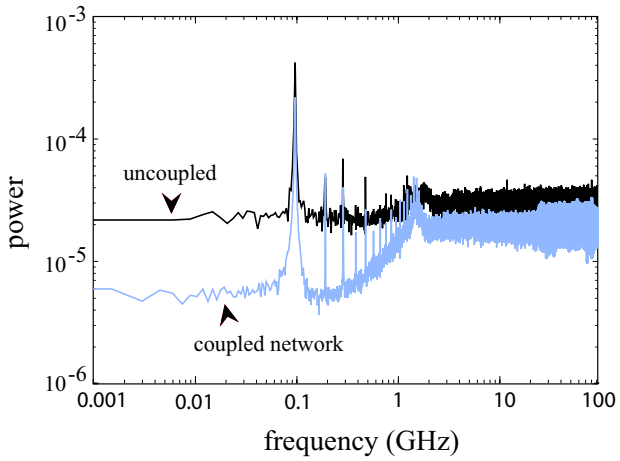

Figure 9.7: Power spectra of coupled and uncoupled networks. The coupled network shows a reduced noise level in the lower frequencies (signal band), improving the SNR with 4.34 dB as compared to the uncoupled network.

coupled network was 27.30 dB below the cutoff frequency of 1 GHz. The harmonic distortions in the results are due to (i) the intrinsic firing rates of the individual neurons in the network and (ii) non-linear feedback introduced to the network. These distortions degraded the SNR characteristics. They could be decreased by setting the input signal frequency to a value much lower than the firing frequencies of individual neurons in the network. Another way of increasing the SNR without tuning the input frequency would be by filtering the output signals, to get rid of the higher frequencies. This is often realized with digital filters in the feedback loop of $\Sigma - \Delta$ converters [12].

9.3 Implications of temporal noises and device fluctuations in enhancing fidelity of signal transmission in single-electron neural circuits

9.3.1 Model and circuit structure

This study is based on a model of the vestibulo-ocular reflex (VOR) proposed by Hospedales et al. ([15]). In their work, they reported that noises and heterogeneity in the intrinsic response properties of neurons account for the high-fidelity in VOR functionality.

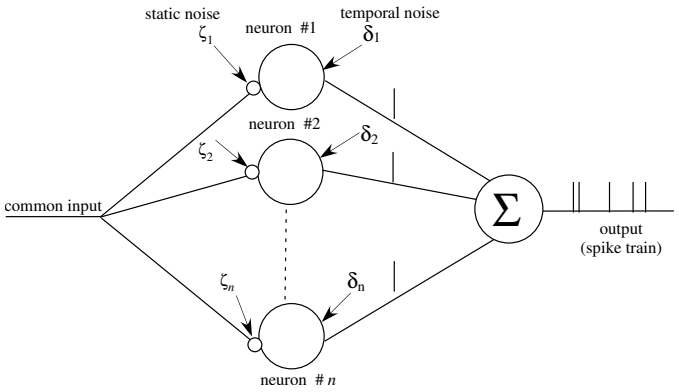

Figure 9.8: Neural network model of signal encoding in the VOR consisting of n neurons.

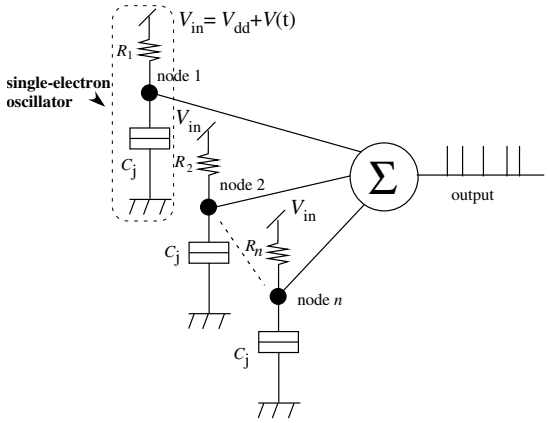

Figure 9.9: Implementation of the model with single-electron oscillators.

Fig. 9.8 shows the part of the model, which converts head movements into neural spikes in the VOR, consisting of n neurons. The structural heterogeneity in the membrane time constants of individual neurons is represented by ξ_i. We refer to this heterogeneity as static noises. The neurons receive a common analog input and produce spikes whose temporal density corresponds to the amplitude of the input signal. The output terminal receives pulses from all the neurons in the network to produce a spike train. The noises introduced into the network lead to random and independent firing events in the neurons, reducing the probability of synchrony in the network. This enhances the precision with which the neurons in the network can encode signals with input frequencies higher those of individual neurons.

The above network is implemented with single-electron IFNs (oscillators) as shown in Fig. 9.9. A single-electron oscillator consists of a tunneling junction $C_{\rm j}$,

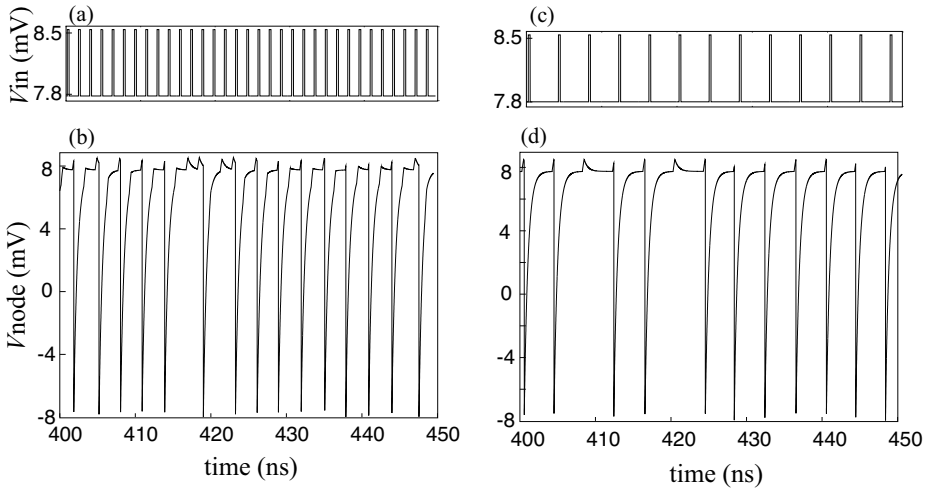

Figure 9.10: Transient response of a single neuron. (a) and (c) show input signals with input frequencies of 600 MHz and 250 MHz, respectively. (b) and (d) show the output characteristics of neurons fed with input signals of 600 MHz and 250 MHz, respectively.

resistance R_{i} and a bias voltage source V_{in}. The node voltage of the oscillator remains stable, if the bias voltage is lower than the tunneling threshold. When the node voltage of the oscillator increases beyond the threshold voltage, say as a result of an incoming input pulse, an electron tunnels from the ground to the node, leading to an abrupt change in the node voltage. This is referred to a firing event. The node voltage is recharged back to the resting potential to repeat the same process. Each neuronal element in the network is implemented with a single-electron neuron. From a previous study, we established that the minimum number of neuronal elements required in such a network could be as small as three. Therefore in the present investigation the number of neurons was set to three.

The heterogeneity in the model was introduced in the circuit as a variation in the series resistance R_{i}. Note that R_{i} is a critical parameter in setting the intrinsic response frequency of each neuron. Therefore, by tuning the values of R_{i}, we could simulate the heterogeneity of membrane time constants of actual neurons.

9.3.2 Simulation results

In the simulations, all the neurons were connected to a input voltage $V_{\mathrm{in}} = V_{\mathrm{dd}} + V(\mathrm{t})$, where V_{dd} (bias voltage) was set to 7.8 mV to achieve a

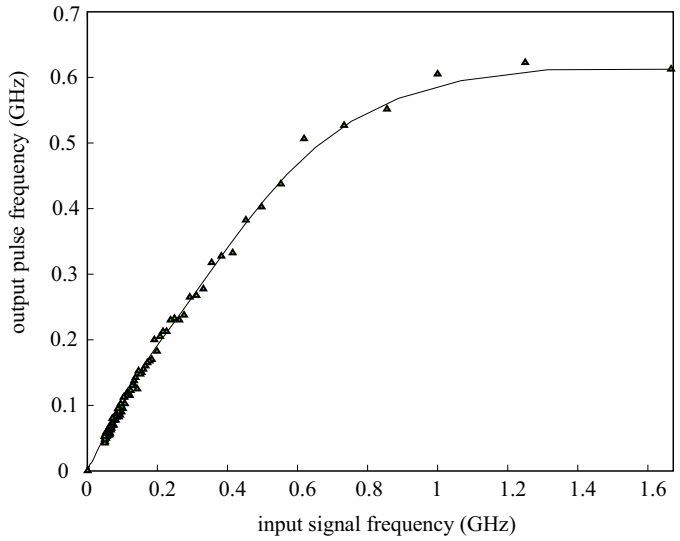

Figure 9.11: Output firing rate of a single neuron plotted against the input pulse frequency.

monostable stable operation in the absence of input signals, $V(\mathrm{t})$ is a pulsed input signal with an amplitude of 0.8 mV. The capacitance of the tunneling junctions C_{j} was set to 10 aF. The simulation time was set to 800 ns, while the operation temperature T was set to 0.5 K for simulation results shown in Figs. 9.10, 9.12 and 9.13(b) and (c).

Fig. 9.10 shows the transient response of a single neuron. Fig. 9.10(a) and (c) show the respective input signals with a frequency of 600 MHz and 250 MHz, respectively. Fig. 9.10(b) shows the neuron response to input "(a)", while "(d)" shows the neuron response to input "(c)". The series resistance was set to $100\mathrm{M}\Omega$. Fig.9.10(d) shows successful encoding of the input signal (the neuron fires once for each pulse in the input signal [1]) whose frequency is within the intrinsic firing rate of a single neuron. In Fig. 9.10(b), the neuron could only encode some of the input pulses, leading to a lower firing rate as compared to the input rate. In other words, the neuron in (b) could only transmit some of the input pulses toward the output. This degrades the fidelity of signal transmission along the neural network. Fig. 9.11 shows the response of a single neuron over a wide range of input frequencies. The horizontal axis shows the input frequency, while the vertical axis shows the average firing rate of the neuron. The neuron response was linear

[1]Tunneling (firing) in single-electron devices involves a probabilistic time lag or waiting time between when the node voltage exceeds the threshold voltage and when an electron can actually tunnel from the ground to the node, releasing a spike toward the output terminal. Due to the effect of the time lag, a neuron might fail to fire even after achieving the tunneling conditions as seen in Fig. 9.10(d). As a result, the average firing rate would be somewhat lower than the input pulse rate

for input signals with a frequency of up to 500 MHz. Beyond this range, the output was highly distorted. This shows that a single neuron can successfully encode (respond to) signals with a maximum input frequency of 500 MHz.
The response of a population of neurons to various input frequencies was investigated with two sets of neuron ensembles: homogeneous and heterogeneous networks. In the homogeneous ensemble, the series resistances R_1, R_2, and R_3 were set to the same value, whereas in the second set, heterogeneity (static noises) was introduced by varying the values of series resistances in the three neurons. The results are shown in Figs. 9.12 and Fig. 9.13.
Fig. 9.12(a) shows the input signal with a frequency of 600 MHz. Figs. 9.12(b-1) and (c-1) show the response of the homogeneous network, where the series resistances R_1, R_2 and R_3 were set to 100 $\mathrm{M}\Omega$. Fig. (b-1) shows the firing events of individual neurons in the network. Fig. (c-1) shows the summed spike output (spike train) at the output terminal. We could confirm that the neurons in the homogeneous network tend to synchronize, emitting pulses at almost the same timing.
Figs. 9.12 (b-2) and (c-2) show the response of neurons in the heterogeneous network, where the series resistances were set to 110 $\mathrm{M}\Omega$ for neuron 1, 100 $\mathrm{M}\Omega$ for neuron 2 and 90 $\mathrm{M}\Omega$ for neuron 3. The firing events in the heterogeneous network are more or less random as shown in Fig. 9.12(b-2). The probability of having a neuron with a potential near the threshold value, at any given moment, is higher than in the case of a homogeneous network. Thus the network can respond to any incoming pulses at a higer probability. This results in an improved encoding of the input as illustrated by the spike train shown in Fig. 9.12(c-2). In other words, since the neurons fired irregularly, they could transmit the input pulses with a higher temporal precision as opposed to the homogeneous network. This is elaborated in more detail in Fig. 9.13 (curves (b) and (c)), where the transmission of signal over a wide range of frequencies is demonstrated. The horizontal axis represents the frequency of input signals, while the vertical axis shows the average firing rate (output frequency) for both neuron sets. In the case of the homogenous network, since the neurons tend to synchronize with time, their encoding frequency is the same as that of individual neurons. Contrary, neurons in the heterogeneous network could correctly encode signals with input frequencies up to 1 GHz, twice that of the homogeneous network. This demonstrates that heterogeneity in the circuit parameters (presence of static noises) plays an important role in improving the fidelity with which neurons can encode signals with input frequencies far beyond the encoding capacity of individual neurons.

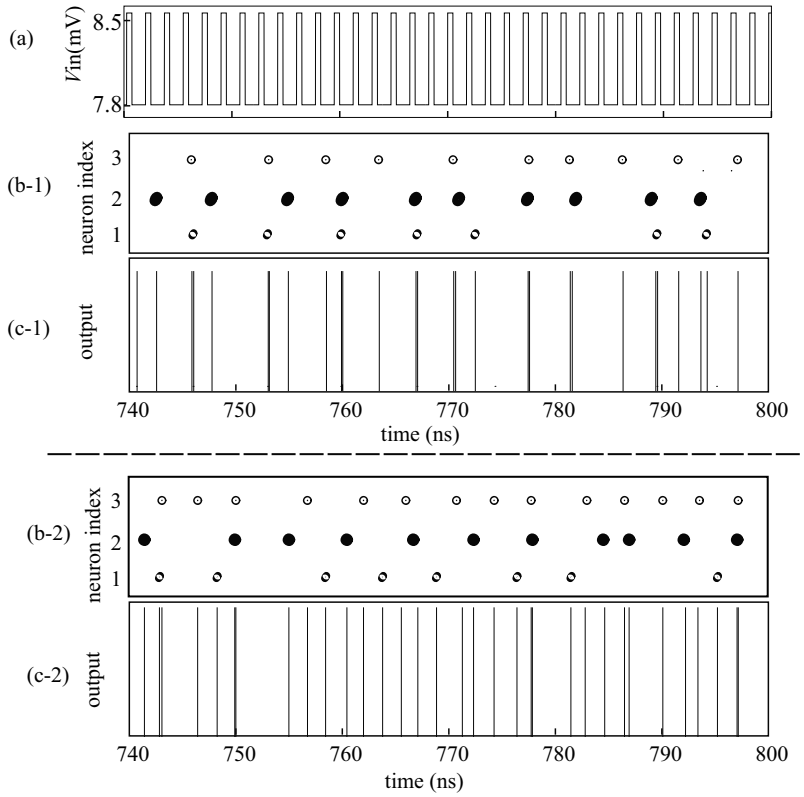

Figure 9.12: Transient responses of both homogeneous and heterogeneous networks. (a) shows the input signal. (b-1) shows the firing events of each neuron, while (c-1) shows the summed pulse output for the three neurons in the homogeneous network. (b-2) shows the firing events, and (c-2) shows the summed pulse output of the heterogeneous network.

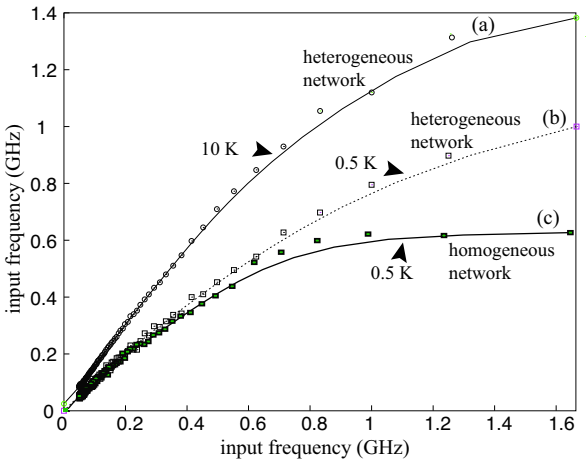

Figure 9.13: Output firing rate of an ensemble of neurons plotted against the input pulse frequency. (a) and (b) show response characteristics of a heterogeneous network simulated at a temperature of 10 K and 0.5 K, respectively. (c) shows response characteristics of a homogeneous network simulated at 0.5 K.

9.3.3 Effect of dynamic noises

Hospedales et al. ([15]) investigated the importance of random noises in improving the fidelity of signal transmission in the VOR. They concluded that besides neuronal heterogeneity, externally induced noises also play an important role in improving the network performance. These external noises could be as a result of spontaneous increases or decreases of membrane potential due to firing events in other neurons in the network. These changes are random and are often referred to as dynamic noises. In the proposed circuit, effect of dynamic noises was studied by considering thermally induced tunneling events in the network. Curves(a) and (b) in Fig. 9.13 show the response characteristics of a network simulated at 10K, and 0.5K, respectively. As the temperature increases, thermally induced tunneling events in single-electron neurons increase, resulting in an increase in the average firing rate in the network. This is illustrated by the increased firing rate at a temperature of 10 K. Although this work suggests that dynamic noises don't play a critical role in increasing the maximum response frequency of the network, they however, increase the fidelity with which the network can sample input signals within the maximum input signal frequency range determined by heterogeneity in the network elements. This is evident at higher input frequencies, where the ratio of the output pulse rate to the input pulse rate starts to roll-off rapidly. The roll off is compensated for by the dynamic noises, which reduces the effect of waiting time in electron tunneling. This is

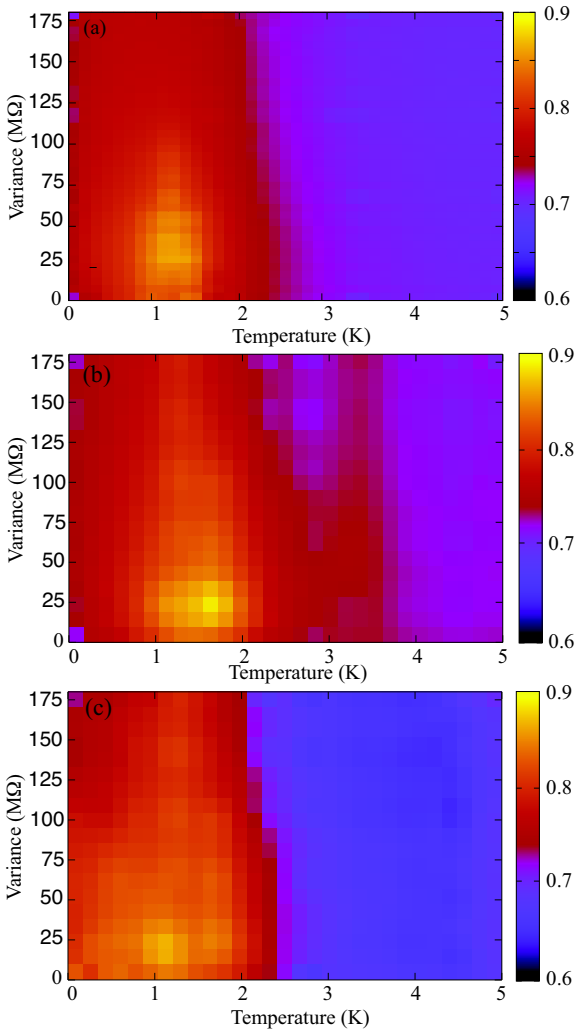

Figure 9.14: Effect of static (variance) and dynamic noises (temperature) to the correlation values in an ensemble of neurons fed with various input signal frequencies: 500 MHz for (a), 400 MHz for (b) and 200 MHz for (c).

further confirmed in section 9.3.4.

9.3.4 Effect of dynamic and static noises

To study the effect of both noises in the transmission fidelity of a heterogeneous network, we calculated the correlation between the input and the output signals in a network of 100 noisy neurons. The neurons were fed with a bias voltage of 8 mV, a sinusoidal input signal with a frequency (f) of 500, 400 and 200 MHz and peak-to-peak amplitude of 1 mV above the bias voltage. The simulation results are shown in Fig. 9.14 where f = 500 MHz for (a), f = 400 MHz for (b), and f = 200 MHz for (c). The horizontal axis shows the operation temperature (T), while the vertical axis shows the variance (σ) of the series resistances with a mean value of 100 M Ω. The scale of the color grading is shown on the right, with the light shading representing a correlation value of 0.9, and the dark shading representing a correlation of 0.6. From the results we observe that the network could produce the maximum correlation value ($\mathrm{C_{max}}$) of 0.87 at a variance of 30 M Ω and a temperature of 1.25 K, for the given set of circuit parameters and input signal frequency of 500 MHz, $\mathrm{C_{max}}$ of 0.89 at a variance of 25 M Ω and a temperature of 1.75 K at an input frequency of 400 MHz, and $\mathrm{C_{max}}$ of 0.88 at a variance of 20 M Ω and a temperature of 1.25 K at an input frequency of 200 MHz. This confirms that the effect of static noises is more dominant in enhancing the fidelity of transmission of high-frequency input signals.

9.4 Summary

To provide a basis for designing electronic circuits with mismatch-prone single-electron devices, this chapter proposed and investigated the performance of a bio-inspired 1-bit analog-to-digital converter. The circuit elements are coupled to each other through a global inhibitory coupling. Through Monte-Carlo based computer simulations, we demonstrated that the presence of static and dynamic noises, and the global inhibitory coupling introduced into the circuit play an important role in improving its noise-shaping properties. The signal to noise ratio improved by 4.34 dB in the coupled network as compared to the un-coupled one. In the second section of the chapter, we proposed and investigated the implication of heterogeneity in transmission of high frequency signals in a neural network. Through Monte-Carlo based computer simulations, we confirmed that heterogeneity in device parameters indeed improved the temporal precision with which the network could transmit signals with high input frequencies within the network. A heterogeneous network could correctly encode signals of upto 1 GHz,

as compared to 500 MHz in single neurons (or a network of homogenous neurons). Another important factor to consider in improving the fidelity of this circuit would be the effect of external and internal (dynamic) noises. In single-electronic devices, such noises include thermally induced random firing events or the effect of environmental noises. As we have shown, as the temperature increases, the dynamic noises also increase compensate for the roll-off in response of the network, especially at high frequencies. The preliminary results presented in this chapter show that in addition to heterogeneity in neuron properties, externally introduced noises could assist in further improving the fidelity of signal encoding in single-electron circuits. We should however, note that at higher temperatures, beyond the results presented here, random tunneling as a result of dynamic noises would increase rapidly leading to degradation of signal transmission. Therefore, the value of dynamic noises to be introduced to the network to achieve the best performance needs to be optimized.
Before summarizing the chapter, it's worth noting on similar promising works in achieving robust electronic systems by utilizing noises in improving signal-to-noise ratio in electronic systems. This approach has been demonstrated with single-electron devices, and nanowire transistor networks [13]. The architectures effectively employ stochastic resonance (SR) [3], and demonstrate a viable novel approach to realizing robust systems in noisy environments. Stochastic resonance is a phenomenon where weak signals can be retrieved from a noisy output [14] by applying an optimal amount of random noise. Oya et. *al*., [4] proposed a single-electron neural network that utilizes SR in signal transmission in neural networks, and successfully demonstrated that using SR indeed improved the temperature performance of the circuit. Kasai et. *al*. [13] experimentally investigated the performance of nanowire transistors with variations in threshold voltages and operating in a noisy experimental setup. In both cases, the effects of SR were investigated by setting the input signal to a value lower than the tunneling (firing) threshold of the network elements. By applying noises, network elements with non-zero inputs were induced to tunnel—tunneling events synchronized with the input signal to a certain quantity of noises. The authors showed that the SNR in their circuits was enhanced through partially using noises.
Such innovative approaches, in addition to the neuromorphic methodology described in this chapter would be indispensable in addressing reliability issues in electronic circuitry with nano-electronic devices. From the investigation results, we can conclude that by learning from biological systems: high levels of redundancy where information processing depends on many neurons operating in parallel, controlled signal transfer through excitatory and inhibitory synapses, and

stochastic resonance mechanisms, we could get hints on how to design circuits that perform better even in noisy environments and (or) with failure-prone electronic devices.

References

[1] C., Constantinescu, ”Trends and challenges in VLSI circuit reliability,” *IEEE Micro*, vol. 23, pp. 14 –19, 2003.

[2] A. Utagawa, T. Asai, T. Hirose, and Y. Amemiya, ”An inhibitory neural-network circuit exhibiting noise shaping with subthreshold MOS neuron circuits,” *IEICE Transactions on Fundamentals of Electronics, Communications and Computer*, E90-A, pp. 2108–2115, 2007.

[3] J.J. Collins, C.C. Chow, T.T. Imhoff, ”Stochastic resonance without tuning,” *Nature*, vol. 376, pp. 236–238, 2002.

[4] T. Oya, T. Asai, and Y. Amemiya, ”Stochastic resonance in an ensemble of single-electron neuromorphic devices and its application to competitive neural networks,” *Chaos, Solitons & Fractals*, vol. 32, pp. 855–861, 2007.

[5] T. Oya, T. Asai, R. Kagaya, T. Hirose, and Y. Amemiya, ”Neuronal synchrony detection on single-electron neural network,” *Chaos, Solitons & Fractals*, vol. 27, pp. 887–894, 2006.

[6] C. Mayr, and R. Schueffny, ”Applying Spiking Neural Nets to Noise Shaping,” *IEICE - Transactions on Information and Systems*, E88-D, pp. 1885–1892, 2005.

[7] D.J. Mar, C.C. Chow, W. Gerstner, R.W. Adams, and J.J. Collins, ”Noise shaping in populations of coupled model neurons,” *Neurobiology*, vol. 96, pp. 10450–10455, 1999.

[8] T. Oya, T. Asai, T. Fukui, and Y. Amemiya, ”Reaction-diffusion systems consisting of single-electron circuits,” *Inter. J. of Unconventional Computing*, vol. 1, pp. 177–194, 2005.

[9] T. Asai, Y. Kanazawa, and Y. Amemiya, ”A subthreshold MOS neuron circuit based on the volterra System,” *IEEE transactions on neural networks*, vol. 14, no. 5, pp. 1308–1312, 2003.

[10] M.A. Cohen, and S. Grossberg, ”Absolute stability of global pattern formation and parallel memory storage bycompetitive neural networks,” *IEEE Transactions on Systems, Man and Cybernetics*, vol. 13, pp. 815–826, 1983.

[11] T. Fukai, and S. Tanaka, ”A simple neural network exhibiting selective activation of neuronal ensembles: from winner-take-all to winners-share-all,” *Neural Computation* vol. 9, pp. 77–97, 1997.

[12] Y-G. Kim, and J-K, Kwon, ”Multi-bit Sigma-Delta Modulator for Low Distortion and High-Speed Operation,” *ETRI Journal*, vol. 29, pp. 835–837, 2007.

[13] S. Kasai and T. Asai, ”Stochastic resonance in Schottky wrap gate-controlled GaAs nanowire field effect transistors and their networks,” *Applied Physics Express*, vol. 1, 083001, 2008.

[14] L. Gammaitoni, P. Hanggi, P. Jung, and F. Marchesoni, ”Stochastic resonance,” *Reviews of Modern Physics*, vol. 70, pp.223-287, 1998.

[15] T.M. Hospedales, M.C.W. Rossum, B.P. Graham, M.B. Dutia, ”Implications of Noise and Neural Heterogeneity for Vestibulo-Ocular Reflex Fidelity”, *Neural Computation*. 20, pp. 756–778, 2008.

[16] R.B. Stein, Some Models of Neuronal Variability. Biophysical Journal. 7, pp. 37–68, 1967.

10 Summary

This thesis investigated the possibility of creating electronic circuits with single-electron devices. Single-electron devices are viewed as promising devices for use in the next generation of LSIs. This owes to their inherently low power dissipation, and minute devices sizes that provide high device integration capacities that can be utilized in creating high resolution sensors, and in parallel information systems.

In this work, we first analyzed non-linear characteristics of dynamical systems consisting of coupled single-electron devices. In the second part of the thesis, a two-dimensional photon position sensor was proposed. This sensor utilizes the high device density to obtain a high spatial resolution. It also employs non-linear characteristics of coupled single-electron devices to enable transmission of signals amongst individual device elements. This eliminates the need to fabricate signal wires within the device, resulting in a compact sensor system.

In the third part of the thesis, we focused on obtaining hints from how living organisms carry out signal processing to create noise-tolerant LSIs. We considered two well studied retinal models to create an edge detection circuit and a motion detection circuit. We further investigated the implication of noises (static noises from device fabrication mismatches and dynamic noises from thermally induced random tunneling events) in actual fabrication of the proposed circuit architectures. We proposed a novel method, where instead of getting rid of the noises, we effectively employ such noises in signal processing. We confirmed that employing such noises enhances the signal-to-noise ratio, and improves the fidelity with which the circuits can transmit high-frequency signals.

Through Monte-carlo based computer simulations, we confirmed that indeed single-electron device could be used to create highly efficient LSIs. Further more, we confirmed that by exploiting noises, we can improve signal-to-noise ratios and the fidelity of signal transmission.

List of Publications

1. Peer Reviewed Journal Papers

1. Kikombo A.K., Tabe M., and Amemiya Y., ”Photon position sensor consisting of single-electron circuits,” Nanotechnology, vol. 20, no. 40, 405209, 2009.

2. Kikombo A.K., Schmid A., Asai T., Leblebici Y., and Amemiya Y., ”A bio-inspired image processor for edge detection with single-erectron circuits,” Journal of Signal Processing, vol. 13, no. 2, pp 133-144, (2009)

3. Kikombo A.K., Asai T., Oya T., Schmid A., Leblebici Y., and Amemiya Y., ”A neuromorphic single-electron circuit for noise-shaping pulse-density modulation,” International Journal of Nanotechnology and Molecular Computation, vol. 1, no. 2, pp. 80-92 (2009).

4. Kikombo A.K., Asai T., and Amemiya Y., ”An elementary neuro-morphic circuit for visual motion detection with single-electron devices based on correlation neural networks,” Journal of Computational and Theoretical Nanoscience, vol. 6, no. 1, pp. 89-95 (2009).

5. Kikombo A.K., Hirose T., Asai T., and Amemiya Y., ”Non-linear phenomena in electronic systems consisting of coupled single-electron oscillators,” Chaos, Solitons and Fractals, vol. 37, no. 1, pp. 100-107 (2008).

6. Kikombo A.K., Oya T., Asai T., and Amemiya Y., ”Discrete dynamical systems consisting of single-electron circuits,” International Journal of Bifurcation and Chaos, vol. 17, no. 10, pp. 3613-3617 (2007).

2. Book chapters

1. Kikombo A.K., Asai T., and Amemiya Y., Pulse-Density Modulation with an ensemble of single-electron circuits employing neuronal heterogeneity to achieve high temporal resolution, ” Nano-Net 2009, A. Schmid, S. Goel, W. Wang, V. Beiu and S. Carrara., Eds., Lecture Notes of the Institute for Computer Sciences, pp. 51-56 , Springer German (2009)

2. Kikombo A.K., Asai T., and Amemiya Y., ”Exploiting temporal noises and device fluctuations in enhancing fidelity of pulse-density modulator consisting of single-electron neural circuits,” Neural Information Processing, Leung C.S., Lee M., and Chan J.H., Eds., Lecture Notes in

Computer Science, vol. 5864, pp.384-391, Springer Berlin / Heidelberg (2009).

3. Invited Talks

1. Kikombo A.K., Asai T. and Amemiya Y., "Neuro-morphic circuit architectures employing temporal noises and device fluctuations to enhance signal-to-noise ratio in pulse-density modulation," The 4th International Workshop on Natural Computing, Himeji, Japan (Sep. 23-25, 2009).

2. Kikombo A.K., "Circuit architectures for Beyond CMOS electronic devices: Learning from biological systems toward creating robust electronic systems with fault-prone building blocks," Faculty Seminar in National Institute of Standards and Technology, Quantum Processes and Metrology Group, Maryland, USA (Jun. 22, 2009).

4. Papers presented at International Conferences and Workshops

1. Kikombo A.K., Asai T., and Amemiya Y., "Single-electron pulse-density modulation circuits employing device fabrication mismatches and temporal noises to achieve high signal to noise ratio," Proceedings of the 3rd International Symposium on Global COE Program of Center for Next-Generation Information Technology Based on Knowledge Discovery and Knowledge Federation, pp. 254-256, Sapporo, Japan (Jan. 18-20, 2010).

2. Kikombo A.K., Asai T., and Amemiya Y., "Morphic circuit architectures for beyond CMOS LSIs using failure-prone nano-electronic devices," Proceedings of the 3rd International Symposium on Global COE Program of Center for Next-Generation Information Technology Based on Knowledge Discovery and Knowledge Federation, Sapporo, Japan (Jan. 18-20, 2010).

3. Kikombo A.K., Asai T., and Amemiya Y., "Bio-inspired single-electron circuit architectures exploiting thermal noises and device fluctuations to enhance signal transmission fidelity," Proceedings of the 2009 International Symposium on Intelligent Signal Processing and Communication Systems, Kanazawa, Japan (Dec. 7-9, 2009).

4. Kikombo A.K., Asai T, Amemiya Y., ”Exploiting temporal noises and device fluctuations in enhancing fidelity of pulse-density modulator consisting of single-electron neural circuits,” Proceedings of the 16th International Conference on Neural Information Processing, pp. 384-391, Bangkok, Thailand (Dec. 1-5, 2009).

5. Kikombo A.K., Asai T, Amemiya Y., ”Pulse-density modulation with an ensemble of single-electron circuits employing neuronal heterogeneity to achieve high temporal resolution,” Proceedings of the 4th International Conference on Nano-Networks, pp. 51-56, Luzern, Switzerland (Oct. 18-20, 2009).

6. Kikombo A.K., Asai T, Amemiya Y., ”Noise-driven architectures toward beyond CMOS LSIs with failure-prone nano-electronic devices,” Proceedings of the 14th International Commercialization of Micro and Nano Systems Conference, P-18, Copenhagen, Denmark (Aug. 30-Sep. 4, 2009).

7. Kikombo A.K., Asai T., Oya T., Schmid A., Leblebici Y., and Amemiya Y., ”A pulse-density modulation circuit exhibiting noise shaping with single-electron neurons,” Proceedings of the 2009 International Joint Conference on Neural Networks, pp. 1600-1605, Atlanta, USA (Jun. 14-19, 2009).

8. Kikombo A.K., Asai T., and Amemiya Y., ”Fault-tolerant architectures for single-electronic circuits based on neural networks,” Proceedings of the 2nd International Symposium on Global COE Program of Center for Next-Generation Information Technology Based on Knowledge Discovery and Knowledge Federation, pp. 275-276, Sapporo, Japan (Jan. 20-21, 2009).

9. Kikombo A.K., Schmid A., Asai T., Leblebici Y., and Amemiya Y., ”Fault-tolerant architectures for nanoelectronic circuits employing simple feed-forward neural networks without learning,” Proceedings of the 15th International Conference on Neural Information Processing of the Asia-Pacific Neural Network Assembly, p. 328, Auckland, New Zealand (Nov. 25-28, 2008).

10. Kikombo A.K., Asai T., and Amemiya Y., ”An insect vision-based single-electron circuit performing motion detection,” Proceedings of the 2008 Asia-Pacific Workshop on Fundamentals and Applications of Advanced Semiconductor Devices, pp. 159-164, Sapporo, Japan (Jul. 9-11, 2008).

11. Kikombo A.K., Asai T., and Amemiya Y., ”A neuromorphic circuit for motion detection with single-electron devices based on correlation neural networks,” The 2008 IEEE Silicon Nanoelectronics Workshop, pp. P1-31, Honolulu, USA (Jun. 15-16, 2008).

12. Kikombo A.K., Asai T., and Amemiya Y., ”Morphic approaches toward establishing emerging image processing architectures for Beyond CMOS nano-electronic devices,” The 4th International Nanotechnology Conference on Communications and Cooperation, Japan Session Poster Poster No. 1, Tokyo, Japan (Apr. 14-17, 2008).

13. Kikombo A.K., Schmid A., Asai T., Leblebici Y., and Amemiya Y., ”Implementation of early vision model for edge extraction with single-slsecton devices,” Proceedings of the 12th International Conference on Cognitive and Neural Systems, p. 125, Boston, USA (May 14-17, 2008).

14. Kikombo A.K., Schmid A., Asai T., Leblebici Y., and Amemiya Y., ”Toward a single-electron image processor for edge detection based on the inner retina model,” Proceedings of the 2008 RISP International Workshop on Nonlinear Circuits and Signal Processing, pp. 267-270, Gold Coast, Australia (Mar. 6-8, 2008).

15. Kikombo A.K., Asai T., Hirose T., and Amemiya Y., ”Neuromorphic nano-electronic circuits performing edge enhancement with single-electron devices,” Proceedings of the 2008 International Symposium on Global COE Program of Center for Next-Generation Information Technology based on Knowledge Discovery and Knowledge Federation, pp. 137-138, Sapporo, Japan (Jan. 22-23, 2008).

16. Kikombo A.K., Schmid A., Leblebici Y., Asai T., and Amemiya Y., ”A bio-inspired image processor for edge detection with single-electron circuits,” 2007 International Semiconductor Device Research Symposium, TA3-04, Maryland, USA (Dec. 12-14, 2007).

17. Kikombo A.K., Tabe M., and Amemiya Y., ”Photon position detector consisting of single-electron devices,” Extended Abstract of the 2007 International Conference on Solid State Devices and Materials, pp. 1114-1115, Ibaraki, Japan (Sep. 18-21, 2007).

18. Kikombo A.K., Hirose T., Asai T., and Amemiya Y., ”Multi-valued logic circuits consisting of single-electron devices,” Proceedings of the 2007 Silicon Nanoelectronics Workshop, pp. 81-82, Kyoto, Japan (Jun. 10-11, 2007).

19. Kikombo A.K., Hirose T., Asai T., Amemiya Y., ”Non-linear dynamics of coupled single-electron oscillator systems,” Collected Papers of the 4th International Symposium on Ubiquitous Knowledge Network Environment, p. 72, Sapporo, Japan (Mar. 5-7, 2007).

20. Kikombo A.K., Hirose T., Asai T., Amemiya Y., ”Non-linear dynamical systems consisting of single-electron oscillators,” Proceedings of the 14th International Workshop on Nonlinear Dynamics of Electronic Systems, pp. 81-84, Dijon, France (Jun. 6-9, 2006).

21. Kikombo A.K., Asai T., and Amemiya Y., ”Single-electron discrete dynamical systems,” The 3rd International Symposium on Ubiquitous Knowledge Network Environment, p. 47, Sapporo, Japan (Feb. 28-Mar. 1, 2006).

22. Kikombo A.K., Oya T., Asai T., and Amemiya Y., ”Discrete dynamical systems consisting of single-electron circuits,” Proceedings of the 13th International IEEE Workshop on Nonlinear Dynamics of Electronic Systems, S-13, Potsdam, Germany (Sep. 18-22, 2005).

5. Papers presented at Domestic Conferences

1. Kikombo Andrew Kilinga, 浅井 哲也, 雨宮 好仁, ”A design methodology for multi-valued logiccircuits with single-electron tunneling devices,” 北海道大学情報科学研究科 若手研究者支援のための産学協同 GCOE シンポジウム, P2-05, (札幌), 2008 年 10 月.

2. Kikombo Andrew Kilinga, Schmid Alexandre*, 浅井 哲也, Leblebici Yusuf*, 雨宮 好仁, ”Toward a bio-inspired image processor for edge extraction with single-electron devices,” 電子情報通信学会 ニューロコンピューティング研究会, (佐賀), 2007 年 11 月. [*Swiss Federal Institute of Technology (EPFL)]

3. Kikombo Andrew Kilinga, 雨宮 好仁, 田部 道晴, ”単電子振動子ネットワークによるフォトン位置検出センサ,” 応用物理学会秋季大会, (札幌), 2007 年 9 月.

4. Kikombo Andrew Kilinga, 廣瀬 哲也, 浅井 哲也, 雨宮 好仁, ”単電子の位相ロッキングを利用した多値論理回路,” 応用物理学会春季大会, (神奈川), 2007 年 3 月.

5. Kikombo Andrew Kilinga, 廣瀬 哲也, 浅井 哲也, 雨宮 好仁, ”単電子結合振動子の非線形現象,” 応用物理学会秋季大会, (滋賀), 2006 年 8 月.

6. Kikombo Andrew Kilinga, 大矢 剛嗣, 浅井 哲也, 雨宮 好仁, ”単電子結合振動子による離散力学システムのダイナミクス,” 応用物理学会春季大会, (東京), 2006 年 3 月.